Computational Studies of Chemical Systems: I. A Molecular Dynamics Simulation of Methane Hydrate; II. Theoretical Investigation of Water Loading on a Pyrophyllite (001) Surface

by

Guozhen Zhang

BS, Wuhan University, China, 2004

MS, Fudan University, China, 2007

Submitted to the Graduate Faculty of

The Dietrich School of Arts and Sciences in partial fulfillment

of the requirements for the degree of

Doctor of Philosophy

University of Pittsburgh

2012

UNIVERSITY OF PITTSBURGH

THE DIETRICH SCHOOL OF ARTS AND SCIENCES

This dissertation was presented

by

Guozhen Zhang

It was defended on

June 15th, 2012

and approved by

Lilian Chong, Associate Professor, Department of Chemistry

Kenneth Jordan, Distinguished Professor, Department of Chemistry

Haitao Liu, Assistant Professor, Department of Chemistry

Alan McGaughey, Professor, Department of Mechanical Engineering, Carnegie Mellon University

Advisor: Kenneth Jordan, Distinguished Professor, Department of Chemistry

Computational Studies of Chemical Systems: I. A Molecular Dynamics Simulation of Methane Hydrate; II. Theoretical Investigation of Water Loading on a Pyrophyllite (001) Surface

Guozhen Zhang, PhD

University of Pittsburgh, 2012

This dissertation consists of two independent parts: Part I. methane hydrate, and Part II. water loading on a clay surface. In Part I (chapter 2-3), we conducted molecular dynamics simulations with non-polarizable force fields to study structural and thermal properties of methane hydrate. We show that the TIP4P/Ice and TIP4P/2005 model potentials do well in the description of the lattice constant and radial distribution functions. Yet they, together with SPC/E and TIP4P models, overestimate the thermal expansion coefficient due to the inadequate description of the non-linear response of lattice constant to temperature. We also show that TIP4P/Ice and TIP4P/2005 overestimate the decomposition temperature of methane hydrate from the experimental value by 50 K and 30 K respectively, while SPC/E gives a good estimation deviating by about 5 K. All these force fields are found to overestimate the thermal conductivity of methane hydrate, but they are able to describe the weak temperature dependence from 100 to 150 K and 225 to 270 K. It is also found that all initial structures used in the work have a proton ordering tendency, suggesting a potential role of proton arrangement in the temperature dependence of the thermal conductivity. In part II (chapter 4), we conducted dispersion-corrected density function theory (DFT-D) and classical force field calculations to study the water loading on a pyrophyllite (001) surface. We disclose low-energy binding motifs from one water molecule to six water molecules and reinterpret the hydrophobic nature of the pyrophyllite surface from the point of view that a water molecule prefers to interact with other water molecules than to be

bound on the surface. The force field approach, while providing a similar trend of the water binding to the DFT-D result, predicts some low-energy binding motifs which are not confirmed by the DFT-D calculation. It suggests a refinement of the force field to better describe the interfacial orientation of water on a clay surface.

TABLE OF CONTENTS

LIST OF TABLES

LIST OF FIGURES

PREFACE

I would like to thank my research adviser, Professor Kenneth Jordan.

Professor Jordan teaches me how to do research with his great kindness and patience. He always encourages me to ask questions, challenges me on my superficial understandings, helps me to explore subtle scientific problems, and trains me to polish my thoughts on specific research subjects. Moreover, he sets an example for me to be a scientist. His passion, serenity, and insight on science touch me deep in heart. It reminds me of the great Albert Einstein's famous quote that "all our science, measured against reality, is primitive and childlike – and yet it is the most precious thing we have". Having working with him, I could perceive how the spirit of academic research is inherited from generation to generation. I always enjoy the discussions with him and his scientific style humor. I owe him too much. The experience of being his student will become a precious memory in the rest of my life.

I want to thank Dr. Hao Jiang. He was a former member in Jordan group. He is always kind, patient and knowledgeable in our discussions on the methane hydrate project. Our current progress on the methane hydrate study cannot be made without his precedent work and help.

I want to Dr. Wissam Al-Saidi for the fruitful discussions on clay project and Dr. Evgeniy Myshakin for his kindly help and comments on methane hydrate project as well as clay project. It is my pleasure to collaborate with them.

I want to thank Dr. Richard Christie for his invaluable help in the use of the computing resources in the Center for Simulation and Modeling (SAM, formerly CMMS).

I would like to thank all my committees, Professor Kenneth Jordan, Professor Lilian Chong, Professor Haitao Liu, and Professor Alan McGaughey, for their invaluable comments and help in the preparation of this dissertation.

I would like also thank all other Jordan group members, especially Dr. Glen Jenness, Dr. Revati Kumer, Dr. Fangyong Yan, Vamsee Voora, Eric Kratz, Xiaoge Su, Xun Wang, Ozan Karalti, and Michael Deible, for their invaluable help in my research work and thesis writing and revision.

I want to thank CMU ballroom dance club for providing me the opportunity to learn ballroom dance and attend dancesports competitions. Because it lets me intuitively understand that nothing meaningful goes easy, which I think encourages me to pursue the PhD work.

At last, I would like to thank the steadfast love from my father and mother, which is a constant strength that help me face the challenge and difficulty in life. Without their constant support, I cannot imagine my standing in US to do the research. This thesis is dedicated to you, mom and dad.

1.0 INTRODUCTION TO METHANE HYDRATE AND CLAY

Natural gas, of which the primary constituent is methane, is an important energy and chemical feedstock. In nature, enormous quantities of natural gas are stored in the form of clathrate hydrates in suboceanic sediments and in permafrost, which is out of the reach of human activities.[1] The increasing concern of the shrinking of readily accessible reserves of natural gas, however, has spurred the interest in exploring clathrate hydrates of natural gas (aka methane hydrate) as a potential source of methane. In addition, methane is an important greenhouse gas, which has been regarded to be responsible for the historical climate change occurring 15,000 years ago.[1] As a matter of fact, it is over 20 times more effective in trapping heat in the atmosphere than carbon dioxide.[1] Therefore, research on methane hydrates is motivated by applications as energy recovery, as well as understanding the role in climate change.[2] The study of methane hydrate is very broad and diversified, ranging from the molecular structure, to mechanical and thermal properties, from phase equilibria, to formation, decomposition and growth.[1]

While much of the research on methane hydrate is concerned with its formation and growth, it is the understanding of its structure that is the foundation of the understanding of all other properties. Thus, we choose the study of its structure as the starting point. We are also concerned with some peculiar properties that are associated with the structure. For example, methane hydrate behaves very differently from ice Ih in thermal conductivity, albeit that they

share many similarities in their compositions and structures. Thermal conductivity (κ) describes a matter's capability to conduct heat. It is measured in watt per meter kelvin ($W \cdot m^{-1} \cdot K^{-1}$).[3] Although both ice Ih and methane hydrate are crystalline materials, ice exhibits a typical crystal-like T-dependence, while methane hydrate exhibits an unusual amorphous-like T-dependence. Moreover, the κ of methane hydrate is an order of magnitude lower than that of ice Ih.[1] This peculiar phenomenon has been a subject of intense research since early 1980s,[4] not only because of the curiosity of the relationship between the thermal conduction and the microscopic structure, but also because of the potential application in the exploration of methane hydrate in sediments.[1] What's more, the clathrate framework is very useful in the design of functionalized materials. For example, inorganic clathrates have been proposed to be promising candidates of thermoelectric materials.[5]

The influence of clay minerals on the formation of methane hydrate has drawn our attention on clay minerals. Recently, it has been found in experiments that methane hydrate can form at the interlayer of montmorillonites (MMTs), an important type of clay minerals.[6-9] Since MMTs are important components of sediments, these discoveries could help us understand the formation of methane hydrate in the natural environment. Apparently, it is necessary to understand the related property of MMTs, which can undergo expansion in the presence of water.[10]

As a matter of fact, expansive clay minerals have many important tributes, such as swelling, sorption, and ion-exchange properties, which make them not only important in the geochemical cycles of metal cations and the oceanic buffering of atmospheric CO_2, but also useful in a wide range of industrial applications, including catalysis, nuclear waste disposal, petroleum extraction and agrochemical delivery.[11-17] Besides, MMTs have also been proposed

for use in CO_2 sequestration.[18] Since all these important phenomena are related to the interactions between water and clay minerals, we will initiate the study of clay minerals from the water-clay interactions.

Computational chemistry, on the basis of physics laws, has become a more and more powerful tool to study chemical systems. In this thesis, I will present our computational study on methane hydrate and clay minerals in three chapters: chapter 2 is about the study of the structure and thermal properties (such as lattice constants, thermal expansion coefficient, radial distribution function, power spectra and decomposition temperature, etc.) of methane hydrate; chapter 3 is about the study of thermal conductivity of methane hydrate; and chapter 4 is about the study of water loading on a pyrophyllite (001) surface.

2.0 STRUCTURE AND DECOMPOSITION OF METHANE HYDRATE

2.1 INTRODUCTION

In this chapter, classical molecular dynamics simulations have been carried out to calculate the decomposition temperature of methane hydrate as well as some of the structural properties of it, including the lattice constant, thermal expansion coefficient, radial distribution functions, and power spectra. These work employed non-polarizable water models, including the SPC/E, TIP4P, and TIP4P-derived models (TIP4P/2005 and TIP4P/Ice). It is found that TIP4P/2005 and TIP4P/Ice give a better description of lattice constant from T = 50 K to 200 K compared to polarizable water models (COS/G2 and AMOEBA). However, all model potentials overestimate the thermal expansion coefficient from T = 100 K to 200 K. Suggestions on the improvement of force fields are given on the basis of the analysis of the fitting function of a lattice constant. Radial distribution functions predicted by TIP4P/2005 and TIP4P/Ice models are also in excellent agreement with the results from polarizable models, yet the power spectra given by these two models are substantially different from those from polarizable models in certain regions. The calculations of the decomposition temperature of methane hydrate show that TIP4P/2005 and TIP4P/Ice force fields overestimate the value by 30 K and 50 K, respectively. By contrast, SPC/E force field gives estimation in line with the experimental value.

2.1.1 Methane Hydrate

The first question of understanding clathrate hydrates lies in their structures. They are ice-like inclusion compounds in which small atoms or molecules (such as Xe, CH_4 and CO_2) are trapped in hydrogen-bonded water cavities.[2] The weak interactions (especially the repulsion) between the encaged atoms/molecules (guest) and the water lattice (host) stabilize the hydrate, which is crucial for the formation of clathrate hydrates.[1] There are three most common types of crystal structures for gas hydrates found in nature, cubic structure I (sI), cubic structure II (sII) and hexagonal structure H (sH).[2] Their geometrical parameters are summarized in Table 2.1. As seen from Table 2.1, the 5^{12} (pentagonal dodecahedral) water cage is the only cage common to all the three hydrate structures.

Table 2.1 Crystal Structures and Cage Geometries for Structure I, II, and H Hydrates. [a]

Property	**Structure I**		**Structure II**		**Structure H**		
Crystal System	Cubic		Cubic		Hexagonal		
Approx. Lattice Constants[Å]	a = 12		a = 17		a = 12, c = 10		
No. of H_2O per Unit Cell	46		136		34		
Cavity type	small	large	small	large	small	medium	large
Geometry	5^{12}	$5^{12}6^2$	5^{12}	$5^{12}6^4$	5^{12}	$4^3 5^6 6^3$	$5^{12}6^8$
No. of Cavities	2	6	16	8	3	2	1
Avg. Cage Radius[Å]	3.95	4.33	3.91	4.73	3.91	4.06	5.71

[a] The data are adapted from Ref. 1.

This is not by accident. The HOH angle of a water molecule in its equilibrium geometry in gas phase is known to be 104.52 º. When water molecules exist in its solid phases (e.g. hexagonal ice, termed as "ice Ih"), they follow the Bernal-Fowler rule to form the most stable structures, as proposed by Bernal and Fowler in 1933.[19] This rule states that: 1). Oxygen atoms form a lattice with tetrahedral coordination; 2) there is exactly one proton between two neighboring oxygen atoms, which is covalently bonded to one oxygen and forms a hydrogen

bond to the other.[20] It is well-known that the O-O-O angle in a standard tetrahedral coordination is 109.47°. When 20 water molecules assemble a 5^{12} cage, the O-O-O angle in each planar pentagonal face is 108°. It results in a 1.5 °deviation from the O-O-O angles of ice Ih, and a 3.5 ° deviation from the HOH angle of free water molecule. This is the lowest price that can be paid in nature to form a water cavity. By contrast, the hexamer face in the $5^{12}6^2$ cage and the tetramer face in the $4^3 5^6 6^3$ cage respectively bear an O-O-O angle of 120 °and 90 °, resulting in a much larger strain of water cavities. Therefore, the 5^{12} cage becomes the most common building block of clathrate hydrate structures.[1]

Methane hydrate normally occurs as a sI hydrate. The tendency that a guest forms a certain type of structure rather than others is influenced by the size ratio of guest diameter to cavity diameter. Generally, 0.76 is regarded as the lower bound of this ratio for a guest being able to stabilize the cavity. For a methane molecule, there is little difference for the occupation of 5^{12} cages (the ratio is 0.86-0.87), but it is entirely different in the case of large cages. It is 0.744 for $5^{12}6^2$ cavity of sI, yet only 0.655 for $5^{12}6^4$ cavity of sII.[1] Thus, it is advantageous for methane to form sI hydrate. In a sI hydrate, the 5^{12} cages are arranged in a body centered cubic lattice.[1] They are connected via vertices. The larger, oblate spaces between them form the $5^{12}6^2$ (tetrakaidecahedral) cages. The large cages are arranged in columns in three dimensions, with their opposing hexagonal faces shared between two contacted ones.[1]

Ideal (fully-occupied) methane hydrate has an empirical formula of $[CH_4 \cdot (5.75H_2O)]$, indicating 85 mol.% of water. This is the lower bound of water contents in methane hydrate.[1] In naturally occurred methane hydrate, the mole fraction of water is always larger than 85% because of incomplete guest occupation of host cavities. This is associated with the

nonstoichiometric nature of methane hydrate, which is related to guest size, temperature and pressure.[1]

Because such high water contents are organized in a form of periodic crystal structure, it is natural to compare it with ordinary solid water, i.e. ice Ih. It has been observed by experiments that hydrates bear a hydrogen bond network very similar to that of ice, in the respects of both hydrogen bond length and O-O-O angles.[1] One consequence of the similarity between compositions and structures of methane hydrate and ice Ih is that many of the hydrate mechanic properties resemble those of ice Ih, such as Bulk modulus, Shear modulus and compressional/shear velocity ratio.[1] However, there are also exceptions. For example, methane hydrate is found to be 20 times stronger (creep resistant) than ice.[1]

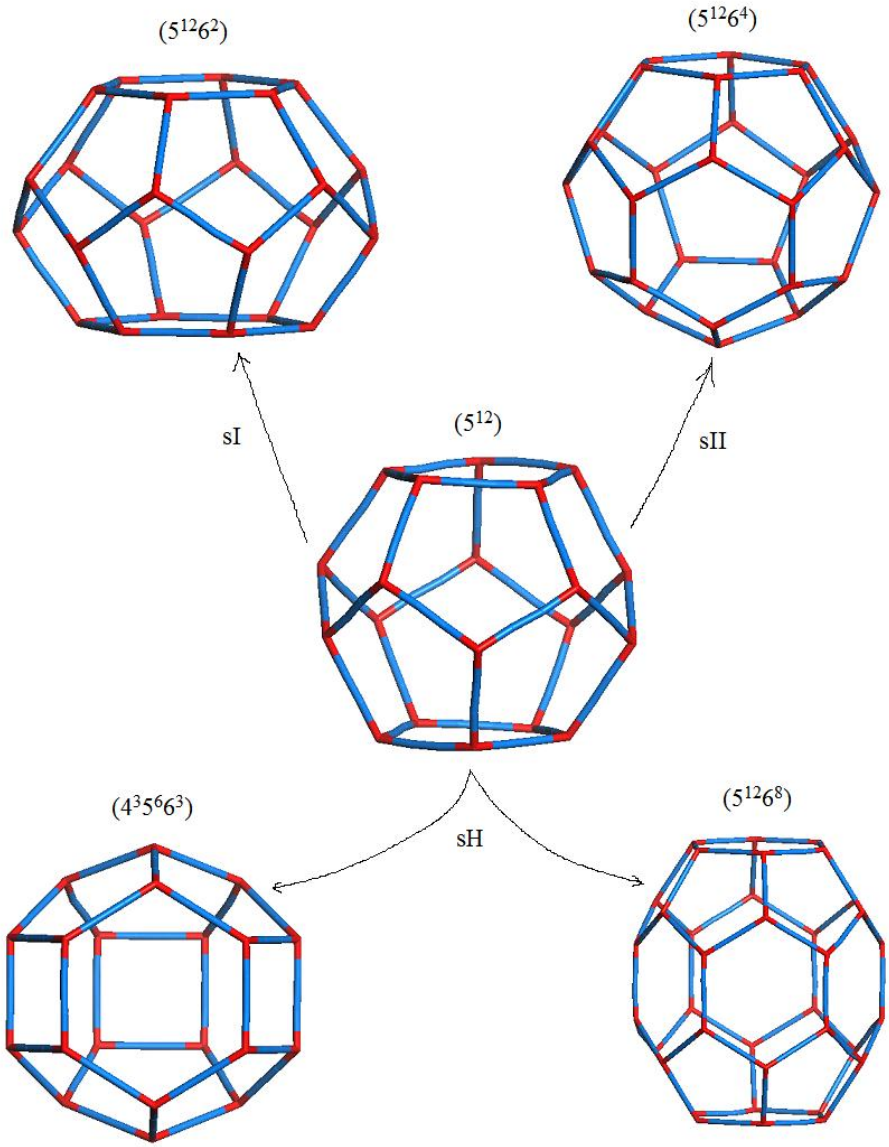

Figure 2.1: Structure representations of all type of water cages described in Table 2.1.

Meanwhile, there exist many differences between their microscopic structures. It is well-documented that sII hydrate and ice Ih have different profiles of hydrogen bond order parameters.[21,22] They are a set of quantities determined by the weight of all possible hydrogen bond arrangements associated with a water dimer in the context of water network. They can be

used for describing the distribution of protons and distinguishing between various lattice types. For ice Ih, there are four possible forms water dimers, labeled as inverse mirror (IM), oblique mirror (OM), inverse center (IC) and oblique center (OC).(Figs 2.2, 2.3) Their respective numbers, X_{im}, X_{om}, X_{ic} and X_{oc}, are termed as hydrogen bond order parameters. For sII hydrate, there are only mirror symmetric water dimers, described by X_{im} and X_{om}. sI hydrates are supposed to have only IM and OM water dimers, just as sII hydrates. (Figs 2.2, 2.3) These four different types of water dimers are not energetically equivalent. Taking the space repulsion of hydrogen atoms into account, IM and OC are slightly (< 1 kJ/mol) more stable than OM and IC, respectively. However, the ratios of each pair (IM~OM, OC~IC) are in a delicate equilibrium affected not only by the relative energies but also by the neighboring water molecules.[22] In an ideal (fully random) lattice of ice Ih, both X_{im}/X_{om} and X_{ic}/X_{oc} are 1/2, and $(X_{im}+X_{om})/(X_{ic}+X_{oc})$ is 1/3. The same ratio (1/2) applies to the X_{im}/X_{om} of an ideal lattice of sII hydrate.[22] The X_{im}/X_{om} and X_{ic}/X_{oc} ratios may deviate from 1/2 in real hydrate and ice samples; however, the total number of hydrogen bonds, which is 4, is invariant. Other pronounced structure and dynamics differences include but are not limited to unit cell sizes, the number of water molecules in a unit cell, dielectric constants, water reorientation and diffusion rates, as shown in Table 2.2.

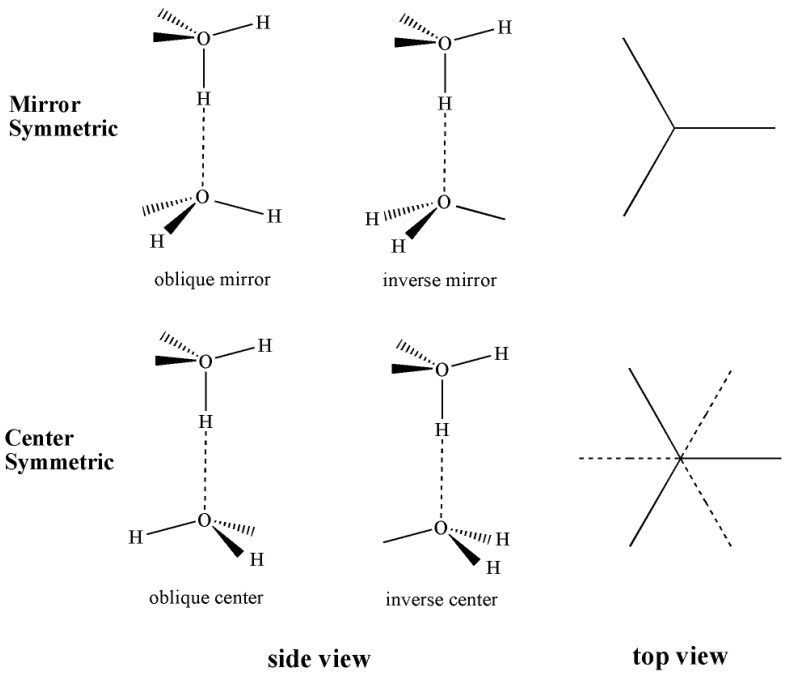

Figure 2.2: The side view and top view of all possible hydrogen-bonded water dimer arrangements in ice Ih and sI(II) hydrates.

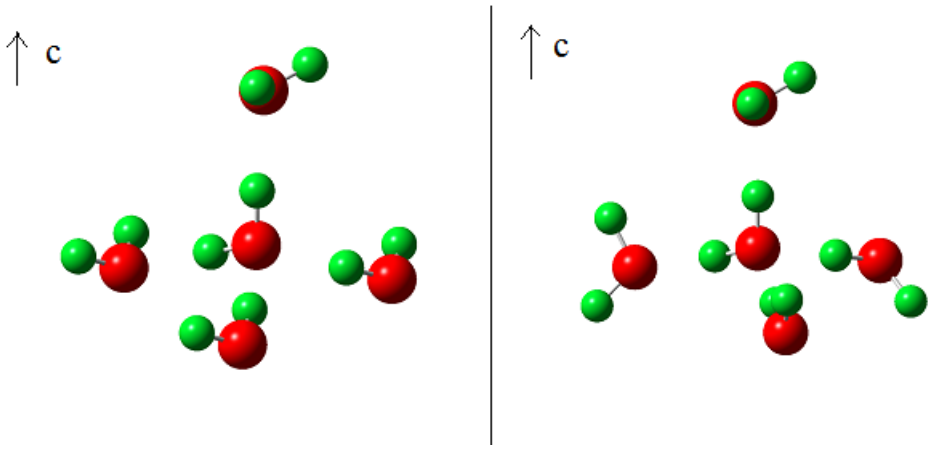

Figure 2.3: The representation of tetrahedral water network of ice Ih (left panel) and sI hydrate (right panel). For the center water molecule in ice Ih, the water dimer in the c direction is mirror symmetric, all other three dimers are center symmetric. For that in sI hydrate, all four water dimers are mirror symmetric.

Table 2.2 Comparison of Properties of Ice Ih and sI Hydrate.[a]

Property	Ice Ih	sI Hydrate
Unit cell size [a] (Å)	a = 4.52, c = 7.36	12.0
No. of H_2O in a unit cell	4	46
Dielectric constant [b]	94	~58
H_2O reorientation time [b] (μs)	21	~10
H_2O diffusion jump time (μs)	2.7	>200

[a] Data are retrieved from Ref. 1. [b] Values are measured at 273 K.

It can be seen that sI hydrate bears a much larger unit cell with an order of magnitude more water molecules relative to ice Ih. Yet their densities (ice: 0.91 g/cm^3, sI hydrate: 0.94 g/cm^3) are comparable at 273 K.[1] The dielectric constant of sI hydrate is about 60% of that of ice Ih. This is similar to the case of sII hydrate *vs* ice Ih.[1] The difference of dielectric constants between sII hydrate and ice Ih has been proposed to result from the difference of the water number molar volumes.[22] Another non-trivial factor that may affect the dielectric constant is the water reorientation time. It is well-documented that the reorientation of water in the lattice of ice is rooted from the disordered nature of protons due to the $(3/2)^N$ ways of arranging N water molecules under the Bernal-Fowler rules.[22] It can be promoted by the structure defects of ice crystals such as the Bjerrum defects.[1] Although the structure defects in hydrates are ill-defined in literatures, because of the similarity of hydrogen bonded networks between hydrates and ice, it is speculated that proton disorder and structure defects contribute to the dielectric constant in a comparable way.[1] As Table 2.2 shows, the water molecules reorient 50% slower in ice Ih than in sI hydrate. There might be some unknown relationship between water reorientation time ratio and dielectric constant ratio. Finally, water molecules diffuse two orders of magnitude slower in sI hydrate than in ice Ih, which may account for the higher mechanical strength of methane hydrate than ice.[1]

In addition, methane hydrate behaves very differently from ice Ih in thermal expansion. The coefficient of thermal expansion determines the rate of volume change of matter in response to temperature change.[23] Within various representations of the entity, the coefficient of linear thermal expansion (CTE) is often used for describing the property. It is defined as the fractional increase in length per unit rise in temperature and can be expressed as:[24]

$$(l_1 - l_0) / l_0 = \alpha_l (T_1 - T_0) \tag{2-1}$$

where l_0 and l_1 represent, respectively, the initial and final lengths due to the temperature change from T_0 to T_1. The parameter α_l is the CTE and has a unit of reciprocal temperature (K^{-1}). It has been found in experiment that the CTE of sI and sII is substantially larger than that of ice Ih below 200 K, as indicated in Table 2.3.

It has been suggested by computer simulations that large thermal hydrate thermal expansivity is due to anharmonic behavior in the water lattice which is the result of guest-host interactions.[1]

Table 2.3 Comparison of the CTE of Methane Hydrate and Ice Ih.[a]

Species	CTE (K^{-1})		
	T=100K	T=150K	T=200K
Ethylene oxide hydrate (sI)	40×10^{-6}	58×10^{-6}	77×10^{-6}
THF hydrate (sII)	28×10^{-6}	42×10^{-6}	52×10^{-6}
Ice Ih	$7\times10^{-6}/8\times10^{-6}$ [b]	$28\times10^{-6}/25\times10^{-6}$	$56\times10^{-6}/57\times10^{-6}$

[a]Adapted from Ref. 1. [b] The first number is for the CTE in *a* axis, the second number is in *c* axis.

Computer Simulations (divided into two categories: molecular dynamics, MD, and Monte Carlo, MC) are a set of important tools to bridge the macroscopic properties and microscopic properties of materials on the basis of statistical mechanics.[1,25,26] In the research area of methane hydrate, they have been widely used for studying its formation and growth and various structural, mechanical and thermal properties.[1]

2.1.2 Classical Molecular Dynamics

MD simulation is a powerful tool to study physical motions of atoms and molecules by probing the phase space of microscopic systems. The resulting trajectories can be used to determine macroscopic thermodynamic properties of systems on the basis of the ergodic hypothesis, to describe important physical and chemical processes such as phase transition and protein folding, to calculate various structure (e.g. radial distribution functions and power spectra) and transport (e.g. viscosity and thermal conductivity) properties.[25]

Both MD and MC simulations can be used for obtaining the macroscopic thermodynamic information based on the statistical mechanics of equilibrium states. However, MD can provide additional dynamics information that is unavailable from MC. This is the most distinctive advantages of MD over MC. Because the properties studied in our work are associated with dynamics, we perform MD simulations.

The crucial factor for a meaningful MD simulation is an adequate description of intermolecular interactions.[27] There are two approaches to determine these interactions. One employs an electronic structure method (e.g. density functional theory methods) to calculate the interatomic potentials via an "on-the-fly" fashion, which is usually referred to as *ab inito* molecular dynamics (AIMD).[28] Carr-Parrinello molecular dynamics (CPMD) employing pseudopotentials and plane wave basis sets is a widely-used scheme to perform AIMD.[29] The advantage of AIMD is that it can provide an accurate potential energy surface on which nuclei move; the main drawback for it is that it's rather time demanding, which limits its application.[29] The other employs pre-made force fields of which the parameters are fit from either experimental data or *ab initio* calculations, referred to as classical MD. By choosing a proper force field, we

can study more realistic systems (up to 100 nm in length) or events (up to 1 microsecond) with satisfying accuracy.[27]

2.1.2.1 Force Field

Most force field for water and molecules in water employ terms to describe the electrostatics, short-range repulsion and long-range dispersion.

The electrostatic term, arising from the classical interaction between the charge distributions of the molecules, is often described by Coulomb's law using atom-centered point charges.

The repulsion term which results from the Pauli Exclusion Principle that prevents the collapse of the molecules and the dispersion term which arises from correlated fluctuations of the electrons in the interacting molecules, are usually combined into a single term, i.e. Van der Waals (vdW) interaction, which is often described by the Lennard-Jones (LJ) potential.

$$U_{ij} = 4\varepsilon\left[\left(\frac{\sigma}{r_{ij}}\right)^{12} - \left(\frac{\sigma}{r_{ij}}\right)^{6}\right] \tag{2-2}$$

On the right hand side, the r^{-6} term represents the dispersion part and the r^{-12} term represents the repulsion part. For the LJ potential the parameters have a simple physical interpretation: ε is the minimum potential energy, located at $r = 2^{1/6}\,\sigma$, and σ is the diameter of the particle, since for $r < \sigma$ the potential becomes repulsive. Because of its simplicity, efficiency and flexibility, LJ potential is a preferable choice in computations.[27]

MD simulations are mainly performed with periodic boundary conditions (PBC),[25] so it is important to efficiently and adequately compute various interactions with PBC. In the case of van der Waals interactions, using a cut-off is a common strategy, where interactions between

particles beyond the cut-off length are neglected. Empirically, the cut-off length is no less than 2.5 σ for a 12-6 type LJ potential.[25]

In principle, electrostatic interactions between all pairs of point charges in the system have to be taken into account. However, this leads to an $O(N^2)$ problem (with N being the system size), which is computationally formidable for large systems. Practically, in MD programs such as GROMACS[30] and DL_POLY[31], special technique (e.g. Ewald summation) or approximation (e.g. reaction field) is employed to make the calculation of electrostatics affordable.

Ewald summation is the golden standard for calculating electrostatic interactions in a periodic system.[27] The problem in calculating the electrostatics in a neutral periodic system of charged point ions lies in that direct Coulomb summation invokes a lattice sum which is unfortunately conditionally convergent, i.e. the result depends on the sequence used in evaluating the sum. Ewald sum was then proposed to overcome this limitation on the basis of two key amendments.[25] It first makes each point charge effectively neutralized by the superposition of a gaussian charge centered on it with an opposite sign. Then a second set of gaussian charges is also superimposed and centered on the same point charges, but with the same sign as the original point charges to neutralize the first set of gaussian charges. The electrostatic potential is finally split into four terms, as shown in eqn (2-3).[25,27,32]

$$U_c = \frac{1}{2}\sum_{\mathbf{n}}{}' \sum_{i=1}^{N}\sum_{j=1}^{N} q_i q_j \frac{\mathrm{erfc}(\alpha |\mathbf{r}_{ij}+\mathbf{n}|)}{|\mathbf{r}_{ij}+\mathbf{n}|} + \frac{2\pi}{L^3}\sum_{\mathbf{k}}{}' \sum_{i=1}^{N}\sum_{j=1}^{N} \frac{q_i q_j}{|\mathbf{k}|^2}\exp(i\mathbf{k}\cdot\mathbf{r}_{ij})\exp(-|\mathbf{k}|^2/4\alpha^2)$$
$$-(\alpha/\pi^{1/2})\sum_{i=1}^{N} q_i^2 + (2\pi/3L^3)\left|\sum_{i=1}^{N} q_i r_i\right|^2 \qquad (2\text{-}3)$$

They are the *real* space term, *reciprocal* space term, *self*-term and *surface* term, respectively, with three parameters controlling the convergence: the real space cut-off r_{cut}, the width of gaussian charges α, and the maximum reciprocal wave-vector $\mathbf{k}_{max}$.[27] The first two terms are direct results of the first and second amendments, respectively. They are functions of the interatomic distance r_{ij}, which need to be evaluated in each time step of a MD simulation. The self-term is required to remove the self-energy interaction arising from the second set of gaussian charge acting on its own site. The surface term originates from a dipolar layer on the surface of the sphere of simulation boxes.[25] It is expressed as a function of the total dipole moment of the system for vacuum boundary conditions.[33] The *self*- and *surface*-terms are constant and may be calculated in the beginning of a simulation.[27] The cost of a standard Ewald sum scales as $N^{3/2}$.[34]

The Smoothed Particle Mesh Ewald (SPME) method is one of the widely-used modifications of the standard Ewald method in order to reduce the computing cost.[34] The main difference between them is in the treatment of the reciprocal space terms. SPME utilizes an interpolation procedure using B-spline, which makes the sum in reciprocal space be represented on a three dimensional rectangular grid. The computing scaling is then reduced to $N\log(N)$.[34]

The reaction field (RF) method, aka the Onsager reaction field[35], was initially used by Baker and Watts[36] in the simulation of water. It splits the field on a dipole into two parts: the first is a short-range contribution from molecules situated within a cavity R_c, and the second arises from molecules outside R_c which are treated as a dielectric continuum generating a reaction field for the cavity. Any net dipole within the cavity interacts with the dielectric continuum via mutual induction. Therefore, the infinite Coulomb sum is replaced by a finite sum inside the cavity plus the reaction field outside the cavity. The total Coulomb potential is given by eqn (2-4):[37]

$$U_c = \frac{1}{4\pi\varepsilon_0}\sum_{i<j} q_i q_j \left[\frac{1}{r_{ij}} + \frac{B_0 r_{ij}^2}{2R_c^3}\right] \tag{2-4}$$

where R_c is the radius of the cavity, and B_0 is defined as:[37]

$$B_0 = \frac{2(\varepsilon_1 - 1)}{(2\varepsilon_1 + 1)} \tag{2-5}$$

with ε_1 the dielectric constant outside the cavity.

However, the discontinuity of potential at the cavity boundary can lead to large energy fluctuation. This issue is addressed by subtracting the value of the potential at the cavity boundary from each pair contribution. The term subtracted is:[37]

$$\frac{1}{4\pi\varepsilon_0}\frac{q_i q_j}{R_c}\left[1 + \frac{B_0}{2}\right] \tag{2-6}$$

Albeit RF is less accurate than Ewald in calculating electrostatics, it is still useful for its simplicity and efficiency in applications.

Beyond pairwise vdW and electrostatic interactions are many-body interactions. They apply to all kinds of non-additive interactions. In many cases, they are non-trivial.[38,39] For water, polarization, which results from the response of charge to an electric field caused by other charges and dipoles, is the leading term of many-body effects.[40-43] It has been shown that the explicit inclusion of polarization of water molecules can give a better description of structures and energies of water clusters and bulk water.[44] Generally, classical models that explicitly include many-body effects are termed as polarizable models, while those implicitly include many-body effects are termed as non-polarizable models. However, simulations using polarizable models are at least an order of magnitude more expensive than simulations using non-polarizable models. Therefore, non-polarizable models have been dominant in the MD simulations from the beginning when the computing power was very poor. Over the last decade, however, polarizable models have been more and more frequently used in MD due to rapid

improvements of computer hardware and the increasing need for more accurate force fields in MD studies.[40] Meanwhile, non-polarizable models also evolve to more effectively incorporate many-body effects.[45] Because of better balance between cost and accuracy, non-polarizable models are picked in this study. We will also compare the results from non-polarizable models with those from polarizable models to have a better understanding about their drawback.

2.1.2.2 Integrators

Having a proper force field is not sufficient to carry out a MD simulation. We need an adequate algorithm to describe the time evolution of system under Newton's laws of motion. In practice, a finite difference integrator of positions, velocities and accelerations is a good approximation for a simulation of a continuously evolving system. [27]

The Verlet algorithm is perhaps the most popular method of MD integrator.[25] By assuming a small enough time step δt, it constructs an integrator by expanding the positions in a Taylor series.

$$\mathbf{r}(t+\delta t) = \mathbf{r}(t) + \mathbf{v}(t)\delta t + \tfrac{1}{2}\mathbf{a}(t)\delta t^2 + \tfrac{1}{6}\mathbf{b}(t)\delta t^3 + ... \quad \text{(2-7a)}$$

$$\mathbf{r}(t-\delta t) = \mathbf{r}(t) - \mathbf{v}(t)\delta t + \tfrac{1}{2}\mathbf{a}(t)\delta t^2 - \tfrac{1}{6}\mathbf{b}(t)\delta t^3 \pm ... \quad \text{(2-7b)}$$

The addition of eqn (2-7a) and eqn (2-7b) produce the equation for updating the positions as follows:

$$\mathbf{r}(t+\delta t) = 2\mathbf{r}(t) - \mathbf{r}(t-\delta t) + \mathbf{a}(t)\delta t^2 \quad \text{(2-8)}$$

where all odd-order terms (including the velocity term) are eliminated and all higher even-order terms (e.g. δt^4) are omitted. Obviously, the velocities are not required to generate the trajectories. However, they are needed to compute kinetic energy and other quantities related to the

velocities. It is easy to obtain the equation for obtaining the velocities by the difference of eqn (2-7a) and eqn (2-7b).

$$\mathbf{v}(t) = \frac{\mathbf{r}(t+\delta t) - \mathbf{r}(t-\delta t)}{2\delta t} \tag{2-9}$$

It is noted that the design of the Verlet algorithm involves a trade-off of the accuracy of the velocities.[25] Several variations on the basic Verlet scheme have subsequently been developed to address this issue. Among them the widely used ones are the "leap-frog"(LF) and "velocity verlet"(VV) schemes.[25]

In the leap-frog algorithm,[46] the velocities leap over the positions by half a timestep. The corresponding equations are as follows:

$$\mathbf{r}(t+\delta t) = \mathbf{r}(t) + \mathbf{v}(t+\tfrac{1}{2}\delta t)\delta t \tag{2-10}$$

$$\mathbf{v}(t+\tfrac{1}{2}\delta t) = \mathbf{v}(t-\tfrac{1}{2}\delta t) + \mathbf{a}(t)\delta t \tag{2-11}$$

$$\mathbf{v}(t) = \tfrac{1}{2}[\mathbf{v}(t+\tfrac{1}{2}\delta t) + \mathbf{v}(t-\tfrac{1}{2}\delta t)] \tag{2-12}$$

The velocities are updated by eqn (2-11) prior to the update of the positions by eqn (2-10). And the current velocities are recovered by eqn (2-12). Although better than the original Verlet algorithm in the accuracy of the velocities, it still does not thoroughly address the issue.[25]

The velocity verlet algorithm,[47] which stores the positions, velocities and accelerations at the same time *t*, further improve the accuracy of the velocities over the leap-frog algorithm. It reads:

$$\mathbf{r}(t+\delta t) = \mathbf{r}(t) + \mathbf{v}(t)\delta t + \tfrac{1}{2}\mathbf{a}(t)\delta t^2 \tag{2-13}$$

$$\mathbf{v}(t+\delta t) = \mathbf{v}(t) + \tfrac{1}{2}[\mathbf{a}(t) + \mathbf{a}(t+\delta t)]\delta(t) \tag{2-14}$$

The new positions at time $t+\delta t$ are calculated using eqn (2-13), yet the new velocities at time $t+\delta t$ are actually calculated in a two-stage fashion, which involves the calculation of the velocities at mid-step using eqn (2-15) and at full-step using eqn (2-16).

$$\mathbf{v}(t+\tfrac{1}{2}\delta t) = \mathbf{v}(t) + \tfrac{1}{2}\mathbf{a}(t)\delta t \quad (2\text{-}15)$$

$$\mathbf{v}(t+\delta t) = \mathbf{v}(t+\tfrac{1}{2}\delta t) + \tfrac{1}{2}\mathbf{a}(t+\delta t)\delta t \quad (2\text{-}16)$$

As a matter of fact, the combination of eqn (2-15) and eqn (2-10) generates eqn (2-13). Apparently, velocity verlet differs from leap-frog only in the scheme for the velocities update. However, this small change makes velocity verlet be more robust than leap-frog and becomes the most popular integrator in molecular dynamics.[25]

Besides on widely used Verlet methods, a more rigorous integrator has also been derived from the Liouville equation, such as multiple time step methods.[27]

2.1.2.3 Ensemble Constraints

MD simulations can be conducted on different types of thermodynamic ensembles to describe different types of thermodynamic systems, such as isolated systems, closed systems, and open systems. An isolated system is handled by the micro-canonical ensemble (NVE) in which the number of particles (*N*), the volume (*V*), and the energy (*E*) are conserved. A closed system is handled either by the canonical ensemble (NVT) in which the number of particles (*N*), the volume (*V*), and the temperature (*T*) are conserved, or by the isothermal-isobaric ensemble (NPT) in which the number of particles (*N*), the pressure (*P*), and the temperature (*T*) are conserved. An open system is handled by the grand canonical (μVT) ensemble in which the chemical potential (μ), the volume (*V*), and the temperature (*T*) are conserved.[25] In this thesis, only isolated systems and closed systems are concerned, thus, NVE, NVT or NPT ensembles are applied in simulations.

The NVE ensemble is the simplest ensemble and usually the default one for MD simulations. It has no constraints of temperature and pressure. The kinetic energy and potential energy can be mutually transformed to each other, while the total energy is conserved. [27]

The NVT ensemble is the simplest extension to the NVE ensemble. The fix of *T* instead of *E*, enables the exchange of heat. In a MD simulation, *T* is controlled by a thermostat. Different types of thermostat have been proposed, including the differential thermostat (e.g. Gaussian thermostat[48]), the proportional thermostat (e.g. Berendsen thermostat[49]), the extended system thermostat (e.g. Nosé-Hoover thermostat[50]), and the stochastic thermostat (e.g. Andersen thermostat[51]).[27]

The NPT ensemble is an extension to the NVT ensemble because it allows for volume fluctuations to obtain a desired average pressure. It needs a barostat for the control of *P* as well as a thermostat for the control of *T*. Common barostat techniques include the proportional barostat (e.g. Berendsen barostat[49]) and the extended system barostat (e.g. Hoover barostat[50] and Andersen barostat[51]).[27] For the proportional thermostat and barostat, the strength of *T*- and *P*-coupling is respectively determined by the corresponding relaxation times, τ_T and τ_P.

2.2 COMPUTATION DETAIL

2.2.1 Classical models for water and methane

In methane hydrate, there are two species, methane and water. Methane is a relatively non-polarizable and chemically inert molecule, interacting with water through van der Waals forces as well as electrostatic forces.

There are two major forms of classical model for methane, a united atom model (aka coarse-grained model) and all-atom model (aka atomistic models). The former abstracts methane into a single L-J mass point with no charge on it, so that only Van der Waals interaction between

methane and other species are calculated explicitly and the rotation of methane is neglected.[52-55] The latter simplifies it into a five-point charge model and places an L-J potential on carbon.[56,57] In both cases, hydrogen atoms are free from the vdW interaction.

Classical models of water are a much more complicated story. As early as 1930s, Bernal and Fowler[19] proposed the first realistic interaction potential for water after the discovery of spectroscopic proofs of its V-shaped geometry. In the B-F model, the center of negative charges is shifted from the oxygen atom and placed on the bisector of the HOH angle towards the hydrogen atoms; besides this, a repulsion-dispersion term is added on the oxygen. This prophetic idea was supposed to be able to explain the tetrahedral arrangement of water molecules in the liquid phase.[58] Its correctness, however, had not been proved until the advent of the TIP4P (Four Point Transferrable Intermolecular Potential) water model in 1983.[59] Since the early 1980s, there have been intense investigations on the development of water models. Although until now there exists no universally transferable water model that can address all scientific issues related to water, we have still gained much insight on properties of water through the development and applications of various water models, which has been summarized in Guillot's review.[58] Similar to methane, water models can also be categorized into atomistic models and coarse-grained models. Our work employs both atomistic and coarse-grained methane models and only atomistic water models.

In this work the water models used include the SPC/E[60], TIP4P, TIP4P/2005[61] and TIP4P/Ice[62] models, all of which are rigid non-polarizable models. As one of the two most frequently encountered atomistic water models, SPC/E (simple point charge-extended) model bears the same geometry (O-H bond is 1.0 Å and HOH angle is 109.47 °) as the original SPC (Simple Point Charge) model but with enhanced charges on the atom sites to recover the

polarization in an effective manner. It employs a Lennard-Jones site on the oxygen atom. The TIP4P/2005 and TIP4P/Ice models are variants of the popular TIP4P model. The key feature of TIP4P family of potentials is that the site carrying the negative charge (usually denoted as the M site) is shifted from the oxygen atom along the H-O-H bisector towards hydrogen atoms to give an improved description of the electrostatics.[45] They employ the geometry of the gas-phase monomer (O-H bond is 0.9572Å and H-O-H angle is 104.52 °). By adjusting the charge and the position of the M site, one can optimize the dipole-quadruple force ratio[45] which is proposed to determine the ability of potential models to describe the phase diagram of water. Vega et al. has suggested that TIP4P/2005 model is probably the best among the non-polarizable water models described by a single LJ site and three charges.[63] Recently Conde and Vega recommended TIP4P/Ice model for the study of hydrate formation because it can predict three-phase (solid hydrate, liquid water, and gaseous methane) coexistence temperature in close agreement with the experimental results. [64]

Four combinations of water and methane models are compared in this study: SPC/E + all-atom methane[57] (SPC/E), TIP4P/2005 + all atom methane (TP4/05A), TIP4P/2005 + united-atom methane[52] (TP4/05U) and TIP4P/Ice + all-atom methane (TP4/Ice). The LJ potential parameters between the water and methane molecules are generally determined through the Lorentz-Berthelot combination rule.[25] The parameters of these force fields are summarized in Table 2.4.

Table 2.4 Parameters of various water + methane model combinations.

Parameter		SPC/E	TP4/Ice	TP4/05A	TP4/05U	TP4/SD	TP4/Tr	TP4
H_2O	q_H	0.4238	0.5897	0.5564	0.5564	0.52	0.52	0.52
	q_O[a]	-0.8476	-1.1794	-1.1128	-1.1128	-1.04	-1.04	-1.04
CH_4	q_C	-0.56	-0.56	-0.56		-0.48	-0.24	-0.56
	q_H	0.14	0.14	0.14		0.12	0.06	0.14
H_2O-H_2O[a]	σ[b]	3.1660	3.1668	3.1589	3.1589	3.154	3.154	3.154
	ε[c]	0.650	0.882	0.775	0.775	0.6485	0.6485	0.6485
CH_4-CH_4	σ	3.64	3.64	3.64	3.73	3.50	3.50	3.64
	ε	1.365	1.365	1.365	1.226	0.2761	0.7531	1.365
CH_4-CH_4	σ					2.50	2.50	
	ε					0.1255	0.1255	
H_2O-CH_4	σ	3.40	3.40	3.40	3.44	3.627	3.327	3.397
	ε	0.942	1.097	1.029	1.043	0.5105	0.6989	0.9409
H_2O-CH_4	σ					2.20		
	ε					0.1862		
H_2O-**CH_4**	σ					2.777	2.827	
	ε					0.3391	0.2853	
H_2O-**CH_4**	σ					1.50		
	ε					0.1255		

[a] for all TIP4P and TIP4P-derived water models, the charge on oxygen is placed on the dummy M site.
[b] atoms marked in bold indicate vdW interaction site, [c] the unit of σ is Å, [d] the unit of ε is kJ/mol.

In addition, two specially optimized methane-water pairwise potentials, developed respectively, by Sun and Duan,[65] and by Anderson *et al.*,[66] are used for the calculation of the thermal expansion coefficient of methane hydrate. Both of them make use of the original TIP4P water model and OPLS-AA[67] methane model as the parent model potentials and parameterize the methane-water vdW interaction parameters on the basis of *ab initio* calculations. These two model potentials are labeled as "TP4/SD" and "TP4/Tr", respectively. The TIP4P water + all-

atom methane (TP4) are also used for comparison with TP4/SD and TP4/Tr. Their parameters are collected together with above mentioned model combinations, in Table 2.4.

2.2.2 Model systems of methane hydrate

A cubic sI unit cell containing 46 water and 8 methane molecules was used as the seed for generating all supercells used in simulations. The box dimension was taken to be 12.03 Å, which is the experimental measured unit cell length for the hydrate of ethylene oxide at 248 K.[68] In the initial structure, the positions of the oxygen atoms of the water molecules were taken from the X-ray diffraction structure of the ethylene oxide hydrate,[68] and the orientations of the hydrogen atoms in water molecules were initialized in a random fashion under the constraint of the Bernal-Fowler rules, giving the net dipole moment of the unit cell close to zero. The methane molecules were placed at the centers of cages.

MD simulations were carried out using a fully occupied $2\times2\times2$ supercell. The vdW interactions were truncated at a distance of 10.0 Å, with long-range corrections[25] applied for both energy and pressure. The electrostatics was handled by the SPME method, as described in section 2.1.2.2. The cut-off of electrostatics was also 10.0 Å.

NVT simulations were performed to calculate the average potential energies and pressures. The ensemble constraint was enforced by a Nosé-Hoover thermostat[50] with a relaxation time being τ_T = 0.5 ps. After 200 ps equilibration runs, 600 ps production runs were executed to collect physical information for analysis.

Lattice constants were calculated from simulations at constant pressure (P =1.013 bar) and at different temperatures (T = 50, 75, 100, 125, 150 and 200 K). The NPT ensemble was enforced by Berendsen weak coupling thermostat and barostat[49] with the corresponding

relaxation times being τ_T= 0.1 ps and τ_P = 0.5 ps. The first 100 ps simulation was for equilibration of the system and the subsequent 100-400 ps was for calculating the average cell parameters, i.e. lattice constants.

The radial distribution functions and power spectra were calculated from NVE simulations. A precedent 250 ps NPT simulations were carried out to equilibrate the system. Then, 1.0 ns and 20 ps (at a 0.5 fs timestep) NVE simulations were respectively performed to collect required trajectories for calculating RDF and power spectra.

To evaluate the thermal stability of methane hydrate, simulations using TIP4P/2005 and TIP4P/Ice models as well as SPC/E model were carried out. The same model systems as reported by Myshakin[69] et al. were used. The fully occupied methane hydrate model consists of 1188 water in liquid phase, 1296 water and 243 methane molecules in hydrate phase; the 95% occupied methane hydrate model, which resembles the natural occurring methane hydrate, contains the same number of water molecules in each phase and 230 methane molecules in hydrate phase.

The preparation procedure was the same as the previous work.[69] Production runs were carried out for 6~20 ns (usually 8 ns) in the NPT ensemble, with semi-isotopic pressure coupling allowing the z-dimension to fluctuate independently from the x and y dimensions. Temperature was controlled by a Nosé-Hoover thermostat (τ_T = 2.0 ps) and pressure was controlled by a Parrinello-Rahman barostat[70,71] (τ_T = 4.0 ps). A time-step of 2.0 fs was used in all production simulations. All simulations in this part were performed on the GROMACS package.

2.3 RESULT AND DISCUSSION

2.3.1 Assessment from NVT Simulation

Table 2.5 Calculated properties of methane hydrate from NVT simulations [a] using various force fields.

	avg. P.E. (kcal/mol)			P (kbar)		
Force field	50K	125K	200K	50K	125K	200K
AMOEBA[b]	-11.80	-11.37	-10.91	3.8	1.8	0.0
COS/G2[b]	-11.85	-11.42	-10.98	4.8	2.4	0.1
SPC[c]	-11.48	-11.06	-10.61	7.2	4.9	2.7
SPC/E[c]	-12.38	-11.96	-11.52	9.5	7.1	4.8
TIP4P[c]	-11.51	-11.10	-10.66	8.7	6.3	4.1
TIP4P/Ice[d]	-14.28	-13.86	-13.42	6.9	4.8	2.8
TIP4P/2005[d]	-13.01	-12.59	-12.14	7.9	5.7	3.6

[a] NVT simulations of 2×2×2 supercell with the lattice parameter of 24.06 Å; [b] Ref 72, [c] Ref 73, [d] this work.

The average potential energies per molecule and equilibrium pressures from NVT simulations with the TIP4P/Ice (Tice) and TIP4P/2005 (T05A) models for T = 50, 125, and 200 K are collected in Table 2.5, together with previous results[72,73] obtained for the same conditions with the non-polarizable SPC, SPC/E, TIP4P models and with the polarizable AMOEBA[74] and COS/G2[75] models. The most sophisticated of these force fields is the AMOEBA force field, which serves as the reference in assessing the other models. Both TIP4P/Ice (TP4/Ice) and TIP4P/2005 (TP4/05A) force fields give larger in magnitude potential energies than other force fields. Meanwhile, the TIP4P/Ice and TIP4P/2005 models give less negative pressures than obtained with the TIP4P model. However, they still give much more negative pressure than obtained with the two polarizable force fields.

2.3.2 Lattice Constants and Thermal Expansion

The lattice constant *vs* *T* curve of methane hydrate was investigated by means of NPT simulations with the SPC/E, TP4/05A, TP4/05U and TP4/Ice force fields. Fig 2.4 reports the values of the lattice constant from these simulations as well as the AMOEBA and COS/G2 results reported by Jiang et al,[72] together with those obtained experimentally for CD_4 hydrate[76] and CH_4 hydrate.[77,78] It should be noted that the lattice constants from the two experimental studies of CH_4 hydrate differ by 0.04 Å, which is within the instrumental resolution.[78] The lattice constant measured for CD_4 hydrate is close to the value reported in Ref 78 for CH_4 hydrate.

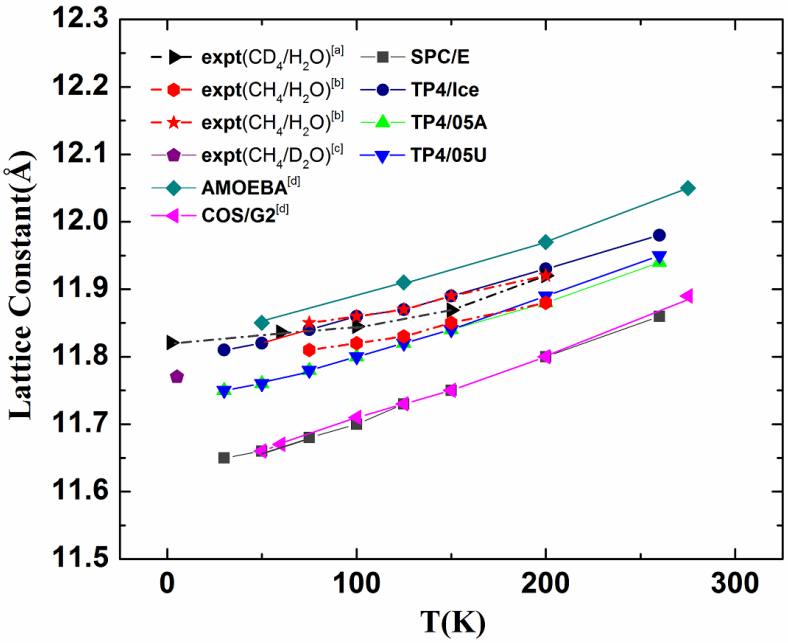

Figure 2.4: Lattice Constants of methane hydrate from MD simulations using various force fields and from experiments. a. from Ref. 76 , b. from Ref. 77 , c. from Ref. 78 , d. from Ref 72.

On one hand, the COS/G2 and SPC/E force fields considerably underestimate the values of the lattice constant, presumably due to their negative charge placed on the oxygen atom. The AMOEBA force field overestimates the lattice constant.

On the other hand, both the TIP4P/Ice and TIP4P/2005 model give a comparable estimation of the lattice constant in excellent agreements with the experimental results. For the TIP4P/2005 model, similar values of the lattice constants were obtained by combining with either united-atom methane model or all-atom one. Since both of them are inexpensive non-polarizable force fields with respect to expensive polarizable force fields, they are preferred for calculating lattice constants of hydrates.

Interestingly, the simulations with all force fields considered give nearly linear lattice constant *vs T* curves, while the experimental curves show appreciable curvature. This difference between theory and experiment is attributed to the neglect of nuclear quantum effects in the simulations.[72]

The coefficient of linear thermal expansion provides another point of view to evaluate the performance of force fields on the description of lattice constants evolving with temperature. The experimentally measured thermal expansion coefficient of ethylene oxide hydrate and methane hydrate,[79,80] together with the calculated ones employing several model potentials from MD simulations, are present in Fig 2.5.

As Fig 2.5 shows, all force fields overestimate the thermal expansivity of methane hydrate compared to experimental determined values. The TP4/05A and TP4/Ice results are comparable, and both of them display less deviation than SPC/E results. This is because TIP4P/2005 and TIP4P/Ice models are better at describing condensed phase water than the SPC/E model.[81] Meanwhile, the calculated thermal expansion coefficients increase noticeably

slower than the experimental one with the increase of temperature. Interestingly, the difference of the trends of thermal expansivity is in agreement with the above mentioned difference of the trends of the lattice constant. In addition, MD simulation results show that fully-occupied MH (FMH) always have larger thermal expansivity than empty MH (EMH), which is independent of the force field used. It indicates that guest species in the cavities can promote the thermal expansion, in agreement with a previous study.[82] And the thermal expansivity is also affected by the type of guest, as the experimental data of ethylene oxide hydrate and methane hydrate indicate.

To examine the guest effect on the thermal expansion of methane hydrate, the quantities evolving with temperature calculated using TP4, TP4/Tr, and TP4/SD model potentials, together with the experimental determined values, are shown in Fig 2.6. These force fields mainly differ in their description of methane-water interactions (see Table 2.4). The comparison of fully-occupied MH and empty MH using the TP4 potential again suggests the promotion role of guest on the thermal expansivity, in agreement with all other water models involved in Fig 2.6. It also shows that the slope of the simulated thermal expansivity of FMH *vs* temperature is larger than that of EMH, although it is still smaller than the experimental value. Meanwhile, changing methane-water interactions merely shifts the thermal expansivity curves in parallel, but does not appreciably change the slope of it.

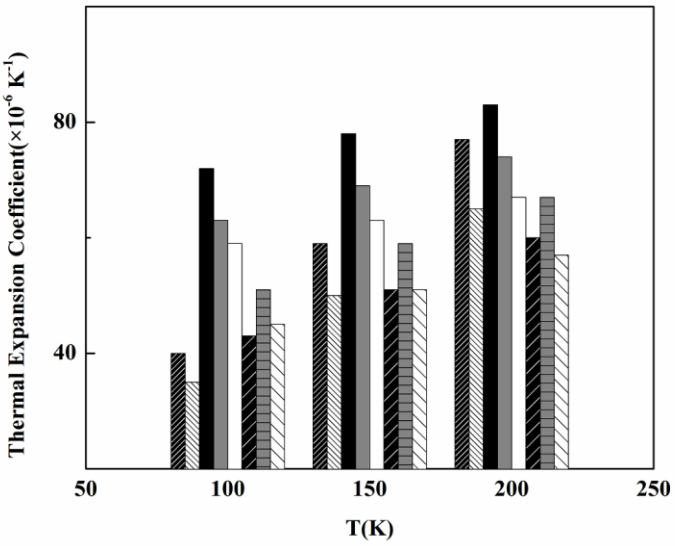

Figure 2.5: Comparison of the coefficient of linear thermal expansion of sI hydrates at T = 100K, 150K and 200K from the experiments and from the MD simulations. The data are clustered according to their corresponding temperatures. In each cluster, the bars from left to right denote ethylene oxide hydrate from experiment (black with dense white strip), methane hydrate (MH) from experiment (white with dense black strip), fully-occupied MH modeled by SPC/E (black), fully-occupied MH by TP4/05A (grey), fully-occupied MH by TP4/Ice (white), empty MH by SPC/E (black with sparse white strip), empty MH by TP4/05A (grey with sparse black strip), and empty MH by TP4/Ice (white with sparse black strip).

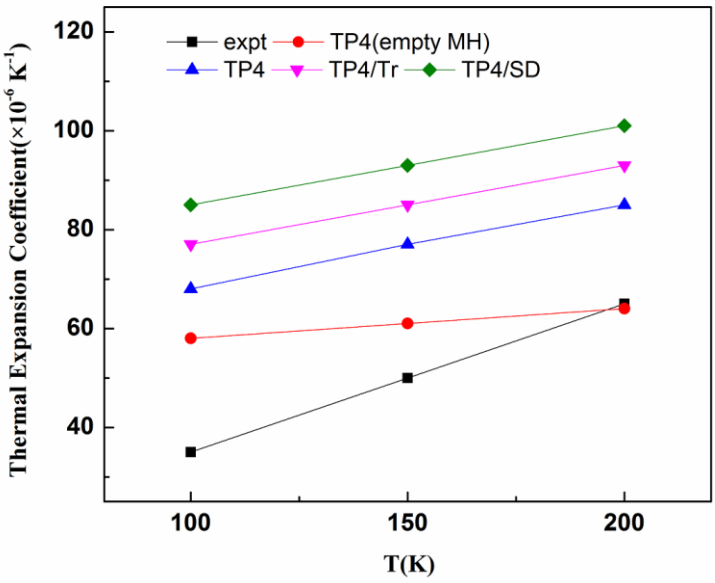

Figure 2.6: Comparison of the coefficient of linear thermal expansion of methane hydrates at T = 100K, 150K and 200K from the experiment and from the MD simulations using TIP4P-water based model potentials.

It is well-documented that the experimental data of lattice constants of sI hydrates as a function of T can be fitted in a quadratic polynomial as[79,80]

$$a(T) = a_0 + a_1 T + a_2 T^2 \tag{2-17}$$

The same formula is applied to all calculated lattice constants from each model potential, with a R^2 larger than 0.99. The resulting constants and coefficients a_0, a_1, and a_2, together with those from experimental data, are collected in Table 2.6.

Substitute eqn (2-17) into eqn (2-1), we have

$$\alpha_1(T) = \frac{2a_2 T + (a_1 + a_2)}{a_0 + a_1 T + a_2 T^2} \tag{2-18}$$

Table 2.6 Comparison of the parameters of the fitting function of lattice constants of sI hydrates from the experiments and the MD simulations.

Species		a_0 (Å)	a_1 (Å/K)	a_2 (Å/K^2)	a_1/a_2 (K)
EOH (expt)[a]		11.835	2.2173×10^{-5}	2.2415×10^{-6}	9.8920
MH (expt)[b]		11.80	5.39×10^{-5}	1.78×10^{-6}	30.3
FMH[c]	TP4/Ice	11.792	6×10^{-4}	5×10^{-7}	1×10^{3}
	TP4/05	11.729	6×10^{-4}	7×10^{-7}	9×10^{2}
	TP4/SD	11.658	8×10^{-4}	1×10^{-6}	8×10^{2}
	TP4	11.641	6×10^{-4}	1×10^{-6}	6×10^{2}
	TP4/Tr	11.628	7×10^{-4}	1×10^{-6}	7×10^{2}
	SPC/E	11.624	7×10^{-4}	7×10^{-7}	1×10^{3}
EMH[d]	TP4/Ice	11.845	4×10^{-4}	7×10^{-7}	6×10^{2}
	TP4/05	11.777	4×10^{-4}	1×10^{-6}	4×10^{2}
	TP4	11.677	6×10^{-4}	4×10^{-7}	2×10^{3}
	SPC/E	11.669	3×10^{-4}	1×10^{-6}	3×10^{2}

[a] EOH, [b] MH, [c] FMH, and [d] EMH respectively denotes ethylene oxide hydrate, methane hydrate, fully-occupied methane hydrate, and empty methane hydrate.

With eqn (2-17) and eqn (2-18), the data in Table 2.6 sheds light on the various differences disclosed in Figs 2.4 - 2.6. In the aspect of lattice constant, the base (a_0) value plays a dominant role in the total value (a). Since the a_0 given by most models (except for TP4/Ice) are noticeably smaller than the one from experiment, these models naturally underestimate the lattice constant. Within simulation data, it is clear that the value of a_0 is sensitive to the choice of water model, and the existence of methane lowers the value of a_0 of empty hydrate. Since a_0 is the low temperature limit of the lattice constant, the decrease of it due to the guest indicates that the attraction is dominant for the guest-host interaction at low temperature.[83] The second factor is the first-order coefficient (a_1) which largely determines the increasing rate of the lattice constant with the increase of temperature. All the coefficients from simulations are one order of magnitude larger than that from experiment. Thus, TP4/05's results approach the experimental values with the rise of temperature while TP4/Ice's results deviate more from the experimental

values at higher temperature. The introduction of guest molecules in the water cavities also result in an increase of a_1. The third one, but a non-trivial one, is the second-order coefficient (a_2), which may have a pronounced effect on the lattice constant when the temperature is high enough. The data show that the experimental data derived a_2 is substantially larger than simulation data derived ones. The remarkable difference between experiment and simulations is also reflected in the ratio of a_1 to a_2. When a_2 is not too small relative a_1, the second-order term can accelerate the increase of lattice constant after some temperature limit, thus *a*-*T* relationship will become a little curve-like, as indicated by experimental data; by contrast, when a_2 is too small relative to a_1, the effect of a_2 on the slope is negligible and the *a*-*T* relationship is virtually linear, as seen in simulation data. In the aspect of thermal expansion coefficient, a_0, a_1, and a_2 all play their respective roles: 1). a_0 mainly affects the absolute value of α_l, because it largely determines the quantity of denominator in eqn (2-18). 2). a_1 also affects the absolute value of α_l, because it affects the base value of numerator in eqn (2-18) in case of very large a_1/a_2 ratio. 3). a_2 mainly affects the increasing rate of α_l vs *T*. Comparison of these coefficients derived respectively from experiment and simulation data shows that: α_l from the experiment is smaller than those from simulations because a_0 is larger and a_1 is smaller in the experiment than in simulations, respectively; meanwhile, the increase of α_l with temperature is greater in experiment because a_2 is larger in the experiment than in simulations. Further, comparison between FMH and EMH from simulations shows that the α_l of EMH is smaller because of larger a_0 and smaller a_1. It again indicates that methane in the cage can promote the thermal expansion of methane hydrate.

In summary, the comparisons of lattice constants, thermal expansion coefficients and parameters of the fitted function of the lattice constant, provide us with abundant information on

the deficiencies of the-state-of-art pairwise water models and the effect of guest-host interactions. The deficiency lies in: first, most of the water models do not predict the correct value of a_0; second, all water models predict too large a_1 and too small a_2, making non-linear response to temperature negligible and thermal expansivity deviated from the experiment in both absolute value and response rate to temperature. Although TP4/Ice gives an a_0 in excellent agreement with experiment, it still has large error in the prediction of a_1 and a_2. The guest effect lies in: it leads to the decrease of a_0 and the increase of a_1 of empty sI hydrate; the change to a_2 varies from different models. However, the change to a_1 and a_2 are limited within the methane-water interaction potential used, leaving the a_1/a_2 ratio still too large. It would be an interesting question to investigate the possible relationship between the three parameters and nuclear quantum effect.

2.3.3 Radial Distribution Functions

The water-water, methane-water and methane-methane radial distribution functions (RDF), were calculated using NVE simulations and the TIP4P/2005 (T05A) and TIP4P/Ice force fields. These simulations were started using equilibrated structures from NPT simulations at T = 200 K and P = 20 bar. Figs 2.7-9 display oxygen-oxygen, oxygen-carbon and carbon-carbon radial distribution functions respectively from the TP4/05A, TP4/Ice force fields, as well as previously reported results for the AMOEBA and COS/G2 force fields. The AMOEBA model has been reported to give structure factors of methane hydrate in excellent agreement with those from neutron diffraction data.[72] It is clearly seen from these figures that all force fields considered give similar results. This indicates that the best non-polarizable water models can describe the structure of methane hydrate as well as polarizable models.

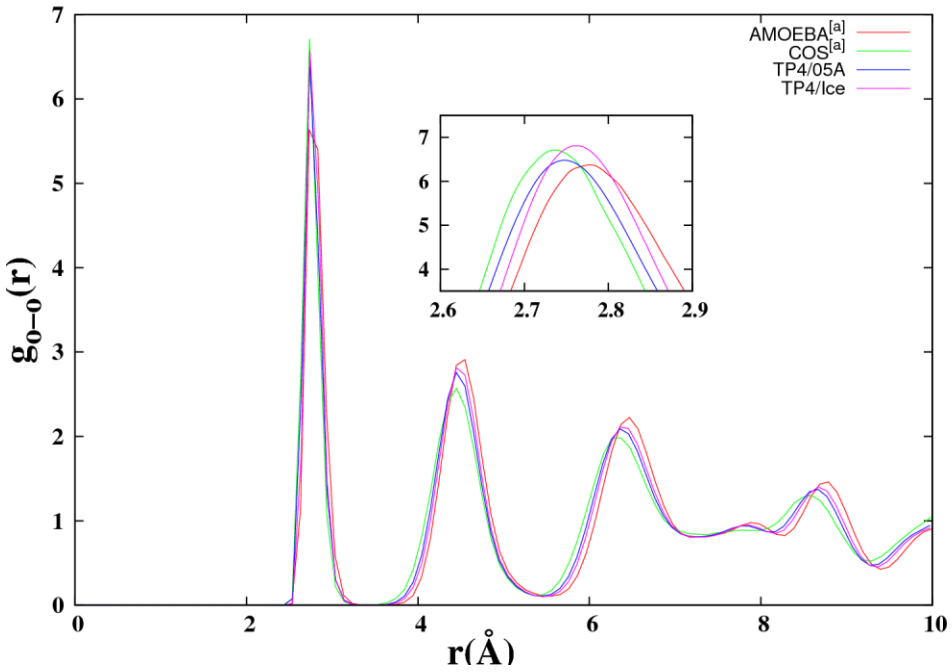

Figure 2.7: Calculated Oxygen-Oxygen radial distribution function $g_{O\text{-}O}(r)$ of methane hydrate at P = 20 bar and T = 200 K. The inset is the magnification of the first peaks. [a] from Ref. 72.

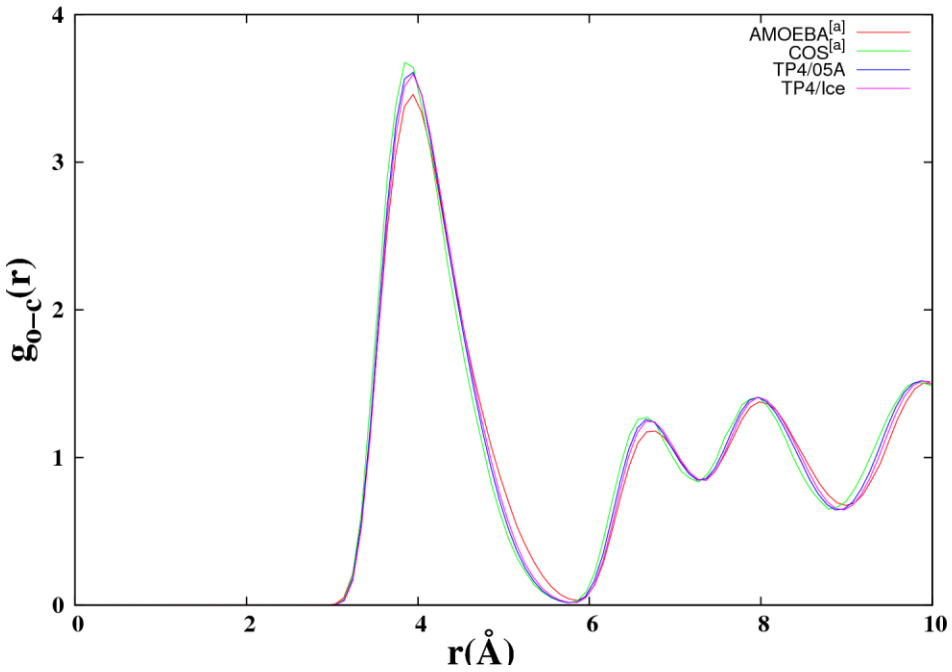

Figure 2.8: Calculated Carbon-Oxygen radial distribution function $g_{C\text{-}O}(r)$ of methane hydrate at P = 20 bar and T = 200 K. [a] from Ref. 72.

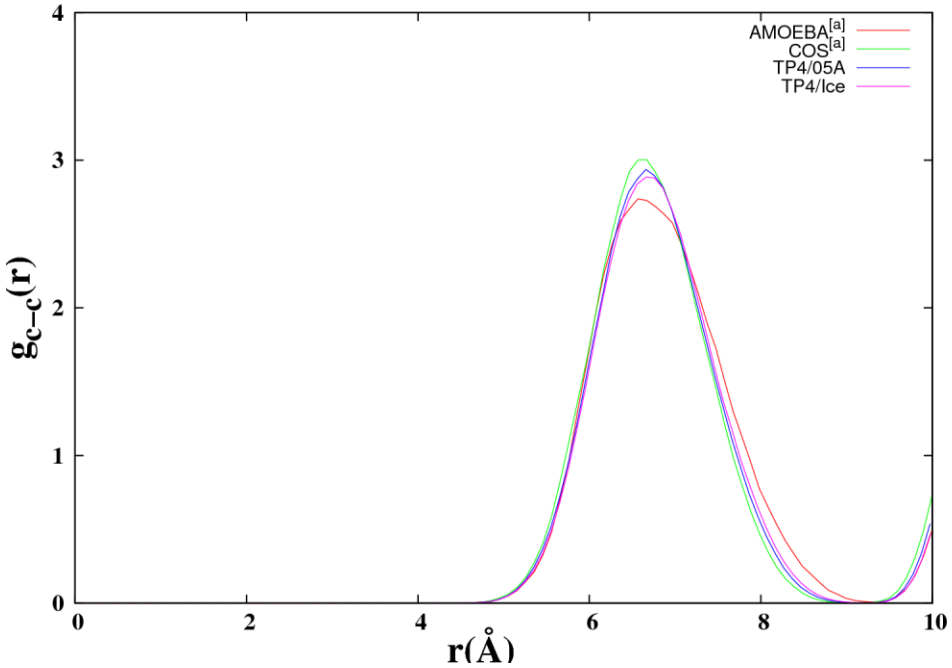

Figure 2.9: Calculated Carbon-Carbon radial distribution function $g_{C\text{-}C}(r)$ of methane hydrate at P = 20 bar and T = 200 K. [a] from Ref. 72.

2.3.4 Power Spectra

English *et al.*[73] and Jiang *et al.*[72] have respectively reported power spectra of methane hydrate at T = 200 K and P = 20 bar using the velocity autocorrelation function (VACF)[84] approach with several different force fields. Overall, polarizable force fields are superior to non-polarizable force fields at predicting the positions of peaks, compared to the experimental results from INS (Inelastic Neutron Scattering) measurement of CD_4 hydrate.[72] In this work, we calculate power spectra using TIP4P/2005 and TIP4P/Ice force fields with the same approach and conditions as used in Ref 72.

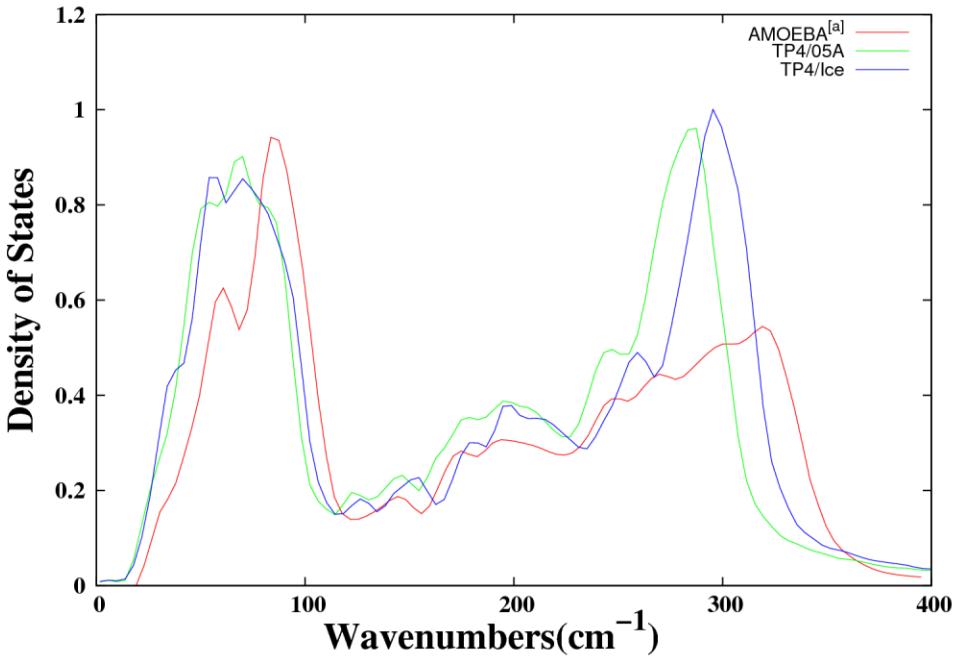

Figure 2.10: Calculated translational spectra of the host lattice of methane hydrate at P = 20 bar and T = 200 K. [a] from Ref. 72.

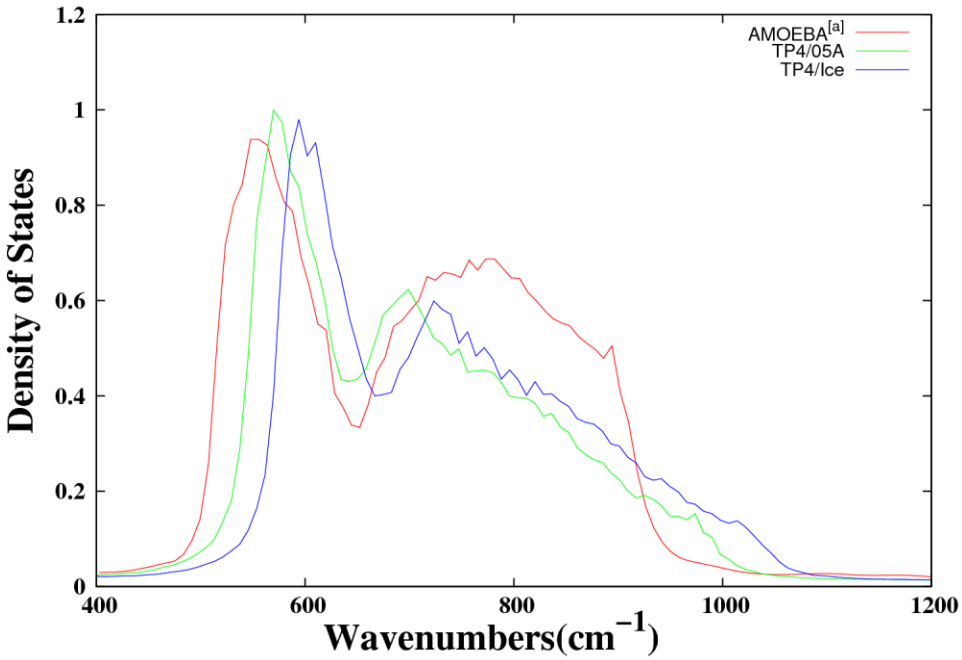

Figure 2.11: Calculated librational spectra of the host lattice of methane hydrate at P = 20 bar and T = 200 K. [a] from Ref. 72.

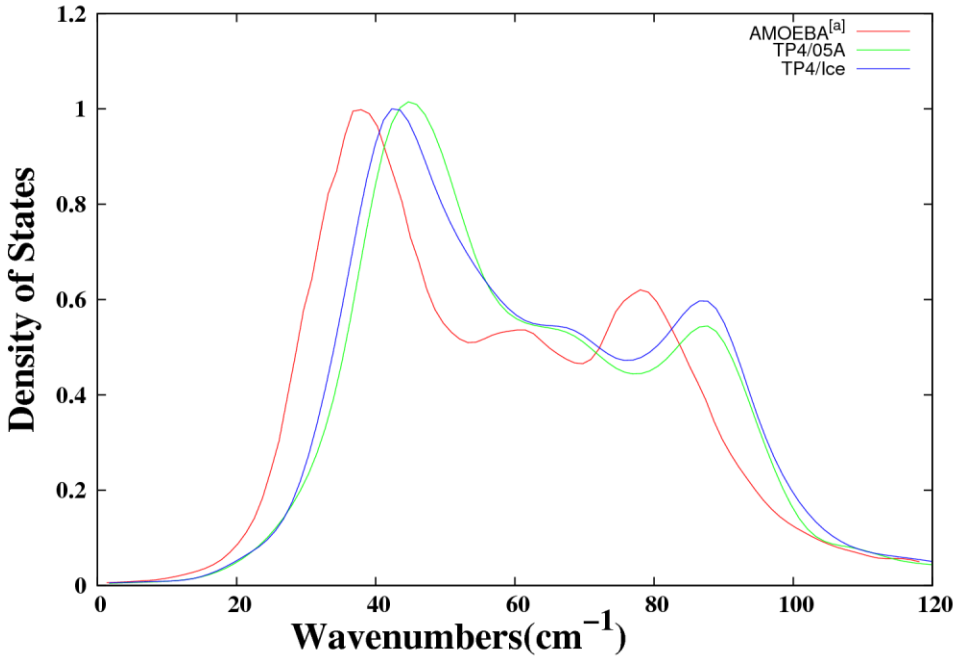

Figure 2.12: Calculated spectra of rattling methane molecules in methane hydrate at P = 20 bar and T = 200 K. [a] from Ref. 72.

Figs 2.10 and 2.11 depict the low-frequency power spectra of the water molecules and Fig 2.12 shows the low frequency spectra associated with the methane molecules. The region shown in Fig 2.10 (0-400 cm^{-1}) is associated with the translation modes of the host lattice.[72] Both TIP4P/2005 and TIP4P/Ice models predict a weak shoulder near 35 cm^{-1}, and pronounced peaks near 55, 65, and 300 cm^{-1}, while the AMOEBA model predicts three peaks (32, 60 and 80 cm^{-1}) below 100 cm^{-1} and one broad peak around 300 cm^{-1}.[72] The peaks below 100 cm^{-1} have been assigned as transverse acoustic modes.[85] Noticeably, the peaks obtained in this work have similar shapes and positions to those calculated using the SPC/E model.[83] However, the relative intensities of these peaks calculated with the non-polarizable force fields differ appreciably from those obtained using the polarizable AMOEBA force field. The TIP4P/2005 and TIP4P/Ice force fields produce a broad peak near 200 cm^{-1}, in agreement with the AMOEBA force field. These

peaks have been assigned to the longitudinal acoustic modes.[85] Fig 2.11 reports the spectra of the water molecule in the 400-1200 cm^{-1} range, which are attributed to the librational motion of host lattice.[72] The spectrum obtained using the TIP4P/2005 model has peaks at 560 and 700 cm^{-1}, and that using the TIP4P/Ice model has peaks at 600 and 720 cm^{-1}. In contrast, the calculations using the AMOEBA model gives peaks at 540 and 770 cm^{-1}. It is also noted that spectra calculated using the TIP4P/2005 and TIP4P/Ice models die off more slowly above 950 cm^{-1} than that calculated using the AMOEBA force field. Unfortunately, there are no experimental data in this frequency range. The spectra associated with the rattling motion of the methane molecules are shown in Fig 2.12. The spectra calculated from different models are in qualitative agreement, all displaying three peaks in the range of 30-95 cm^{-1}. It is well-documented[72,84] that the first two peaks with lower frequencies are due to the translation of methane molecules in large cages, and the third peak with a higher frequency is due to the translation of methane molecules in small cages. The peaks appear at 42, 65 and 88 cm^{-1} with the TIP4P/2005 model, and at 41, 64 and 87 cm^{-1} with the TIP4P/Ice model. The corresponding peak positions in the calculations using the AMOEBA model are somewhat lower, falling at 37, 60 and 80 cm^{-1}. The peaks from the INS experiment[86] are observed at 43.6, 61.3 and 80.7 cm^{-1}. All three models give peak positions in good agreement with experiment, with the results from the AMOEBA model being in better overall agreement with experiment than those obtained using the TIP4P/2005 and TIP4P/Ice models. Comparison of the spectra in Figures 2.10 and 2.12 reveals that the peaks caused by the translational motion of the water molecules are close to those assigned as the rattling modes of the methane molecules, as found in earlier studies[72] and consistent with significant guest-host coupling in this frequency range. As noted in the introduction, this coupling has also been proposed to be responsible for the glass-like thermal conductivity profile of methane hydrate.[87]

2.3.5 Decomposition of Methane Hydrate

The decomposition temperatures of methane hydrate were evaluated by NPT simulations with TP4/05A, TP4/05U, TIP4P/Ice and SPC/E force fields. The purposes are twofold: to evaluate the performances of all non-polarizable models concerned with describing the thermal stability of methane hydrate; to ensure that the crystal structure of methane hydrate can hold up to 260 K, which is the highest temperature used in the NEMD simulations for calculating the thermal conductivity of methane hydrate. The approach used for determining the melting point of ice[81] was employed to calculate the decomposition temperature of methane hydrate

The point when methane hydrate decompose can be evident by such characteristics: the rising of total energy; the periodic z-density of water in the hydrate phase is disappearing and the z-density of water in the liquid phase diffuse; the oxygen-oxygen radial distribution function of water in the hydrate phase shifts from a solid-like figure to liquid-like figure, as shown by Figs 2.13-15, respectively. Fig 2.13 depicts the total energy profile of methane hydrate (95% filled)-liquid water mixture at different temperatures simulated with the SPC/E model. It is easy to see that the total energy undergoes a pronounced rises at 285 K and finally stabilized at a plateau, which is typical for a phase transition. At 290 K, the decomposition is more rapidly and the system even blows up after 5 ns. Fig 2.14 presents the partial densities profile of water at 280 K showing that the region of liquid water (in the middle) is expanding while the region of hydrate (at two ends) is shrinking. Fig 2.15 is the plot of the radial distribution function of oxygen-oxygen atom of hydrate water at 280 K. The rising up of the first trough as well as at the weakening of all crests suggests the transition of water from hydrate phase to liquid phase. Based on these observations, the decomposition temperature of 95% filled methane hydrate is estimated to lie between 280 K and 285 K predicted by the SPC/E water model. Here, we prefer to give a

range where the decomposition occurs instead of an exact value. To obtain an exact number, more (e.g. 3-5) independent and longer (it's 20 ns in a previous study) simulations are required. Furthermore, it may be more accurate to simulate the mixture of three-phase (solid hydrate, liquid water, and gaseous methane) coexistence to calculate the decomposition temperature.[64] In this sense, our simulations served as a quick estimate of these models on the description of thermal stability of methane hydrate. Meanwhile, it is noted that the decomposition temperature range predicted by the SPC/E water model agrees well with the experimental value, i.e. 282.6 K at P = 6.77 MPa.[1] The full filled methane hydrate was also simulated using the same method with SPC/E, which gives a decomposition temperature falling within 285 K and 290 K. The difference is small (5 K). Since methane hydrate in nature are usually 95% occupied, the 100% occupied methane hydrate seems to be a reasonable approximation to study the decomposition temperature. All simulation results of the decomposition temperature in this work, together with the data from the COS/G2 model[69], are summarized in Table 2.7.

Table 2.7 Melting point (T_m) of ice I_h and decomposition temperature of methane hydrate with partial (95%) or full (100%) occupation calculated by two-phase coexistence approach with various models.

T_m	SPC/E	TP4/05A	TP4/05U	TP4/Ice	COS/G2	Expt
Ice I_h	213±2[a]	249±2[a]	249±2[a]	268±2[a]	236±2[b]	273.15[b]
MH(95%)	[280, 285]	[305, 310]			268±3[b]	282.6[b]
MH(100%)	[285, 290]	[310, 315]	[310, 315]	[330, 335]		

[a] from Ref. 81; [b] from Ref. 69.

It can be seen that SPC/E model gives the best estimation of decomposition temperature of methane hydrate but the poorest estimation of melting point of ice I_h; TIP4P/Ice model gives the best prediction of melting point but overestimate the decomposition temperature most (by 50 K); TIP4P/2005 model (the use of either all-atom methane or united-atom methane model makes little difference) underestimate the melting point by 20 K and overestimate the decomposition

temperature by 30 K; COS/G2 underestimates both melting point and decomposition temperature. This part of the simulations has two indications. Firstly, it is clear that at 260 K methane hydrate is far from decomposition. Secondly, no model could give good predictions on both properties simultaneously and it's not simple to tell which one is better than others. However, the gap between the two temperatures may give a criterion. The experimentally observed gap is about 9 K; this number is 32 K for COS/G2, 55 K for TIP4P/2005 and TIP4P/Ice, and 67 K for SPC/E. It is obvious that the polarizable water model is more balanced than non-polarizable model.

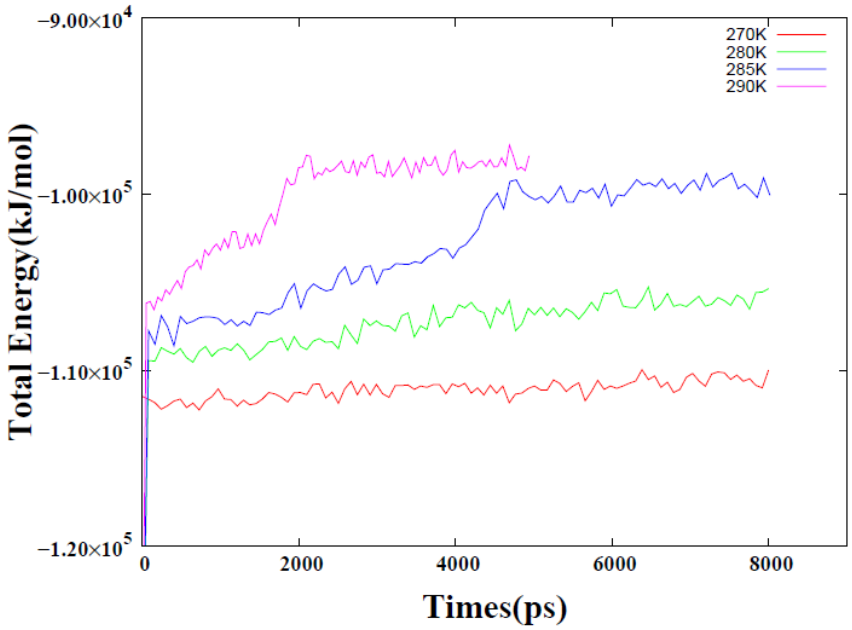

Figure 2.13: Evolution of Total energy of methane hydrate/liquid water mixture with SPC/E model at P = 68 bar.

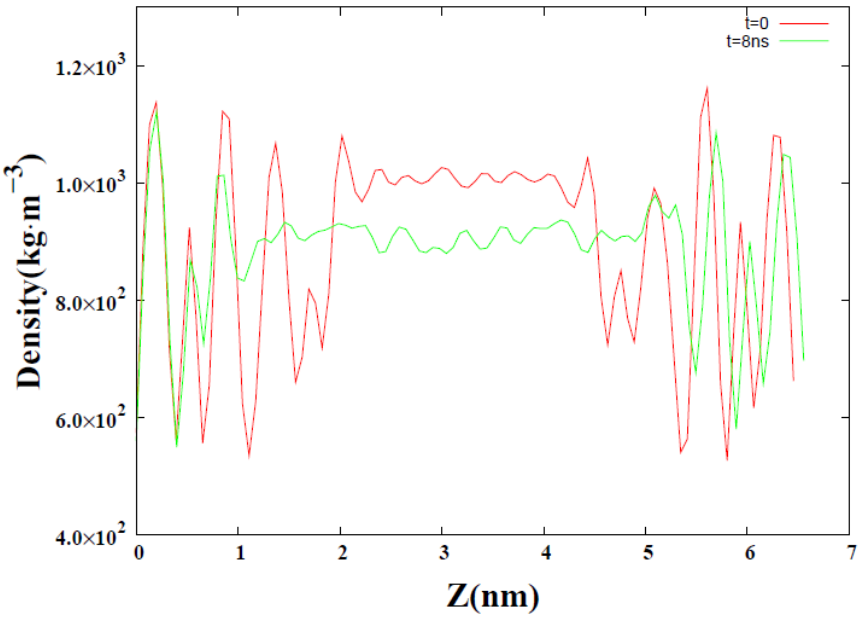

Figure 2.14: Partial densities in Z-direction at the beginning and the end of the simulation of hydrate/water mixture with SPC/E model at P = 68 bar and T = 280 K.

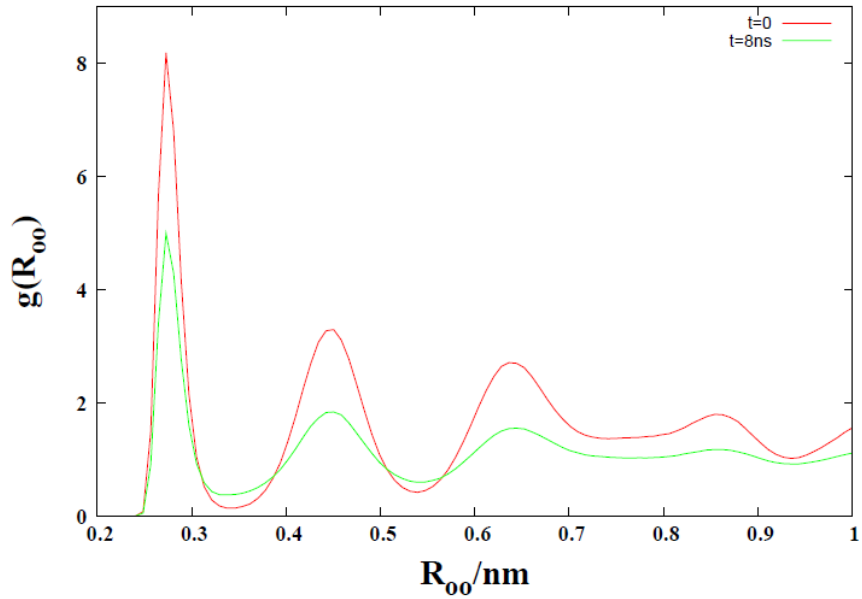

Figure 2.15: oxygen-oxygen radial distribution function in the hydrate phase at the beginning and the end of the simulation with SPC/E model at P = 68 bar and T = 280 K.

2.4 CONCLUSION

This chapter presents our work on molecular dynamics simulations of methane hydrate using several atomistic models, including the SPC/E, TIP4P, TIP4P/2005 and TIP4P/Ice water models, an all-atom point charge and united-atom methane model, and two optimized methane-water vdW interaction potentials. All the water and methane models are non-polarizable and rigid. The properties investigated include lattice constants, thermal expansion coefficient, radial distribution functions, power spectra, and decomposition temperature.

It is found that both TIP4P/2005 and TIP4P/Ice water models do very well in the description of lattice constants and radial distribution functions. Because they have better balance between accuracy and cost than a polarizable water model, it is suggested that pairwise potential with implicit polarization embedded are sufficient for the study of these two properties. Meanwhile, their drawback lies in the overestimation of the thermal expansion coefficient and underestimation of the accelerated increasing of lattice constants, which is common for all non-polarizable water models used in this work. Methane-water interactions are shown to promote the thermal expansion of hydrates, consistent with previous conclusions. However, optimized methane-water pairwise potentials do not address the issue in the description of lattice constant and thermal expansion. Finally, it is found that the SPC/E model can give a very good estimation of the decomposition temperature of methane hydrate. By contrast, TIP4P/2005 and TIP4P/Ice overestimate this quantity by 30 K and 50 K, respectively. This is probably a consequence of too strong interactions between water molecules predicted by these two models.

In future work, a more fundamental factor such as nuclear quantum effects should be investigated in the calculation of lattice constant and thermal expansion. A more sophisticated

simulation technique (such as free energy calculations) may be employed to study the decomposition of methane hydrate.

2.5 ACKNOWLEDGEMENT

This chapter is extracted from a manuscript under preparation: Zhang, G.; Jordan, K. "*A Molecular Dynamics Study of Methane Hydrate on Its Structural and Thermal Properties*". This work was performed in support of the National Energy Technology Laboratory's ongoing research in Subtask 41817.606.06.03.

3.0 THERMAL CONDUCTIVITY OF METHANE HYDRATE

3.1 INTRODUCTION

In this work, nonequilibirum molecular dynamics (NEMD) simulations with the non-polarizable SPC/E, TIP4P/2005, and TIP4P/Ice force fields have been employed to calculate the thermal conductivity of methane hydrate over a temperature range from 30 to 270 K. The calculated thermal conductivities are appreciably larger than the experimental values, but they display the weak temperature dependence found in experiments from T = 100 - 150 K and from T = 225 - 270 K. It is also found that the variation in the thermal conductivity for different proton disordered structures is greater than the standard errors of calculated thermal conductivity. Interestingly, the averaged thermal conductivity from 100 different initial configurations exhibits weak crystal-like character from T = 100 to 150 K. These configurations display partial proton ordering. This is consistent with a recent experimental result (Krivchikov et al., *Low. Temp. Phys.* **2008**, *34*, 648) showing that a proton-ordered THF hydrate sample displays crystal-like behavior in its thermal conductivity.

3.1.1 Overview of Thermal Conductivity of Methane Hydrate

It is well documented that methane hydrate is fundamentally different from ice Ih in thermal conduction, although they are both crystalline materials and have similar hydrogen bond

network.[88-91] While thermal conductivity of ice I_h shows a T^{-1} dependence[89] after reaching a maximum at low temperature, which is typical for a crystal, thermal conductivity of methane hydrates is one order of magnitude less than ice and exhibit weak temperature dependence above 100 K,[92-94] typical for amorphous solids, like glasses. Moreover, methane and other gas hydrates are considered as model systems to investigate the origin of the glass-like behavior of thermal conductivity in other crystalline solids, including semiconductor clathrates,[95,96] and skutterudites.[97,98]

Since the discovery of the unusual thermal conductivity of methane hydrates in 1981,[88] several mechanisms have been proposed.[99-105] In a study of Xe and CH_4 hydrates, Krivchikov et al.,[92,93] described the temperature dependence of the thermal conductivity using four distinctive regions. In regions I and II (from T = 2 to 54 K), $\kappa(T)$ is essentially independent of the type of guest molecule and is well described by the soft-potential model.[106] This model assumes a common origin of the tunneling states and the localized resonant modes. It has been reported to correctly describe the low-temperature thermal conductivity of glasses[106] as well as methane hydrate.[92] In region III (from T = 54 to 94 K), $\kappa(T)$ of methane hydrate decreases by almost 50% as the temperature increases, behavior attributed to the resonant scattering mechanism,[100] also known as guest-host coupling.[101,107] The basic idea of this mechanism is that the low thermal conductivity of gas hydrates is due to phonon-scattering caused by the coupling of the guest rattling modes and the host lattice acoustic modes.[87,108,109] Evidence for such a coupling have been provided by an inelastic x-ray scattering experiment.[110] However, in an earlier study on the methane hydrate, Krivchikov et al[92] showed that the resonant-scattering model only gives a good description of the thermal conductivity below T = 25 K, in addition to neglecting the velocity dispersion. It is worth noted that there is a dip of $\kappa(T)$ near 90 K, which is only observed in Xe

and CH_4 hydrates; for the other hydrates, $\kappa(T)$ is essentially a plateau after climbing to maxima at around T = 75 K.[93] In region IV (above T = 94 K), the phonon mean free path reaches the minimum allowed value(i.e. the Ioffe-Riegel condition[111]), which results in the propagation of the thermal phonons via diffusion.[112] As mentioned by Krivchikov et al., there is no rigorous model being able to quantitatively describe the thermal conductivity of methane hydrate over all the four temperature regions.[93]

However, there are alternative hypotheses concerning the cause of the anomalous thermal conductivity in gas hydrates. Dharma-wardana[99] suggested that the large unit cell of the hydrate causes a constant phonon mean free path, with a value near the lattice constant. This results in the low and weakly temperature dependent thermal conductivity of gas hydrates. This view is supported by a study of the Xe hydrate conducted by Inoue et al.[108] Ahmad and Phillips[113] have proposed in their study of 1,3-dioxolane clathrate hydrate that the structure disorder in the hydrate is responsible for the tunneling state, which leads to the dominant phonon scattering.

Recently, two studies on skutterudites[97,98] (which have similar topologies to gas hydrates) have appeared, which challenged the popular resonant scattering model, and suggest that structural factors may be more important than what is generally believed. Noticeably, Krivchikov et al. [105] found that for the tetrahydrofuran (THF) hydrate, the experimentally measured thermal conductivity is affected by the temperature prehistory of the sample, which is attributed to the effect of the proton ordering. All the proposed mechanisms for explaining the behavior of thermal conductivity of gas hydrates are only partially correct, and fail at describing all the behavior associated with the thermal conductivity of gas hydrates.[95]

In the current study, we extend the non-equilibirum molecular dynamics (NEMD) study previously done in our group, in an effort to understand the origin of the thermal conductivity of

methane hydrate. In the present work, we employ two TIP4P-derived water models, namely the TIP4P/2005 and TIP4P/Ice models. Both models have been proven to perform well at describing the ice phase but have not been extensively used for gas hydrates. Inclusion of both models will allow us to determine their accuracy in calculating thermal conductivity of methane hydrate compared to results from the polarizable COS/G2 force field.[114] Secondly, we investigate the potential impact of the initial configuration of methane hydrate samples on the calculated thermal conductivity, because that the initial configuration is associated with proton disorder.

3.1.2 Methods for calculating thermal conductivity

The thermal conductivity relates the heat flux of the system to the temperature gradient within using Fourier's law for heat conduction,[3]

$$J_{\mu} = -\sum_{\nu} \kappa_{\mu\nu} \partial T / \partial x_{\nu} \tag{3-1}$$

where J_{μ} is a component of the heat current, $\kappa_{\mu\nu}$ is a matrix element of the thermal conductivity tensor, and $\partial T/\partial x_{\nu}$ is a temperature gradient (T-gradient). In experimental studies, κ is obtained by measuring the T-gradient as a result of the stationary heat flux applied on the system of interest. However, in MD simulations, there are two commonly used methods for computing the thermal conductivity. The first method is referred to as the "direct method", which is a non-equilibrium MD (NEMD) method. It imposes a T-gradient across the simulation cell like an experiment, and calculates the thermal conductivity using Fourier's law.[115-117] The second one is referred to as Green-Kubo (GK) method, which is an equilibrium MD (EMD) approach. It utilizes the heat current fluctuations to obtain the thermal conductivity via the Green-Kubo relations.[118,119]

3.1.2.1 NEMD method

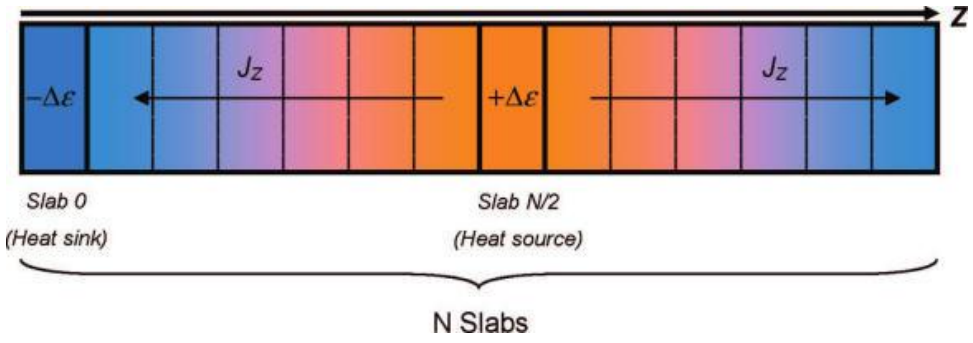

Figure 3.1: A schematic representation of the NEMD method for calculating thermal conductivity. (Retrieved from Ref. 114)

As shown in Fig 3.1, a rectangular simulation cell (replicated by periodic boundary conditions) is divided along the Z direction into N slabs (where N is an even number), with a heat sink and a heat source placed at slab 0 (the cold zone) and slab N/2 (the hot zone), respectively.[114] A constant temperature difference between the heat source and the heat sink is created by steadily subtracting a constant kinetic energy $\Delta\varepsilon$ from the heat sink and adding it to the heat source. Practically, at a regular interval, the center-of-mass (COM) velocities of the molecules in the heat sink (source) slabs are scaled down (up) according to the algorithm of Jund and Jullien,[117] which maintains the conservation of the total momentum. As a consequence, a constant heat flux $\boldsymbol{J}_z$ from the heat source to heat sink, equal to $\Delta\varepsilon/(2A\Delta t)$, is established. Here Δt is the time step, A is the cross-sectional area in the XY plane and the coefficient 2 comes from the fact that energy can flow from the heat source to the heat sink in two directions. The resulting temperature gradient along the Z axis is not evaluated until a steady local temperature is established at the center of each slab. The local temperature of each slab (except slabs 0 and N/2) is then calculated from the time average of the kinetic energy of the molecules in the slab. The temperatures of symmetry-equivalent slabs are then averaged to build up the temperature profile:

$$T_i(Z_i) = \frac{1}{2}\left(\langle T\rangle_i + \langle T\rangle_{N-i}\right) \tag{3-2}$$

where i (which ranges from 1 to N/2-1) is the slab index and Z_i is the Z-coordinate of the center of slab i. The T-gradient can be easily calculated by linear regression because the temperature profile is linear.[117] The thermal conductivity is then calculated via Fourier's law.

In the NEMD method, there are several variables in the set-up, including the magnitude of heat flux, the size of the hot and cold zones, the thickness of the slabs, and the size of the simulation box. Previous studies[115,116,119] have shown that the calculated thermal conductivity is relatively insensitive to the value of heat flux. Specifically, Jund and Jullien[117] have found that the results are independent on the choice of $\Delta\varepsilon$, if $\Delta\varepsilon$ has a value near 1% of k_BT with a timestep of 0.7 fs. In the present work, we employ rigid monomers, which enables a time step of 2 fs and a $\Delta\varepsilon$ of 3% of k_BT. In addition, Chantrenne and Barrat[120] verified that the three numerical parameters that govern the rescaling (i.e. the period of rescaling, the fraction of rescaling and the size of the hot and cold zones) have a trivial effect on the thermal conductivity.

The effect of the system size, (aka "finite-size effects"[119,120]), are caused by artificial phonon scattering from the heat source and the heat sink. The finite-size effects can be recovered by employing an extrapolation procedure based on the kinetic theory of thermal conduction.[121] This expresses the thermal conductivity of a non-metallic solid as the product of the mass density ρ, the specific heat capacity c_v, the effective phonon velocity v, and the phonon mean free path l.

$$\kappa = \tfrac{1}{3}\rho c_v v l = \tfrac{1}{3}\rho c_v v^2 \tau \tag{3-3}$$

where τ is the phonon relaxation time, which is given by $l=v\tau$. Eqn (3-3) is based on two assumptions, namely that the material is isotropic, and the group velocity and the relaxation times are constant with respect to all the phonons presented in the system.[120] For a perfect

crystal, the relaxation times can be decomposed[120] into contributions due to the bulk, and due to the scattering from boundary conditions:

$$\tau_{MD}^{-1} = \tau_{bulk}^{-1} + \tau_{bc}^{-1} \tag{3-4}$$

where τ_{bc}^{-1} is given by

$$\tau_{bc}^{-1} = \frac{v}{\frac{1}{2}L_z} \tag{3-5}$$

where L_z is the length of the Z dimension of the simulation cell. The factor of ½ arises from the fact that the distance between the heat sink and source is one half of L_z.[114] A linear relationship between $1/\kappa_{MD}$ and $1/L_z$ can then be established:

$$\frac{1}{\kappa_{MD}} = \frac{3}{\rho c_v v^2}\tau_{MD}^{-1} = \frac{3}{\rho c_v v^2}\left(\tau_{bulk}^{-1} + \frac{2v}{L_z}\right) \equiv A + \frac{B}{L_z} \tag{3-6}$$

Thus, the thermal conductivity of an infinite system can be obtained by extrapolating the regression line to $1/L_z = 0$, and the effective phonon mean free path is obtained as l_{bulk} = B/2A, where A and B are the intercept and slope of the regression line, respectively.[114]

The linear extrapolation procedure can also be validated from a first-order truncation of a Taylor-series expansion for $\frac{1}{\kappa} = \chi\left(\frac{1}{L}\right)$ where χ is an unknown function of $1/L$ that converges to $1/\kappa_\infty$ as $1/L \rightarrow 0$.[122]

3.1.2.2 The Green-Kubo method

With the Green-Kubo method, the thermal conductivity can be calculated from the equilibrium current-current autocorrelation function

$$k(\tau_m) = \frac{1}{Vk_BT^2}\int_0^{\tau_m}\left\langle \mathbf{J}(\tau)\cdot\mathbf{J}(0)\right\rangle d\tau \tag{3-7}$$

where V is the volume, k_B is the Boltzmann constant, T is the system temperature, **J** is the heat current, and the angular brackets denote an ensemble average. However, since the simulation is performed using discrete time steps of length Δt, the integral in eqn (3-7) can be transformed into a summation.[119]

$$k(\tau_X) = \frac{\Delta t}{Vk_B T^2} \sum_{x=1}^{X} (N-x)^{-1} \sum_{n=1}^{N-x} \left(\mathbf{J}(x+n) \cdot \mathbf{J}(n) \right) \tag{3-8}$$

where τ_X is given by $X\Delta t$ and $\mathbf{J}(x+n)$ is the heat current at the timestep $x+n$. Typically, the total number of integration steps X is considerably smaller than the total number of MD steps in order to ensure a good statistical averaging. The bulk thermal conductivity, which is formally obtained by the limit $\tau_X \rightarrow \infty$, can be recovered as long as τ_X is longer than the relaxation time of the heat current.[119] For the methane hydrate, it has been shown that an integration length of 20 ps is sufficient to provide a reliable estimate of the thermal conductivity.[104]

The time-dependent heat current[119] is given by

$$\mathbf{J}(t) = \frac{d}{dt} \sum_i \mathbf{r}_i(t) h_i(t) \tag{3-9}$$

where $\mathbf{r}_i(t)$ is the time-dependent coordinate of atom i and $h_i(t)$ is the site energy. For a system described by pair-wise additive potential, the site energy is given by

$$h_i = \tfrac{1}{2} m_i \mathbf{v}_i^2 + \tfrac{1}{2} \sum_j u_2(r_{ij}) \tag{3-10}$$

By substituting eqn (3-10) into eqn (3-9), the thermal current becomes

$$\mathbf{J}(t) = \sum_i \mathbf{v}_i h_i + \tfrac{1}{2} \sum_{i \neq j} \mathbf{r}_{ij} (\mathbf{F}_{ij} \cdot \mathbf{v}_i) \tag{3-11}$$

where $\mathbf{F}_{ij}$ is the force on atom i due to its neighbor j from the pair potential. The advantages of using the Green-Kubo method is that it allows the study of anisotropic effects in the thermal

conductivity and finite-size effects are less severe than in the NEMD method; however, it is notorious for its slow convergence.[123]

It has been shown that both NEMD method and Green-Kubo method can give consistent thermal conductivity values with proper choices of parameters.[119] It has been also suggested that for a system with a small phonon mean free path, the NEMD method may be preferable because of the low computational cost.[119]

3.2 COMPUTATION DETAIL

In the current study, we employed the same unit cell as described in chapter 2. The NEMD simulations were carried out with simulation boxes of increasing lengths, and the resulting finite-size thermal conductivity was extrapolated through linear fitting to estimate the bulk thermal conductivity. The simulations boxes were built with ($2\times2\times n$) unit cells of hydrate, with n, the number of unit cells in the Z direction, being 2, 4, 5, 6 and 8 for the SPC/E water model and 2, 3, 4, 5 and 6 for other water models. A $3\times3\times3$ simulation box was used for the Green-Kubo calculations, as recommended by a previous study.[104] We also investigated $4\times4\times4$ simulation box with the Green-Kubo calculations, and found that the result showed that the calculated thermal conductivity $3\times3\times3$ box was indeed converged with respect to the simulation box size.

In NEMD simulations, the thermal conductivity was calculated step-wise at T = 30, 50, 75, 100, 125, 150, 200, 225, 240, 250, 255, 260, 265 and 270 K. A 150-ps NPT (P = 1 atm) simulation was first carried out to equilibrate the system, then a subsequent NVT simulation of 3.0-5.0 ns was then conducted to calculate the thermal conductivity. The temperature and pressure in the equilibration stage were maintained by a Berendsen thermostat (τ_T = 0.1 ps) and

barostat (τ_P = 0.5 ps). It is found there is little difference in equilibrating the system between using Berendsen thermostat & barostat and Nosé-Hoover thermostat & barostat. The temperature in the production stage was maintained by a Berendsen thermostat with a τ_T of 2.0 ps. The use of the NVT instead of the NVE ensemble in the calculation of the thermal conductivity is to prevent the total energy from drifting which would occur if a NVE ensemble was used.[124] In the production run, the simulation box was divided evenly along the Z-axis into 4*n* slabs, and a constant heat flux (6% of k_BT) with a magnitude of 10^{-12} w/Å^2 was imposed along the Z dimension. The first 300-500 ps of each production run was used to establish a steady temperature gradient and was discarded in the averaging process. The procedure and related error propagation rule described in Ref. 114 was employed for calculating standard errors of all of the thermal conductivity values.

In the case of the SPC/E water model, the thermal conductivity of the methane hydrate was calculated using the Green-Kubo method at T = 150 K in addition to the NEMD simulations. The dimensions of the box were determined from a 200 ps NPT (P = 1 atm) simulation with a Berendsen thermostat (τ_T = 0.2 ps) and barostat (τ_P = 1.0 ps). The system was then equilibrated via a 500 ps NVT simulation with a Nosé-Hoover thermostat (τ_T = 0.5 ps), followed by a 5.0 ns NVE simulation in order to collect the real-time heat flux data, for calculating the heat flux autocorrelation function. The thermal conductivity was obtained then through *fast Fourier transform* (FFT) technique. The first two steps used a time-step of 2.0 fs, a cut-off of 10.0 Å, and smooth particle mesh Ewald (SPME) method for electrostatics. The final step used a time-step of 0.5 fs, a cut-off of 11.0 Å, and the reaction field (RF) method for electrostatics.

To investigate the effect of proton disorder on the thermal conductivity of methane hydrate, NEMD simulations were carried out with the SPC/E force fields on 100 initial structures

differing by their proton arrangements. These configurations are generated using a Monte Carlo algorithm proposed by Buch and Sandler.[125] In order to gain a better understanding on the proton arrangement of these configurations, proton order parameters are also calculated using the algorithm proposed by Rick and Freeman.[22]

All MD simulations in the current study were performed using a modified version of the DL_POLY2 program in which the NEMD and GK methods had been implemented as describe by Jiang et al.[114]

3.3 RESULT AND DISCUSSION

The thermal conductivities obtained from the NEMD simulations using various non-polarizable models, together with the experimental data collected by Krivchikov et al.,[93] are plotted in Fig 3.2.

3.3.1 Model potentials

The κ vs T curves obtained using the TP4/Ice, TP4/05A, TP4/05U, and the SPC/E water models are similar, increasing from 30 to 50~75 K and then decreasing for still higher temperatures, albeit with one or more small peaks. These trends roughly resemble the trend that is found experimentally, although the experimental thermal conductivity curve displays a more pronounced dip near 90 K, whereas the calculated curves either lack a dent or display only a small dent near this point.

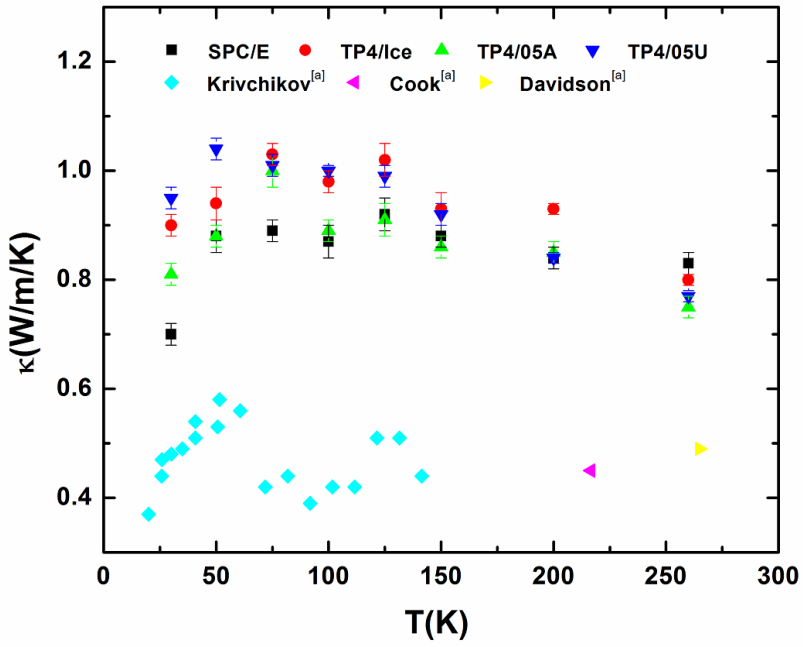

Figure 3.2: Comparison of thermal conductivities from NEMD simulations of a single initial configuration with various force fields and from experiments (a. from Ref. 92).

Quantitatively, all models used in this work overestimate the thermal conductivity by roughly a factor of two. While the TIP4P/2005 and the TIP4P/Ice water models do a good job at predicting the structural properties (e.g. lattice constants and radial distribution functions) as well as the thermodynamics properties (e.g, triple point[64]) of methane hydrate, they are far from being successful at predicting the thermal conductivity. In this context, it is relevant to note that Jiang and co-workers[114] found that the calculated thermal conductivity of methane hydrate using a polarizable model is significantly lower and in closer agreement with experiment.

Fig 3.3 depicts the calculated phonon mean free path (l) obtained from various force fields. Interestingly, while the l obtained using TP4/05U decreases monotonically with increasing temperature, for the TP4/05A, TP4/Ice and SPC/E force fields, there is a small peak in l between 50 and 75 K. The phonon mean free paths are apparently smaller with the SPC/E water

model than with any of the TIP4P based models. The effective phonon velocity (v) increases monotonically with increasing temperature for all the force fields considered. However, phonon velocities calculated with the SPC/E water model are appreciably larger than those calculated with the TIP4P-based models. As a previous work suggests, a smaller phonon mean free path is associated with stronger phonon-phonon interaction and a larger effective phonon velocity is associated with greater phonon dispersion.[114] Since the TIP4P-derived water models all have larger potential energies than the SPC/E water model (Table 2.5), it is speculated that for a non-polarizable model a larger potential energy could result in a longer phonon mean free path (meaning weaker phonon-phonon interaction) and smaller phonon velocity (meaning less phonon dispersion). These effects would then lead to a greater thermal conductivity of methane hydrate. Contrary to the non-polarizable models (which overestimate the phonon mean free path), the polarizable COS/G2 model predicts a nearly temperature-independent mean free path near 0.5 nm for $T \geq 100$ K.[114] Meanwhile, the phonon mean free path of THF hydrate[112] deduced from the experimental data using eqn (3-3) exhibits a different trend than simulation results of using these non-polarizable models, as it shows T^{-1} dependence below T = 100 K and a steady value between 0.4-0.5 nm above T = 100 K. This is because all other variables in the eqn (3-3) are almost unchanged for experimental measurements above T = 100 K (which is about half of the Debye temperature Θ_D of THF hydrate), including thermal conductivity, specific heat, and phonon velocity (in their calculations v was fixed to be 1871 m/s).[112] It is noteworthy that the COS/G2 polarizable water model gives a phonon mean free path close to the experimental value for $T \geq$ 100 K, which accounts for its better description of the thermal conductivity of gas hydrates than non-polarizable water models.

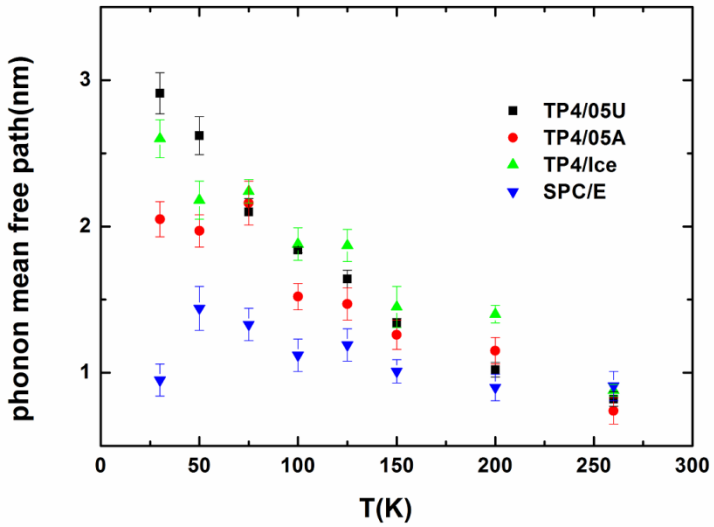

Figure 3.3: Effective phonon mean free path calculated from the NEMD simulations.

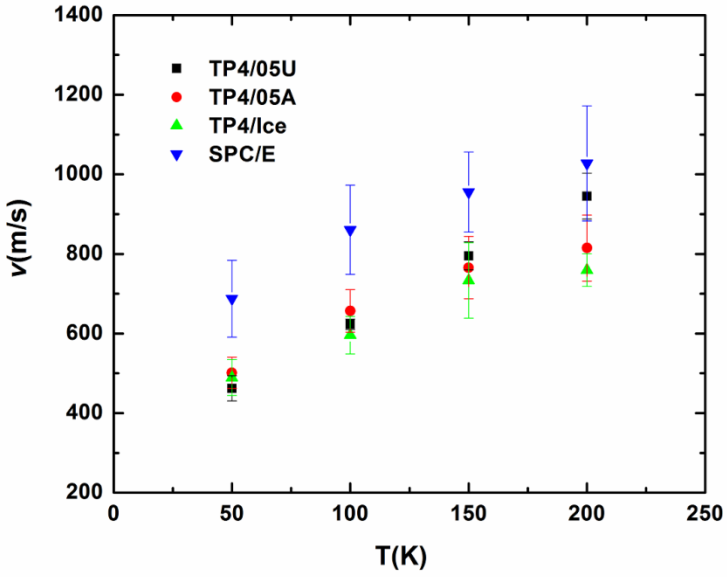

Figure 3.4: Effective phonon group velocities from the NEMD simulations.

3.3.2 Error Analysis of Thermal Conductivity Calculation

In NEMD simulations, calculated thermal conductivity values are susceptible to errors due to statistical thermal fluctuations of the temperature gradient established between the heat source and the heat sink.[126] In this section, we examine the convergence of our calculations by carrying out simulations at T = 125 K with different initial velocity distributions, and average the results in order to reduce the error. In principle, this should be equivalent to a one-time simulation with a time scale five times as long as the original simulation. However, if the time for the complete equilibration is much longer than that of a single long simulation, the two approaches could give different results.

As Table 3.1 shows, in the NEMD simulations of methane hydrate, for a specific configuration, different production runs of 5.0 ns started with different initial velocity distributions can give thermal conductivity values that differ by upwards of 6%. Since the extrapolating results in NEMD can magnify the error due to statistical thermal fluctuations,[127] using different sets of individual values from one-time runs for the extrapolation can lead to a > 6% uncertainty on the bulk thermal conductivity values. As seen from Table 3.2, the difference between extreme values of the thermal conductivity varies from 0.06 to 0.13 $W \cdot m^{-1} \cdot K^{-1}$ for individual configurations, which corresponds to 6-14% statistical errors. This is indicative of the inadequacy of using results from one-time NEMD simulations. To obtain reliable thermal conductivity values from the NEMD simulations, it is important to use mean values obtained by averaging the results of several separate simulations initiated with different initial conditions.

Table 3.1 Finite-size thermal conductivities ($W \cdot m^{-1} \cdot K^{-1}$) from five NEMD simulations of 5.0 ns at T = 125 K.

	2 ×2 ×2	**2 ×2 ×4**	**2 ×2 ×5**	**2 ×2 ×6**
Group1[a]	0.4492 ±0.0063	0.6017 ±0.0110	0.6428 ±0.0045	0.6772 ±0.0097
	0.4625 ±0.0078	0.5975 ±0.0139	0.6264 ±0.0078	0.6797 ±0.0076
	0.4524 ±0.0100	0.6027 ±0.0081	0.6220 ±0.0090	0.7016 ±0.0085
	0.4444 ±0.0106	0.5816 ±0.0095	0.6424 ±0.0078	0.6943 ±0.0089
	0.4481 ±0.0078	0.5952 ±0.0073	0.6357 ±0.0072	0.7061 ±0.0090
Average	0.4513 ±0.0085	0.5957 ±0.0099	0.6339 ±0.0073	0.6918 ±0.0087
Group5	0.4457 ±0.0073	0.5915 ±0.0079	0.6548 ±0.0062	0.7091 ±0.0076
	0.4497 ±0.0089	0.6100 ±0.0098	0.6483 ±0.0081	0.7042 ±0.0073
	0.4502 ±0.0030	0.6018 ±0.0075	0.6412 ±0.0062	0.7192 ±0.0081
	0.4651 ±0.0066	0.5975 ±0.0066	0.6623 ±0.0113	0.7021 ±0.0081
	0.4424 ±0.0091	0.6024 ±0.0086	0.6652 ±0.0060	0.7156 ±0.0093
Average	0.4506 ±0.0070	0.6006 ±0.0081	0.6544 ±0.0076	0.7100 ±0.0081
Group46	0.4573 ±0.0101	0.6121 ±0.0104	0.6560 ±0.0067	0.7035 ±0.0050
	0.4602 ±0.0063	0.6308 ±0.0108	0.6383 ±0.0060	0.7045 ±0.0088
	0.4501 ±0.0104	0.6193 ±0.0064	0.6517 ±0.0062	0.7039 ±0.0075
	0.4450 ±0.0083	0.6510 ±0.0111	0.6395 ±0.0067	0.6988 ±0.0061
	0.4699 ±0.0063	0.6227 ±0.0081	0.6515 ±0.0107	0.7108 ±0.0081
Average	0.4565 ±0.0083	0.6272 ±0.0093	0.6474 ±0.0073	0.7043 ±0.0071
Group48	0.4689 ±0.0055	0.6216 ±0.0073	0.6420 ±0.0119	0.7134 ±0.0055
	0.4716 ±0.0076	0.6162 ±0.0077	0.6589 ±0.0037	0.7121 ±0.0064
	0.4742 ±0.0082	0.6318 ±0.0127	0.6662 ±0.0049	0.7161 ±0.0074
	0.4663 ±0.0130	0.6167 ±0.0088	0.6623 ±0.0084	0.6997 ±0.0065
	0.4633 ±0.0076	0.6236 ±0.0106	0.6620 ±0.0088	0.7163 ±0.0057
Average	0.4689 ±0.0084	0.6220 ±0.0094	0.6583 ±0.0075	0.7115 ±0.0063
Group55	0.4662 ±0.0095	0.6216 ±0.0065	0.6829 ±0.0103	0.7361 ±0.0050
	0.4629 ±0.0074	0.6356 ±0.0118	0.6784 ±0.0070	0.7149 ±0.0056
	0.4661 ±0.0132	0.6178 ±0.0081	0.6802 ±0.0090	0.7196 ±0.0076
	0.4660 ±0.0091	0.6302 ±0.0078	0.6783 ±0.0095	0.7200 ±0.0052
	0.4626 ±0.0042	0.6260 ±0.0083	0.6792 ±0.0095	0.7170 ±0.0088
Average	0.4647 ±0.0087	0.6262 ±0.0085	0.6798 ±0.0091	0.7215 ±0.0064
Group75	0.4685 ±0.0094	0.6284 ±0.0079	0.6864 ±0.0104	0.7038 ±0.0089
	0.4594 ±0.0093	0.6156 ±0.0080	0.6756 ±0.0099	0.7064 ±0.0066
	0.4578 ±0.0069	0.6141 ±0.0048	0.6843 ±0.0075	0.7084 ±0.0068
	0.4536 ±0.0064	0.6296 ±0.0086	0.6751 ±0.0092	0.7205 ±0.0063
	0.4738 ±0.0099	0.6029 ±0.0060	0.6661 ±0.0096	0.7007 ±0.0076
Average	0.4626 ±0.0084	0.6181 ±0.0071	0.6775 ±0.0093	0.7080 ±0.0072

[a] groupX denotes the *X*th configuration, with the different configurations differing in their proton arrangement.

Table 3.2 Thermal conductivities ($W \cdot m^{-1} \cdot K^{-1}$) from single-run and mean values of multiple runs in NEMD simulations at T = 125 K.

	Group1	Group5	Group46	Group48	Group55	Group75
One-time[a]	0.86 ±0.02	0.89 ±0.02	0.88 ±0.02	0.88 ±0.02	0.96 ±0.02	0.90 ±0.02
	0.96 ±0.03	1.01 ±0.03	1.01 ±0.03	0.97 ±0.02	1.02 ±0.02	1.03 ±0.02
Mean[b]	0.90 ±0.03	0.95 ±0.02	0.95 ±0.03	0.93 ±0.02	0.99 ±0.03	0.96 ±0.03

[a] One-time denotes the values extrapolated from a set of data points in Table 3.1. The upper and lower values represent the estimate of minimum and maximum. [b] Mean denotes the values extrapolated from the averaged data points from Table 3.1.

Table 3.3 Thermal conductivity ($W \cdot m^{-1} \cdot K^{-1}$) of methane hydrate by Green-Kubo calculations at T = 150 K.

	#C1	#C2	#C3
Run 1	0.97	0.77	0.91
Run 2	0.82	0.90	0.88
Run 3	0.77	0.87	0.78
Mean	0.85	0.85	0.86

Similarly, Green-Kubo calculations using 5.0 ns EMD trajectories do not give fully converged values for the thermal conductivity of methane hydrate. As Table 3.3 reports, for each of three different initial configurations (#C1-#C3) that are unrelated to the configurations used in NEMD simulations, the values of thermal conductivity calculated by the Green-Kubo method on the basis of one-time 5.0 ns trajectories started with different velocity distributions, differ by as much as 0.2 $W \cdot m^{-1} \cdot K^{-1}$. It is noted that the 20% uncertainty for the value of the thermal conductivity is in line with the reported error range of the Green-Kubo method from previous studies.[127] The sensitivity of the Green-Kubo approach to the initial velocity distribution is due to the fact that the trajectories are not sufficiently long to achieve ergodic behavior.

3.3.3 Uncertainty of the Experimental Measurement

One of challenges in comparing the calculated and measured thermal conductivities of methane hydrate is that the experimental samples necessarily contain defects of various types.[114] Moreover, the methane hydrate samples generally used for the measurements tend to be highly porous which introduces errors due to the thermal contact resistance between adjacent crystalline grains.[92] To reduce the influence of contact resistance, the pores are filled with helium gas, which has a much lower thermal conductivity (κ_{He}) than the hydrate. By assuming that the heat flow is parallel to the parallel layers of two substances, the effective thermal conductivity κ_{eff} of the sample and the thermal conductivity of the ideal sample κ_{mh} are connected by an empirical formula:[92]

$$\kappa_{eff}(T) = \kappa_{mh}(T)v_{sample} + \kappa_{He}(T)(1 - v_{sample}) \tag{3-12}$$

where $v_{\mathrm{sample}} = V_{\mathrm{sample}}/V_{\mathrm{cell}}$, and V_{sample} and V_{cell} are the volume of the hydrate and cell, respectively. However, even with this approach to attempt to minimize the effects of the porosity on the deduced thermal conductivity, some error still remains.

The effect of the different proton arrangements can also impact the thermal conductivity of clathrate hydrates, as has been noted by Krivchikov et al.[105] In an experimental study, they measured the thermal conductivity of THF hydrate in the interval T = 2-150 K using samples prepared under different growth and cooling conditions. They found that the thermal conductivity of samples processed with normal cooling speed exhibited typical amorphous behavior, while that of samples cooled extremely slowly (and optionally doped with KOH impurity) tended to display crystal-like behavior. The latter has been attributed to the development of a proton ordering state in the sample.[105]

3.3.4 Structure disorder in Methane Hydrate

In the ice Ih and gas hydrates, each proton can be in one of two possible locations. Take ice Ih for example, there are $(3/2)^N$ possible arrangements (with N being the number of water molecules) for all the protons under the constraint of the Bernal-Fowler ice rule. Different proton arrangements are interchangeable through water reorientation, which occurs on a μs time scale at T = 273 K for both ice Ih and methane hydrate.[1] The barrier for water reorientation[128] is quite high and the observed reorientation process is actually dominated by extremely rare defects[22] (less than 1 per 1×10^6 water molecules at T = 273 K). Clearly, a simulation on a ns time scale does not satisfy the ergodic assumption.

The proton disorder of the host lattice of gas hydrates has been considered as a likely source for the glass-like behavior for their thermal conductivity.[105] Interestingly, the low density amorphous (aka LDA) ice has been reported to exhibit an unusual crystal-like behavior in its thermal conductivity in spite of the lack of long-range structure order.[129] Meanwhile, methane hydrate exhibits a glass-like behavior in thermal conductivity although it exhibits long-range order. The reason for the crystal-like thermal conductivity of the LDA ice has been attributed to the short-range order, which allows a fairly long phonon mean free path.[129] Likewise, it is possible that the short-range order in methane hydrate may not hold because of the proton disorder of the water network. Therefore, it is helpful to examine whether the proton disorder has any impact on the thermal conductivity of methane hydrate by running simulations on several independent configurations.

By using the averaging procedure described in section 3.3.3, we reduced the errors due to the inadequacy of single 5.0 ns production runs, and obtained more robust results from the NEMD simulations, as seen in Table 3.2. It is noted that the variation of thermal conductivity

values among the selected configurations in Table 3.2 exceeds the error bar in the thermal conductivity for a single structure. This implies that there exists a non-negligible difference in the calculated thermal conductivity values for the methane hydrate starting from different initial structures.

We also averaged the thermal conductivity values of one hundred different initial structures from T = 50 to 200 K using the data obtained from one-time NEMD production runs of 3.5 ns duration. The resulting mean values display a weak crystal-like feature between T = 100 and 150 K, as seen in Fig 3.5. The partial crystal-like behavior may be associated with the proton-ordering character of these initial configurations. As shown in Table 3.4, the percentages of the oblique mirror (OM) water dimer motif in these initial structures are appreciably lower than the theoretical value (2/3) expected for a sample with fully randomly distributed protons. This suggests that, the initial structures generated under the constraint of small net dipole moment may have a bias toward the partially proton ordered configurations. Coincidently, a proton-ordering structure for the THF hydrate has been reported to show crystal-like behavior in the thermal conductivity.[105] It is likely that NEMD simulations using initial configurations with higher proton disorder would generate different TC profiles than obtained in the simulations described above.

We then investigated the thermal conductivity of methane hydrate from T = 225 to 270 K using one initial configuration (group1) with the SPC/E force field. The data points used for the extrapolation are taken from the mean values of five 5.0 ns NEMD simulations started from different velocity distributions. According to section 3.3.3, this procedure can give a converged thermal conductivity for methane hydrate. As depicted in Fig 3.6, it is independent of the temperature, indicating the glass-like behavior of thermal conductivity of methane hydrate in this

temperature range. We found some structural defects in the equilibrated structure prepared for the production run at T = 225 K and higher temperatures. Normally, a water molecule is tetrahedrally coordinated with four neighboring water molecules via hydrogen bonds. However, if there are more than four water molecules surrounding a specific water molecule, a structural defect develops, as seen in Fig 3.7. We also detected rotation of the water molecules without changing the corresponding hydrogen bond orientations. These phenomena, which were not observed at T = 200 K and lower temperature simulations, may contribute to the glass-like behavior of the thermal conductivity of methane hydrate from T = 225 to 270 K.

Table 3.4 Proton order parameters of selective configurations used in NEMD calculations at T = 125K.

	Group1	Group5	Group46	Group48	Group55	Group75
X_{im}	0.554	0.652	0.720	0.671	0.698	0.712
X_{om}	0.446	0.348	0.280	0.329	0.302	0.288

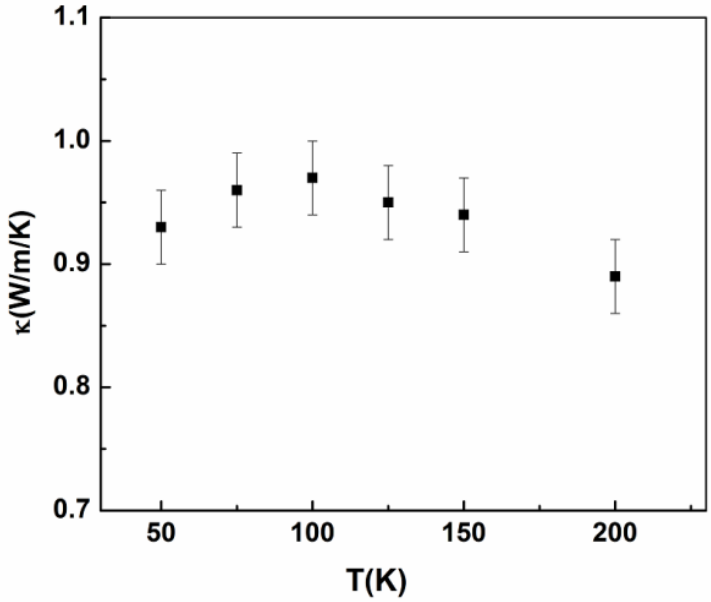

Figure 3.5: Averaged thermal conductivity of methane hydrate obtained from NEMD simulations of 100 different configurations using SPC/E model with one-time production run for each structure.

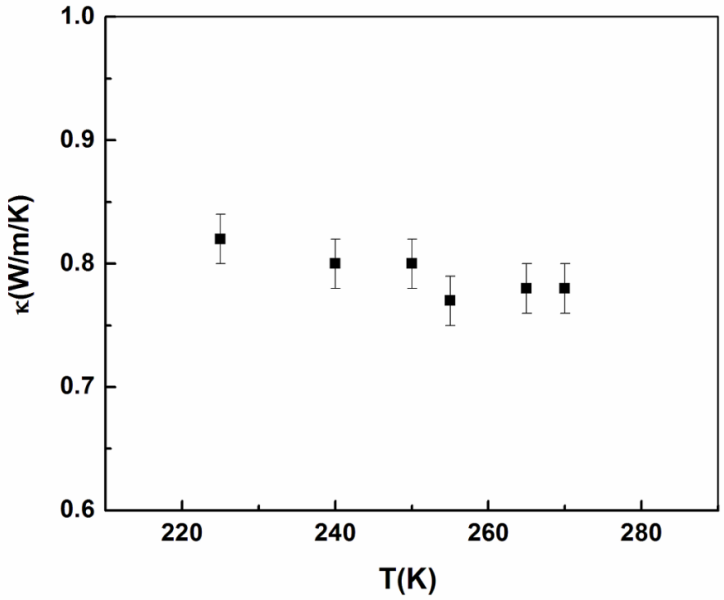

Figure 3.6: Thermal conductivity of methane hydrate obtained from NEMD simulations of one configuration using SPC/E model with five parallel production runs.

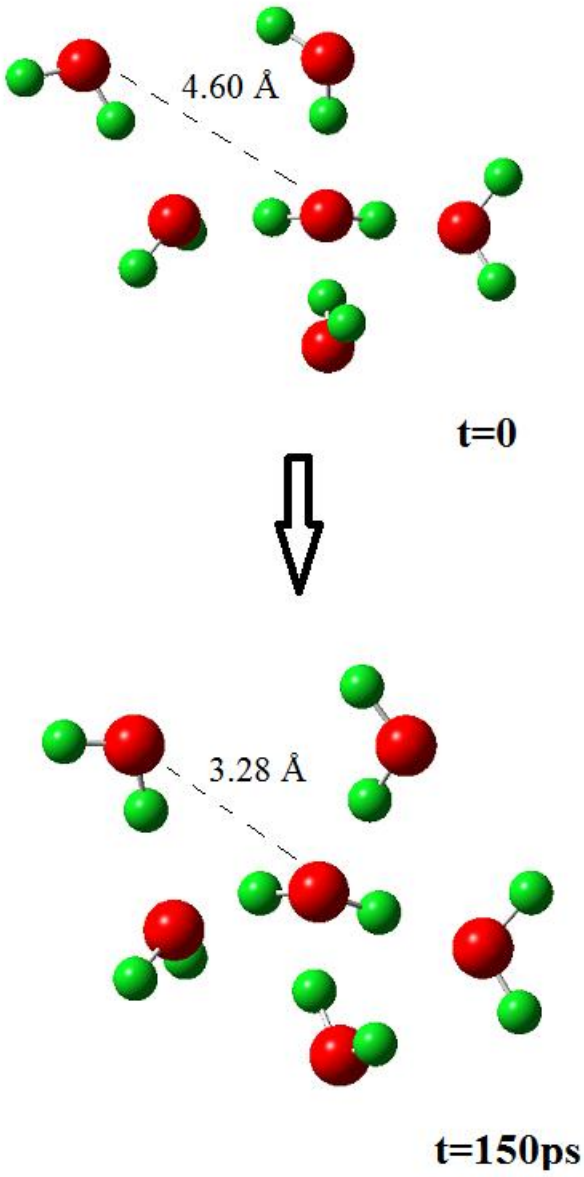

Figure 3.7: Comparison of tetrahedral coordination of a water molecule (top panel) and defected non-tetrahedral coordination (bottom panel) in methane hydrate.

3.3.5 Open Questions

Model Potentials: Two recent independent computational studies on methane hydrate reached different conclusions about the mechanisms impacting the thermal conductivity.[4] On one hand, English *et al*. have suggested that based on the EMD study the glasslike temperature dependence is governed by the guests and the guest-host interactions, and that the lower thermal conductivity relative to ice I_h is caused by the crystal structure of the clathrate framework. They also concluded that the effect of the guest is only important above T = 100 K.[130] On the other hand, in a NEMD study, Jiang et al. found that the impact of guest-host coupling is only appreciable at T = 30 K and it diminishes rapidly with increasing temperature. They suggested that the differences between the lattice structures of methane hydrate and ordinary ice may have a more dominant effect than previously assumed.[83,114] The role of the model potentials, however, has not been carefully examined regarding to the effect on the calculated thermal conductivity of methane hydrate. For example, the models reported to give a relative good estimate of the thermal conductivity of methane hydrate also severely underestimate the thermal conductivity of ordinary ice.[130] Another concern is whether small changes in the methane-water interaction potentials could significantly impact guest-host coupling. Until now, there are only a few published model potentials that are optimized for methane-water interaction.[65,66,131]

Quantum Effects: Nuclear quantum effects have a considerable influence on the properties of liquid water, ice, and clathrate hydrates.[132-139] It has been found that the quantum treatment can give a softer and more flexible structure of ice Ih compared with the classical treatment at the same temperature.[133] Conde et al. recently concluded from a path-integral MD simulation study on the empty gas hydrate that the incorporation of nuclear quantum effect is crucial for the calculation of the densities below T = 150 K.[135] As mentioned in Chapter 2,

current simulations do not correctly describe the trends of the lattice constant and thermal expansion with increasing temperature. It would be interesting to investigate the role of the quantum effects on these properties. If proven important, quantum effects should also be taken into account in the calculation of thermal conductivity.

3.4 CONCLUSION

This chapter presented the results of calculations of the thermal conductivity of methane hydrate using both the NEMD and the Green-Kubo methods. Both the TIP4P/2005 and TIP4P/Ice models (combined with an all-atom methane model), predict larger values for the thermal conductivity than the SPC/E water model (with the same methane model), from T = 30 to 260 K. All model potentials considered overestimate the thermal conductivity by a factor of two, compared with experimental data. However, they are qualitatively consistent with experiment in certain regions: for example, the rise of κ as T increases from 30 to 50 K and its weak temperature dependence from 100 to 150 K.

In addition, the statistical error in both the NEMD and Green-Kubo calculations was investigated. In both methods, non-negligible errors persist when using single production runs of 5.0 ns. It is proposed to use the averaged values from parallel runs with different initial velocities to reduce the statistical noise.

The effect of initial proton orientation (proton disorder) is investigated. We found that different initial structures can give significantly different values. We also noted that all the initial structures used in this work display partial proton-ordering, which may account for the partial crystal-like feature of thermal conductivity profile from T = 100 to 150 K. In addition, structural

defects and rotations of water molecules emerge during the equilibration of system at T ≥ 225 K, which is believed to contribute to the weak temperature dependence of thermal conductivity in this range.

While previous MD studies on the thermal conductivity of methane hydrate have reached different conclusions,[4] we argue that there are several factors deserving more attention. In particular, it appears that the effect of initial proton orientation in simulations may be more important than typically assumed. Secondly, a model correctly describing both ice and gas hydrate is crucial for comparing the difference between them. Currently, there are abundant sophisticated water models for ice; but for gas hydrate, they are rare. Last but not least, we believe that the role of nuclear quantum effects should be investigated.

3.5 ACKNOWLEDGEMENT

This chapter is extracted from a manuscript under preparation: Zhang, G.; Jordan, K. "*A Molecular Dynamics Study of Methane Hydrate on Its Structural and Thermal Properties*". This work was performed in support of the National Energy Technology Laboratory's ongoing research in Subtask 41817.606.06.03.

4.0 WATER LOADING ON THE PYROPHYLLITE (001) SURFACE

4.1 INTRODUCTION

Water adsorption on the (001) surface of pyrophyllite [$Al(OH)(Si_2O_5)$] was investigated using density functional theory (DFT) with dispersion corrections and force field calculations. The DFT calculations show that a water molecule can bind either to one or two basal oxygen atoms of the surface, with adsorption energies varying from -0.10 to -0.19 eV depending on the binding configuration and binding site. Because the water-water interactions are stronger than the water-surface interactions, the energetically preferred structures with two or more molecules on the surface are clusters reminiscent of their gas-phase counterparts. The trend in water-surface binding energies with the number of water molecules obtained from force field calculations qualitatively agrees with that predicted by the dispersion-corrected DFT calculations. However, the force field calculations give a low-energy structural motif with a water molecule coordinated to a hydroxyl group associated with the octahedral layer of the pyrophyllite surface. This binding motif is found to be unstable in the DFT calculations.

4.1.1 Clay minerals: montmorillonite and pyrophyllite

Clay minerals are important components of soils and sediments on the earth. They are composed of sheet silicates (aka phyllosilicates), different from zeolites and quartz which are framework silicates.[17] There are mainly two types of layer structures for them. One bears a 1:1 layer, in which tetrahedral sheets and octahedral sheets stack in an alternate pattern; the other bears a 2:1 layer, in which an octahedral sheet is sandwiched between two tetrahedral sheets, commonly referred to as a TOT layer. Among common phyllosilicates, kaolinite and serpentine have 1:1 layer structures, while mica, vermiculite and smectite have 2:1 layer structures.[140] The most noticeable property of clay minerals is the random isomorphic cation substitutions in their structures, such as Mg^{2+} or Fe^{2+} for Al^{3+} in the octahedral layer, and Al^{3+} for Si^{4+} in the tetrahedral layer. This nature introduces a negative net surface charge, which can be balanced by a cation on the surface. When exposed to aqueous solutions, if water molecules can be intercalated between two negative charged clay layers, they undergo swelling. Kaolinite and mica are non-expansive, while vermiculite and smectite are expansive.[140]

Montmorillonites (MMTs) belong to smectite family.[140] In nature, MMTs tend to be hydrated,[10] which is the subject of many computational studies.[141-152] It has been found that the swelling process is influenced by multiple factors, such as the type of cation, the type of isomorphic cation substitution, interlayer spacing, and the relative humidity. However, due to the large number of different interactions (e.g., water-cation, water-clay substrate, cation-cation, water-water, and cation-substrate)[146] at play, it is difficult to establish the relative importance of each specific interaction on the properties of hydrated clays. Since hydration of clay minerals occur in the interlayer formed by two adjacent (001) surfaces, it is useful to investigate the

water-clay substrate interaction in isolation as a starting point for understanding clay-water interactions. Pyrophyllite is an ideal starting point for understanding the hydration of MMTs.

Pyrophyllite is closed related to MMTs. With a formula of $Al_2[Si_4O_{10}](OH)_2$, it is the simplest structural prototype for 2:1 dioctahedral phyllosilicates.[17] In the octahedral sheet, two-thirds of the available octahedral sites are occupied by aluminum ions and one-third is vacant. The occupied octahedra show a quasi hexagonal symmetry around the vacant octahedron, and two adjacent octahedra are linked by hydroxyl groups.[153] In the tetrahedral sheets, silicon ions are situated at the tetrahedral sites coordinated with three shared oxygen atoms (basal oxygen, O_b) and one unshared oxygen atom (apical oxygen, O_a). Pyrophyllite does not bear a permanent charge in the TOT layer because of lack of isomorphic cation substitutions. It is thus regarded as the uncharged analog of montmorillonites.[17] Due to the nonstoichiometric and inhomogeneous nature of the cation substitutions in MMTs, pyrophyllite is often preferred in modeling these clay minerals.[143]

4.1.2 Density functional theory and the dispersion correction

Kohn-Sham density functional theory (KS-DFT, usually shorten as DFT) provides us with a rigorous and practical framework to calculate the electronic structure of an *N*-electron system.[154] It wisely reduces the intractable many-body problem of interacting electrons into the tractable problem of non-interacting electrons moving in an approximate and self-consistent potential.[155] It solves the one-electron Kohn-Sham equation in a way similar to *ab inito* Hartree-Fock method and describes the electron-electron interaction using an approximate exchange-correlation (XC) functional. The cost is as low as Hartree-Fock method, yet the accuracy can be comparable to MP2 method (a second-order perturbation theory on the basis of HF method).[156] This appealing

balance between accuracy and cost makes DFT grow rapidly and be widely used in various atomic and molecular systems in the last three decades.[157]

DFT methods are not uniformed because of the lack of a universally exact XC functional. Instead, many different forms of approximated XC have been proposed. According to the degrees of their complexities, they are categorized into five rungs from low to high, referred to as the Jacob's ladder of density functional.[155] Among them, the first two are mature and more popular in application. The lowest rung is local density approximation (LDA). The XC in this group depends only on the densities of each point in space. On top of it is generalized gradient approximation (GGA). The XC in this group depends on the gradients of local densities as well as the local densities. There are basically two schools of GGAs. One is parameterized on the basis of empirical data either from experiments or high-level *ab initio* calculations, represented by Becke88 (B88)[158] exchange functional and Lee-Yang-Parr (LYP)[159] correlation functional. The other is built on first principles and known constraints, represented by Perdew-Wang 91 (PW91)[160] functional and Perdew-Burke-Ernzerhof (PBE)[161] functional. To improve the accuracy of GGA, hybrid-GGA, and meta-GGA are respectively developed. Hybrid-GGA mixes a portion of exact HF exchange and a portion of exchange functional to obtain the total exchange energy.[162] Meta-GGA takes the kinetic energy density into account on top of GGA.[155] However, all these functional do not aim to address some challenging issues in the origin, such as charge transfer and non-bonded intermolecular interactions, which in turn limits the application of DFT methods.[157]

It is well accepted that long-range van der Waals force (London dispersion force) is crucial for the description of large systems (beyond molecules) where intermolecular interactions are dominant.[157] Meanwhile, it is well known that the performance of most popular functionals

on simple weakly bound rare gas dimers is poor.[126] Thus, it is necessary to add dispersion correction into current DFT functionals in order to enhance their capabilities of describing non-bonded interactions.

Several approaches have been proposed for correcting DFT for dispersion, including the DFT-D2,[163,164] DFT-D3,[165] and vdW-TS[166] methods at an atom-atom level, the DCACP (dispersion-corrected atom-centered pseudopotential)[167,168] method at atom-electron level, and explicit consideration of non-local interactions as in the vdW-DF[169-171] method. Their basic ideas are summarized in Table 4.1.

Table 4.1 Summary of various methods of dispersion correction to regular DFT methods.

Method	Scheme	scaling
DFT-D2	Adds damped empirical corrections $C_6^{ij}R_{ij}^{-6}$ to DFT energies[a]	N^3
DFT-D3	Adds system-dependent damped empirical corrections $C_6^{ij}R_{ij}^{-6} + C_8^{ij}R_{ij}^{-8}$ to DFT energies[*]	N^3
vdW-TS	Adds damped $C_6^{ij}R_{ij}^{-6}$corrections determined from Hirshfeld partitioning of the charge density[*]	N^3
DCACP	Adds atom-centered Troullier-Martins type pseudopotential terms to DFT energies	N^3
vdW-DF	Adds non-local correlation functional by an integral over the product of densities at **r** and **r'** and a non-local kernel Φ(**r**, **r'**)	N^3

[a] The meanings of these $C_6^{ij}R_{ij}^{-6}$ and $C_8^{ij}R_{ij}^{-8}$ terms can refer to eqn (4-2).

DFT-D2, DFT-D3, and vdW-TS all belong to DFT-D framework, where "D" stands for empirical dispersion correction. The general form of DFT-D energy can be written as:

$$E_{\text{DFT-D}} = E_{\text{KS-DFT}} - E_{\text{disp}} \tag{4-1}$$

where $E_{\text{KS-DFT}}$ is the regular DFT energy, and E_{disp} is the dispersion correction as a sum of two-body ($E^{(2)}$) and three-body ($E^{(3)}$) energies. The two-body term is dominant and generally given by

$$E^{(2)} = \sum_{ij} \sum_{n=6,8,10,\ldots} s_n \frac{C_n^{ij}}{R_{ij}^n} f_{d,n}(R_{ij}) \tag{4-2}$$

where *ij* denotes that the sums go over all atom pairs in the system, C_n^{ij} denotes for the averaged *n*th-order (*n*=6,8,10,…) dispersion coefficient, s_n and f_n denotes the corresponding scaling factor and damping function for each, respectively. The main differences among DFT-D2, DFT-D3 and vdW-TS lie in the parameterization for C_6 term and the choice of damping function. DFT-D3 also involves higher order dispersion terms (e.g. C_8), which is not included in DFT-D2 and vdW-TS. Overall, they are simple, straight forward, and easy to implement in standard DFT codes.

As eqn (4-3) shows, DCACP also takes an additive term to mimic dispersion correction to the regular XC functional, which is similar to DFT-D in some sense.

$$v_{xc}^{\text{extended}} = v_{xc} + \sum\nolimits_I v_I^{\text{DCACP}}(\mathbf{r},\mathbf{r}') \tag{4-3}$$

However, DCACP is distinct from DFT-D by employing an atom-centered pseudopotential form to recover the dispersion interaction, written as eqn (4-4).

$$v_I^{\text{DCACP}}(\mathbf{r},\mathbf{r}') = \sum_{m=-l}^{+l} Y_{lm}(\vec{\mathbf{r}})\, p_l(r)\sigma_1 p_l(r')Y(\vec{\mathbf{r}}') \tag{4-4}$$

Here $\vec{\boldsymbol{r}}$ is the unit vector, r is the distance from nucleus I, l is the angular momentum quantum number and chosen to be 3, Y_{lm} is spherical harmonic, and p_l is the projector.

$$p_l(r) \propto r^l \exp(-r^2 / 2\sigma_2^2) \tag{4-5}$$

It is the merit that DCACP incorporates the electronic effect into the dispersion correction. But it suffers from the issue of transferability and non-negligible deviation from

correct R^{-6} asymptotic behavior.[157] Moreover, it is only available for a few elements in the periodic table.*

vdW-DF adopts a bottom-up approach to build a non-local correlation functional to fix the dispersion issue in regular DFT. It has no empirical parameters, which is different from DFT-D and DCACP. However, it is more numerically complicated than DFT-D approach, and it does not support simple force calculations and thus can only be used in single-point energy calculations. [165]

Among these three different approaches, DFT-D appears to be an attractive framework to the dispersion correction in standard DFT methods.

4.1.3 Targets of this work

The (001) surface of pyrophyllite has been reported as hydrophobic in earlier DFT studies.[172-175] For example, Bridgeman[174] et al. found a positive energy for pyrophyllite swelling, and Churakov[175] calculated that the water-pyrophyllite binding energy is much smaller than the water-water interaction energies, with both of these results being consistent with the hydrophobic nature of the pyrophyllite surface. However, these studies did not include dispersion corrections to the DFT energies, which have been found to be important in characterizing water adsorption on hydrophobic surfaces.[176-180] Therefore, it is desirable to take the dispersion part into account for the surface binding energy calculations in this work. Both the DFT-D2 and vdW-TS methods have been shown to substantially improve the description of the layered structures of montmorillonite and pyrophyllite, and overall DFT-D2 performs slightly better than vdW-TS.[181]

* http://lcbcpc21.epfl.ch/DCACP/DCACP.html

Therefore, in the present work the DFT-D2 method is employed in conjunction with the PBE functional to study water adsorption on the pyrophyllite (001) surface.

Although DFT-based calculations are readily applicable to simple clay model systems, their application to complex clay systems is computationally prohibitive due to the size of the simulation cell that must be employed.[182] As a result, there is considerable interest in the application of computationally less demanding force field methods to clay systems.[182] Several force fields including CLAYFF,[142] phyllosilicates force field (PFF),[183] and MS-Q[184] have been developed for simulations of clay minerals. Thus, it is of interest to compare the structures and stability of water on the pyrophyllite surface obtained using CLAYFF and DFT-D2 calculations. Specifically, we will consider the low-energy structures of one through six water molecules on the surface.

4.2 COMPUTATION DETAIL

The DFT calculations were performed using the Vienna *ab initio* simulation package (VASP[185,186]) and made use of the PBE functional together with D2 dispersion corrections (hereafter denoted as PBE+D2) and periodic boundary conditions. A plane-wave basis set using the projector-augmented wave (PAW)[187] scheme and an energy cut-off of 600 eV was employed. The convergence of the adsorption energies with energy cutoff was confirmed by comparing with the results of calculations using an 800 eV cut-off. Both $1\times1\times1$ and $2\times1\times1$ supercells were used for the calculations. A Monkhorst-Pack[188] sampling of the Brillouin zone was used for generation of the **k**-point grids. Based on previous work[181] on pyrophyllite, a $2\times2\times1$ k-point sampling scheme was adopted. Geometry optimizations were performed with convergence

criteria of 1×10^{-5} eV for the total energy and of 1×10^{-2} eV/Å for the RMS residual force. Only atoms in the top two atomic layers of pyrophyllite (see Fig 4.3) were allowed to relax.[189] This is sufficient to obtain converged interaction energies, as was confirmed by comparison with optimizations allowing all layers to relax. Each optimized structure was confirmed to be a local minimum by carrying out a vibrational frequency analysis.

The interaction energies of water molecules on the surface were calculated as: $E_{int} = E_{cplx} - n \cdot E_{wat} - E_{pyro} - E_{lat}$, where E_{cplx} is the energy of the complex of the adsorbed water molecule(s) plus the surface, n is the number of water molecules on the surface, E_{wat} is the energy of an isolated water monomer, E_{pyro} is the energy of the dry pyrophyllite substrate, and E_{lat} is a correction for lateral interactions between water molecules in adjacent cells as described below. For the calculation of the energy of a single water molecule, a cubic $14\times14\times14$ Å^3 cell was used, which is sufficient to ensure energy convergence. E_{lat} was calculated using $E_{lat} = E_{wat(abc)} - E_{wat(14,14,14)}$, where $E_{wat(abc)}$ is the energy of the water cluster in the same a,b,c cell as used in the slab model calculations, and $E_{wat(14,14,14)}$ is the energy of the water molecule(s) in a $14\times14\times14$ Å^3 cell.[190] In calculating $E_{wat(abc)}$ and $E_{wat(14,14,14)}$, the geometries and orientations of the water molecules were extracted from the optimized surface arrangement. In the case of more than one water molecule, the net interaction energy E_{int} can be decomposed into water-water and water-surface contributions. The latter contribution is calculated as follows: $E_{surf} = E_{cplx} - E_{wat(abc)} - E_{pyro}$.

The force field calculations were performed using the LAMMPS package,[191] with pyrophyllite being described by the CLAYFF force field, which uses the rigid SPC model[60] for the water molecules and a flexible SPC model[192] for the hydroxyl groups of the pyrophyllite. The interactions between atoms include electrostatic, repulsive, and van der Waals (vdW) terms with

the latter two contributions being expressed by Lennard-Jones (12-6) functions. The Lorentz-Berthelot mixing rule[25] was used to obtain the Lennard-Jones parameters for interactions between unlike atoms. Under periodic boundary conditions (PBC), the long-range electrostatics were treated by the particle-particle particle-mesh Ewald (PPPM) solver of Hockney.[193]

Calculations were also carried out with the default SPC water model used in CLAYFF replaced by the SPC/E[60] and TIP4P[59] models, with the modified force fields being designated as CLAYFF-E and CLAYFF-T, respectively. It has been reported that the TIP4P water model performs well for simulating water in clay minerals.[194] Calculations were also performed with a modified CLAYFF force field, designated CLAYFF-M, in which the harmonic potential for the clay hydroxyl groups was replaced by a Morse potential.[195]

The initial structure of the unit cell of pyrophyllite was taken from Ref. 181 where it was fully optimized at the PBE+D2 level. The calculated lattice parameters of the unit cell are: a = 5.18, b = 8.99, c = 20.33 Å, and α = 90.88 º, β = 100.50 ºand γ = 89.82 º. These are in excellent agreement with experimental values.[181] In the electronic structure calculations, a $1\times1\times1$ unit cell was used for adsorption of one water molecule, and a $2\times1\times1$ supercell was used for studying adsorption of two to six water molecules on the surface. An 11 Å vacuum layer (in the c direction) was used to isolate surfaces in adjacent slabs. The binding energy of a single water molecule on the surface was unaffected by increasing the vacuum layer to 15 Å, indicating that the vacuum spacing of 11 Å is adequate. The binding energy was also unaffected by doubling the thickness of the pyrophyllite slab in the c direction. In the CLAYFF calculations, a $4\times2\times1$ supercell with a vacuum layer of 11 Å in the c direction was employed, with an orthogonal lattice having the same lattice dimensions as used in the PBE+D2 calculations. The use of

orthogonal lattice instead of the triclinic one is more computationally efficient, which has been shown not to change the structure of TOT layers.[195]

In the force field calculations a sequence of molecular dynamics (MD) simulations and conjugated gradient optimizations was used to identify low energy structures. The first round of MD simulations was initiated with water molecules placed on the surface with arbitrary arrangements. The simulations were carried out for 25-50 ps in the NVT ensemble at T = 100 K. Twenty configurations were saved at evenly spaced time intervals and then optimized using the conjugate-gradient method. The lowest energy configuration thus obtained was then used to start a 40 ps simulation in the NVT ensemble at T = 10 K. Equilibrated configurations from this simulation were collected every 2 ps and used for another round of conjugate-gradient optimizations. Additionally, some of the initial structures were taken from the optimum DFT structures. The MD simulations were carried out using a 1.0 fs time-step and employed an rRESPA multi-timescale integrator.[196] Geometry optimizations were concluded when the change in energy between two consecutive steps was less than 1.0×10^{-6} of the total energy.

In the electronic structure calculations, the initial configurations of the water molecules on the surface were generated by hand in the cases of one or two water molecule(s) in the supercell, randomly placing the monomers on the surface, and for larger clusters taking the equilibrated structures captured from the CLAYFF MD trajectories.

4.3 RESULTS AND DISCUSSION

Our calculations show that adsorbed water clusters are considerably more stable than isolated water molecules on the surface, and, for this reason, only the cluster results are presented for the

case of more than one water molecule in the supercell. The calculations also reveal that the potential energy surfaces of one or more water molecules interacting with the pyrophyllite surface have myriad minima, generally separated by relatively small potential energy barriers. In the following discussion, we focus on the energetically most favorable structure of each type. Less stable structures are also collected in the corresponding tables and figures.

4.3.1 Water monomer

The structures of the various arrangements of a water molecule on the pyrophyllite surface are depicted in Fig 4.1. The associated geometrical parameters and binding energies are summarized in Table 4.2. In labeling the different binding configurations, it is useful to distinguish between the three types of basal oxygen atoms on the surface. As shown in Figs 4.2 and 4.3, one type (site 1) is on the extended line of hydroxyl groups in the octahedral sheet, and the other two (sites 2 and 3) lie above aluminum atoms in the octahedral sheet. The PBE+D2 calculations identify three potential energy minima (**$1a_1$-$1a_3$**) where the water molecule binds to the surface by donating one hydrogen bond and two potential energy minima (**$1b_1$** and **$1b_2$**) where it binds via two hydrogen bonds. The **$1a_1$**, **$1a_2$**, and **$1a_3$** species are bound at sites 3, 2, and 1, respectively. The water monomer binds more strongly at sites 2 and 3 which are uppermost on the surface than at the deeper-lying site 1. Churakov[175] has shown that electrostatic potential is negative above sites 2 and 3 so that they are effective hydrogen bond acceptors. The **$1b_1$** and **$1b_2$** configurations are bound to the (2, 3) and (1, 3) pairs of sites. The **$1b_1$** structure is found to be the most stable form of the water monomer on the pyrophyllite surface. At the PBE+D2 level, it is bound by -0.19 eV, which is slightly less than the strength of the hydrogen bond of the water dimer, -0.22 eV.[197]

Table 4.2 Structures and binding energies for adsorption of a water molecule on the pyrophyllite surface.

Motif	PBE+D2[a]		CLAYFF (CLAYFF-M)[b]		CLAYFF-E (CLAYFF-T)[c]		Binding
	H_w-O_b (Å)[d]	E_{int}(eV)	H_w-O_b (Å)	E_{int}(eV)	H_w-O_b (Å)	E_{int}(eV)	sites
1a$_1$	2.10(2.28)	-0.14(-0.05)	1.82(1.84)	-0.13(-0.13)	1.87(1.84)	-0.13(-0.14)	3
1a$_2$	2.17(2.35)	-0.14(-0.05)	1.82(1.84)	-0.12(-0.13)	1.88(1.82)	-0.15(-0.14)	2
1a$_3$	2.45(3.10)	-0.10(-0.01)					1
1b$_1$	2.17/2.40	-0.19(-0.06)	2.04/2.07	-0.14(-0.15)	2.04/2.12	-0.15(-0.15)	2,3
	(2.32/2.48)		(2.07/2.16)		(2.04/2.13)		
1b$_2$	2.35/2.51	-0.15					1,3
1c			2.21(2.04)	-0.15(-0.15)		-0.16	2(3)[e]

[a] The results of the DFT calculations with dispersion corrections are given first, and those without dispersion corrections are given in parentheses. [b] The CLAYFF results are reported first with the CLAYFF-M results being given in parentheses. [c] The CLAYFF-E results are reported first with the CLAYFF-T results being given in parentheses. [d] H_w-O_b denotes the hydrogen bonds lengths between water and the surface. [e] **1c** is predicted to be bound at site 2 using CLAYFF and at site 3 using CLAYFF-M.

As seen from Table 4.2, the inclusion of dispersion corrections in the DFT calculations enhances the energy for the binding of a water monomer to the surface by about 0.1 eV (~66 % of the binding energy). The hydrogen bond lengths obtained with PBE+D2 calculations are noticeably shorter than those from the PBE calculations. These results indicate that inclusion of long-range dispersion corrections is important for describing the adsorption of water on the pyrophyllite surface.

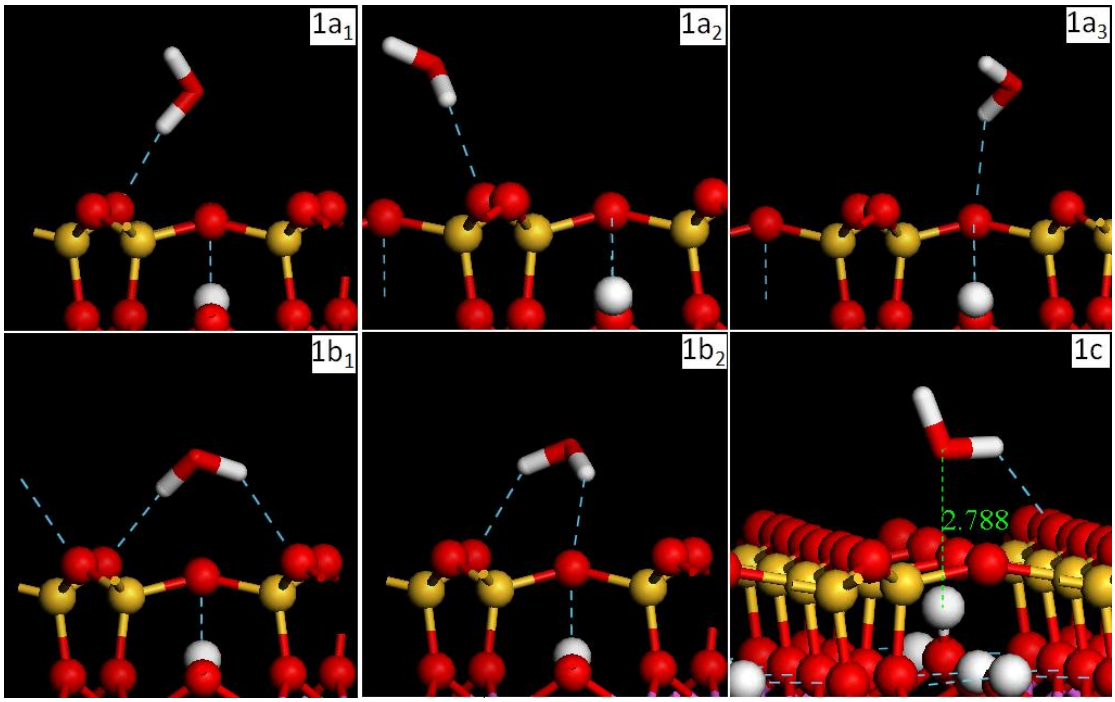

Figure 4.1: Representations of optimum structures of various binding motifs for one water molecule on the surface described in Table 4.2. Structures are extracted from PBE+D2 (**1a**$_{1\text{-}3}$, **1b**$_{1\text{-}2}$) and CLAYFF (**1c**) results, respectively.

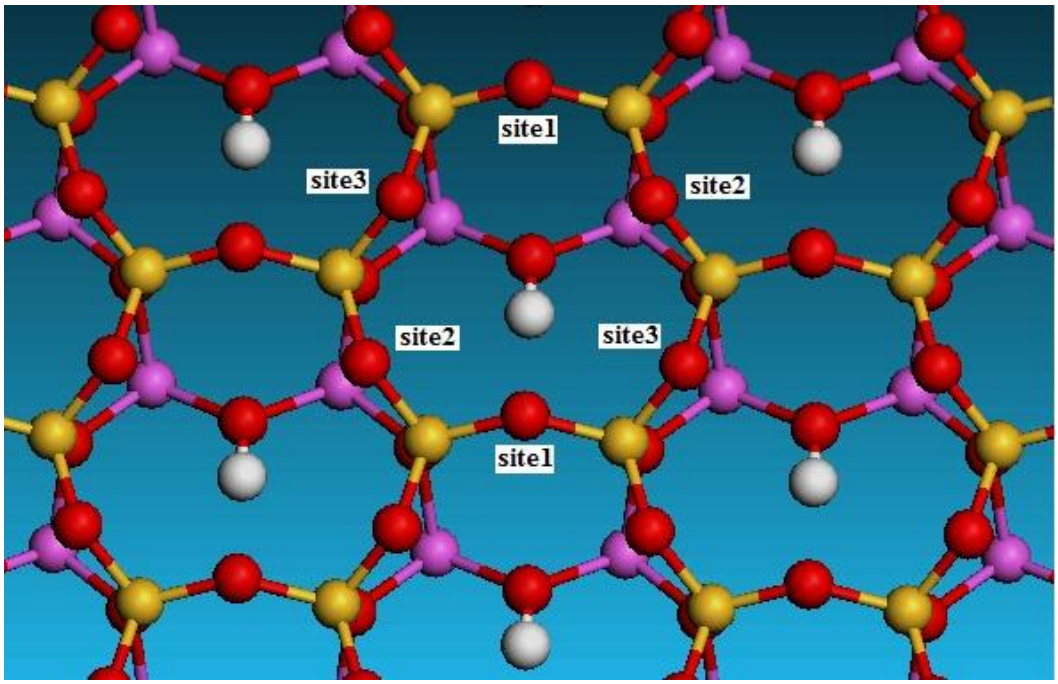

Figure 4.2: Definition of oxygen sites on the pyrophyllite surface.

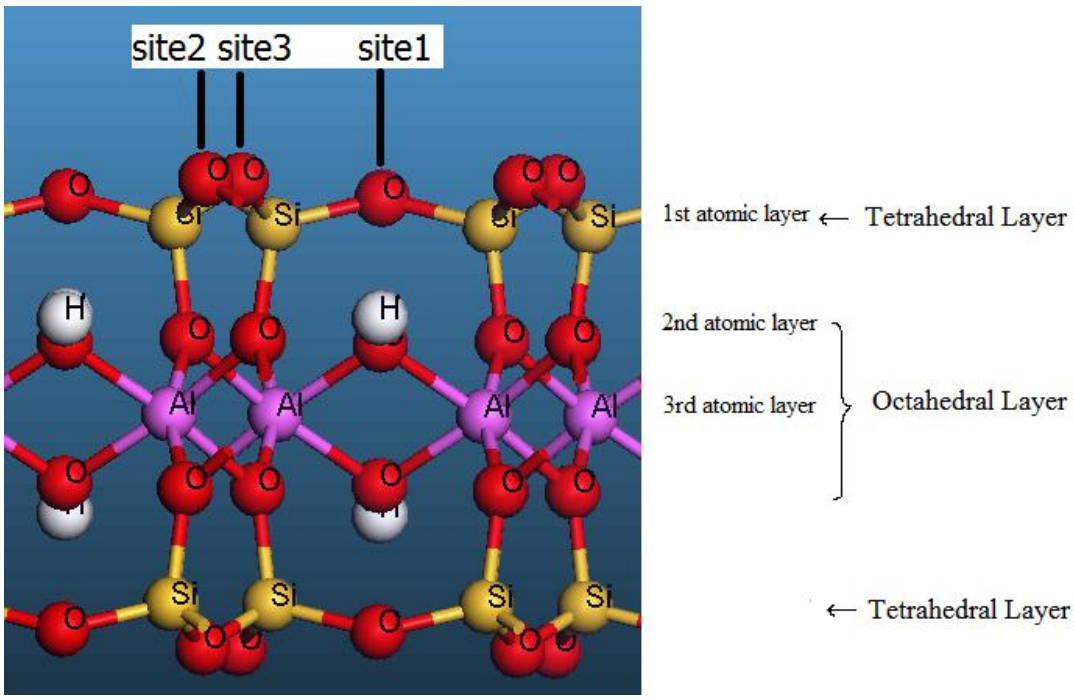

Figure 4.3: Side view of the pyrophyllite.

It is noted that the binding energies obtained from the DFT-D2 calculations are much larger in magnitude than those (-0.01 to -0.02 eV) from an early study,[175] which used a $2\times1\times1$ supercell with four water molecules on the surface, and employed the PBE functional without dispersion corrections. We have verified that a similar binding energy of -0.02 eV per water molecule is obtained when using the same model system as employed in Ref 176. This comparison validates our DFT-D2 calculations.

Three of the binding motifs found in the PBE+D2 calculations (**1a**$_1$, **1a**$_2$, and **1b**$_1$) are also identified in the CLAYFF calculations. However, the hydrogen bonds in the CLAYFF calculations are up to 0.35 Å shorter than those found in the PBE+D2 structures. This is indicative of a deficiency in CLAYFF. However, the most significant difference between the

PBE+D2 and CLAYFF characterization of a single water molecule on the surface is that the oxygen atom of water in the **1c** CLAYFF structure binds to the hydrogen atom of a hydroxyl group in the octahedral layer. This binding motif is not located as a minimum in the PBE+D2 optimizations. The coordination in **1c** requires the pyrophyllite hydroxyl group to rotate from its usual near parallel-to-surface orientation[142,198] to near perpendicular to the surface. The **1c** species is also found with the CLAYFF-M and CLAYFF-E calculations (not reported in Table 1), where again it is predicted to be comparable in stability to $\mathbf{1b_1}$. In contrast, in the CLAYFF-T calculations, **1c** ceases to be a local minimum and collapses to $\mathbf{1b_1}$. This may be a consequence of the TIP4P model used to describe water in CLAYFF-T, providing a more realistic description of the electrostatic potential of the water monomer.

4.3.2 Water dimer

Fig 4.4 depicts the three lowest energy structures of the water dimer on the pyrophyllite surface located in the PBE+D2 calculations, with the key geometrical parameters and binding energies being given in Table 3.3. These are $\mathbf{2a_1}$ and $\mathbf{2a_2}$, with the acceptor water making one hydrogen bond to the surface, and $\mathbf{2b_1}$ with the acceptor water interacting with the surface via two hydrogen bonds. There are some binding motifs closely related to $\mathbf{2b_1}$ arrangement that are about 0.1 eV less stable than $\mathbf{2b_1}$ (Table 4.4 and Fig 4.5). The PBE+D2 calculations predict $\mathbf{2b_1}$ to be most stable, followed by $\mathbf{2a_1}$ and $\mathbf{2a_2}$. For all three structures, the water-water hydrogen bond strength is nearly the same as that for the gas-phase dimer. Thus the interaction between water and the surface has little impact on the interaction between the two water molecules.

Two of the three minima, $\mathbf{2a_2}$ and $\mathbf{2b_1}$, found in the PBE+D2 calculations, were also found as minima in the CLAYFF calculations. CLAYFF and its variants give appreciably

smaller water-surface binding energies and stronger water-water interactions than found in the PBE+D2 calculations. The latter is a direct consequence of the water force fields used, which overestimate the strength of the hydrogen bond in the water dimer. All variants of CLAYFF give a third binding motif (**2c**) which, like **1c**, described above for the monomer, has a bond to a surface OH group. With CLAYFF and CLAYFF-E, **2c** is predicted to be of comparable stability to **2b$_1$**, whereas with CLAFF-T, it is found to be significantly less stable than **2b$_1$**.

Table 4.3 Key distances (Å) and energies (eV) for the binding of a water dimer on the pyrophyllite surface.

Method	Motif	O_{w1}-O_{w2}[a]	H_{w1}-O_{w2}	H_{w2}-O_b	Si-O_{w1}	O_w-H_o[b]	E_{int}[c]	E_{surf}[d]	Binding sites
PBE+D2	**2a$_1$**	2.82	1.84	2.04	3.09		-0.59	-0.34	2
	2a$_2$	2.86	1.88	2.39	3.06		-0.54	-0.30	3
	2b$_1$	2.79	1.81	1.99/2.26	2.95		-0.65	-0.42	2,3
CLAYFF	**2a$_2$**	2.72	1.70	1.81	3.08		-0.53	-0.24	3
	2b$_1$	2.74	1.72	2.00/2.30	3.16		-0.54	-0.25	2,3
	2c	2.73	1.73	1.89		2.57	-0.54	-0.26	3
CLAYFF-E	**2a$_2$**	2.74	1.72	1.85	3.02		-0.56	-0.23	3
	2b$_1$	2.72	1.70	1.98/2.25	3.16		-0.58	-0.26	2,3
	2c	2.71	1.71	1.80		2.68	-0.58	-0.28	3
CLAYFF-T	**2a$_2$**	2.75	1.77	1.83	3.10		-0.54	-0.24	3
	2b$_1$	2.74	1.76	2.03/2.14	3.20		-0.57	-0.27	2,3
	2c	2.74	1.80	1.84		2.73	-0.49	-0.22	3

[a] w1 and w2 refers to the hydrogen bond donor water molecule and hydrogen bond acceptor water molecule, respectively. [b] O_w-H_o denotes the hydrogen bond length between the oxygen (water) and hydrogen (hydroxyl group). [c] E_{int} denotes the net interaction energy. [d] E_{surf} denotes the interaction energy between the water dimer and the surface.

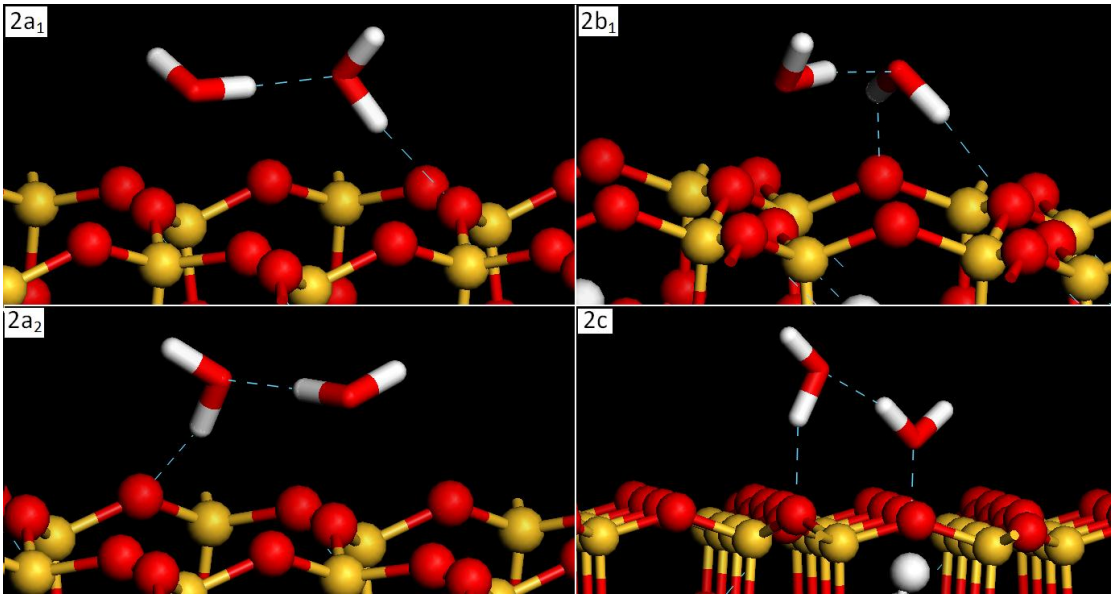

Figure 4.4: Representations of various binding motifs of the water dimer on the surface described from Table 4.3. Structures are extracted from PBE+D2 (**2a$_{1\text{-}2}$**, **2b$_1$**) and CLAYFF (**2c**) results, respectively.

Table 4.4 Key distances (Å) and energies (eV) of less stable binding motifs of the water dimer on the pyrophyllite surface, predicted by PBE+D2 calculations.

Motif	O_{w1}-O_{w2}[a]	H_{w1}-O_{w2}	H_{w2}-O_b	Si-O_{w1}	E_{int}[b]	E_{surf}[c]	Binding sites
2b$_2$	2.79	1.80	2.49/2.53	3.27	-0.60	-0.35	2,2
2b$_3$	2.79	1.81	2.35/2.56	3.18	-0.59	-0.36	3,3
2b$_4$	2.79	1.81	2.41/2.44	3.33	-0.57	-0.34	1,2
2b$_5$	2.86	1.88	2.16/2.48	3.06	-0.57	-0.33	1,3

[a] w1 and w2 refer to the hydrogen bond donor and acceptor molecules, respectively. [b] E_{int} denotes the net interaction energy. [c] E_{surf} denotes the interaction energy between the water dimer and the surface.

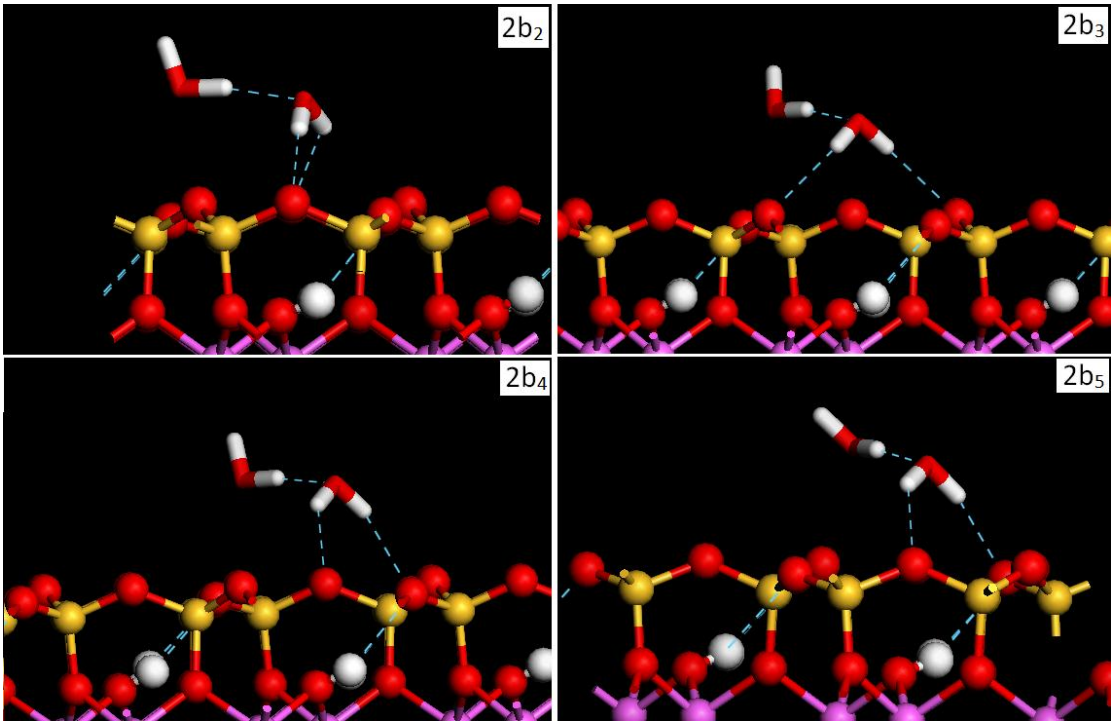

Figure 4.5: Structures of the water dimer on the pyrophyllite surface described in Table 4.4.

4.3.3 Water trimer

The low-energy forms of the water trimer on the pyrophyllite surface are shown in Fig 4.6. Although the global minimum of the gas-phase water trimer is cyclic, both cyclic and linear trimer structures are found as local minima on the pyrophyllite surface. The cyclic (**$3a_1$**) and linear (**$3b_1$**) forms of $(H_2O)_3$ found in the PBE+D2 calculations both donate two hydrogen bonds to the surface. The cyclic isomer is predicted to be more stable, although the chain isomer binds more strongly to the surface (Table 4.5). The stronger binding of the chain isomer to the surface could be due to its larger dipole moment.

The calculations using CLAYFF predict the cyclic (**$3a_1$**) configuration to be the most stable structure in agreement with the PBE-D2 calculations, but give a different binding

arrangement (**3b$_2$**) for the chain isomer than found in the PBE+D2 calculations. In the **3b$_2$** structure, the water trimer donates one hydrogen bond to the surface and accepts one hydrogen bond from an OH group in the octahedral sheet. All variants of CLAYFF predict that the binding motif with cyclic trimer is more stable than the chain-like structure.

Table 4.5 Key distances (Å) and energies (eV) for the binding of a water trimer on the pyrophyllite surface.

Method	Motif	H_w-O_b[a]	O_w-H_o	E_{int}	E_{surf}	Binding site(s)
PBE+D2	**3a$_1$**	2.11/2.17		-1.16	-0.36	3,3
	3b$_1$	2.04/2.59		-1.02	-0.46	1,3
CLAYFF	**3a$_1$**	1.90/1.99		-1.05	-0.28	3,3
	3b$_2$	1.80	2.43	-1.02	-0.37	2
CLAYFF-M	**3a$_1$**	1.89/1.90		-1.06	-0.30	3,3
	3b$_2$	1.95	2.66	-0.99	-0.35	2
CLAYFF-E	**3a$_1$**	1.84/1.94		-1.13	-0.29	3,3
	3b$_2$	1.78	2.38	-1.10	-0.40	2
CLAYFF-T	**3a$_1$**	1.85/1.93		-1.14	-0.35	3,3
	3b$_2$	1.88	2.67	-1.04	-0.41	2

[a] H_w-O_b denotes the hydrogen bonds lengths between water and the surface. In the case of multiple hydrogen bonds to O_b sites on the surface, all bond lengths are reported.

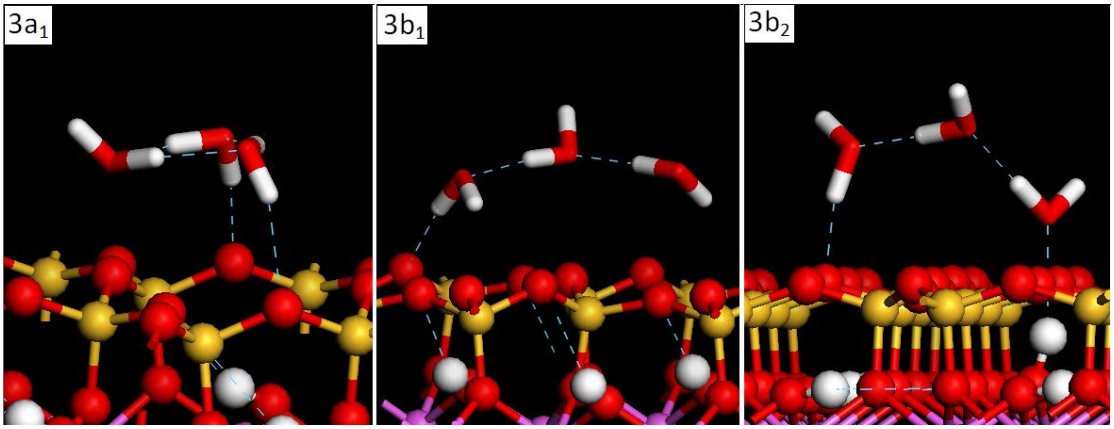

Figure 4.6: Representations of various binding motifs of the water trimer on the pyrophyllite surface described in Table 4.5, extracted from PBE+D2 (**3a$_1$** and **3b$_1$**) and CLAYFF (**3b$_2$**) results, respectively.

4.3.4 Water tetramer

The PBE+D2 calculations predict two low-energy structures (**4a$_1$** and **4a$_2$**) of $(H_2O)_4$ on the pyrophyllite surface. Both of these species retain the cyclic structure of the gas-phase isomer and bond to the surface *via* two hydrogen bonds involving OH groups associated with two water molecules (Fig. 4.7). **4a$_1$** is H-bonded to site 1 and site 3 (Table 4.6), and **4a$_2$** (Table 4.7 and Fig 4.8) lying only 0.02 eV above $4a_1$, is H-bonded to site 2 and site 3, and. On the other hand, CLAYFF and its variants predict a rich set of binding motifs, including cyclic tetramers (**4a$_2$**, **4a$_3$**), chain tetramers (**4b$_1$**, **4b$_2$**), and "Y"-shape tetramers (**4c$_1$**, **4c$_2$**). All variants of CLAYFF fail to locate the (**4a$_1$**) binding motif, and predict **4a$_2$** to be the most stable structure. The **4a$_3$** structure incorporates a cyclic water tetramer with DD and AA water monomers. This tetramer is bonded to the surface by donating an H-bond to site 3 and accepting a hydrogen bond from a sub-surface hydroxyl group. The Y-shaped tetramer structures are comprised of a cyclic trimer with a dangling monomer. The two structures with chain-like water tetramers accept an H-bond from a sub-surface hydroxyl group.

Table 4.6 Key distances (Å) and energies (eV) for the binding of a water tetramer on the pyrophyllite surface.

Method	Motif	N_{hb}^{ww} [a]	N_{hb}^{ws} [b]	H_w-O_b	O_w-H_o	E_{int}	E_{surf}	Binding sites
PBE+D2	**4a$_1$**	4	2	2.21/2.32		-1.86	-0.42	1,3
CLAYFF	**4a$_2$**	4	2	1.95/2.35		-1.66	-0.30	2,3
	4a$_3$	4	2	1.78	2.49	-1.42	-0.51	3
	4b$_1$	3	2	1.82/1.93	2.36	-1.49	-0.51	2,3
	4c$_1$	4	2	2.00/2.28		-1.44	-0.37	3,3
CLAYFF-M	**4a$_2$**	4	2	1.95/2.48		-1.67	-0.31	2,3
	4a$_3$	4	1	1.85	2.59	-1.40	-0.49	3
	4b$_2$	3	3	1.83/1.87/2.45	2.52	-1.47	-0.48	2,2,3
	4c$_2$	4	2	1.96/2.39		-1.44	-0.38	2,3
CLAYFF-E	**4a$_2$**	4	2	1.97/2.42		-1.80	-0.31	2,3
	4a$_3$	4	1	1.80	2.31	-1.53	-0.54	3
	4b$_2$	3	3	1.85/1.91/2.37	2.24	-1.61	-0.53	2,2,3
	4c$_1$	4	2	2.01/2.40		-1.55	-0.37	3,3
CLAYFF-T	**4a$_2$**	4	2	2.00/2.05		-1.65	-0.33	2,3
	4a$_3$	4	1	1.88	2.530	-1.44	-0.50	3
	4b$_2$	3	3	1.84/1.88/2.42	2.330	-1.50	-0.52	2,2,3
	4c$_1$	4	2	1.97/2.24		-1.45	-0.40	3,3

[a] N_{hb}^{ww} is the number of water-water H-bonds. [b] N_{hb}^{ws} is the number of water-surface H-bonds.

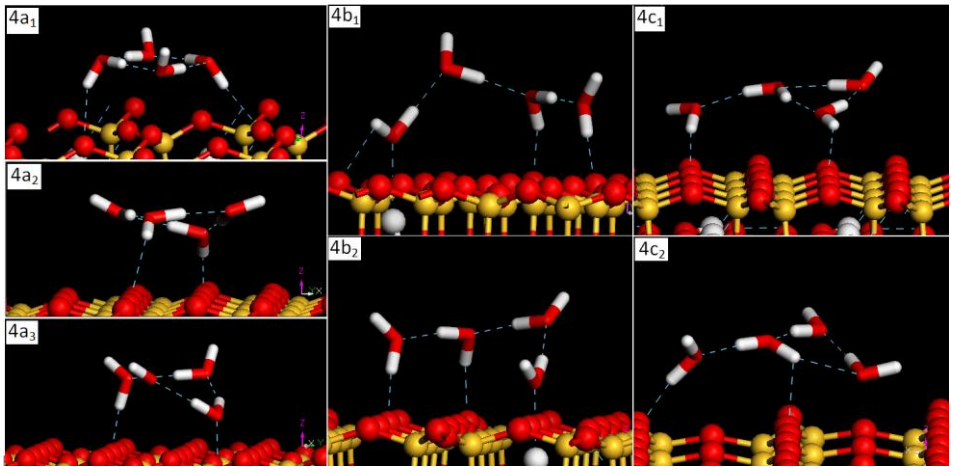

Figure 4.7: Representations of various binding motifs for the water tetramer on the surface described in Table 4.6, extracted from PBE+D2 (**4a$_1$**) and CLAYFF (**4a$_{2-3}$, 4b$_{1-2}$, 4c$_{1-2}$**) results, respectively.

Table 4.7 Key distances (Å) and energies (eV) of a less stable binding motif of the water tetramer on the pyrophyllite surface.

Motif	H_w-O_b	E_{int}	E_{surf}	Binding sites
$4a_2$	2.10/2.37	-1.84	-0.41	2,3

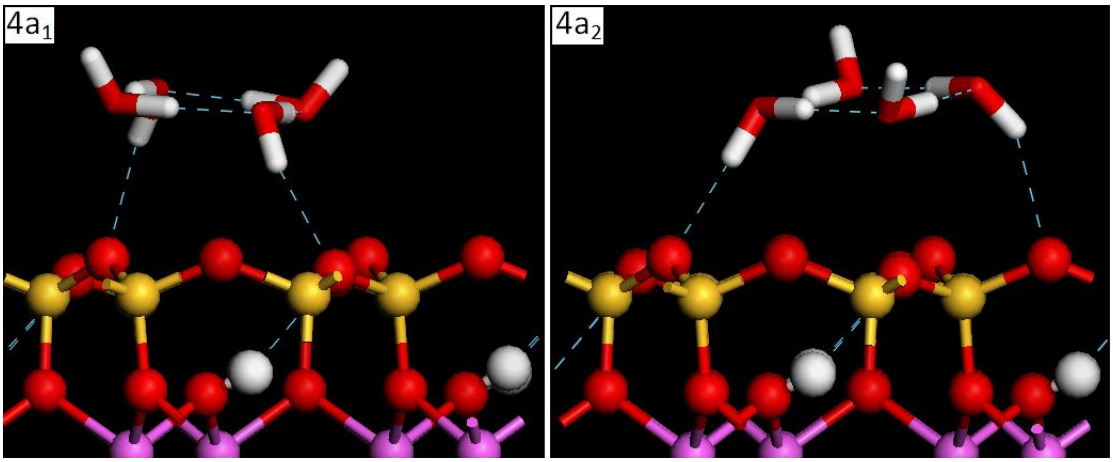

Figure 4.8: $4a_2$ binding motif of the water tetramer on the pyrophyllite surface described in Table 4.7. $4a_1$ from the main text is included for comparison.

4.3.5 Water pentamer

The key structures of the water pentamer on the pyrophyllite surface are depicted in Fig 4.9, with the geometrical parameters and binding energies being given in Table 4.8. The PBE+D2 calculations predict that the most stable arrangement of five water molecules on the pyrophyllite surface (**$5a_1$**) retains the five-member ring found in the gas-phase pentamer[199,200] and donates three hydrogen bonds to the surface. This binding motif has also one less stable (0.03 eV) isomer (Table 4.9 and Fig 4.10) with different binding sites. The PBE+D2 calculations also predict a second isomer (**$5b_1$**) consisting of a four-member ring with a dangling water molecule, 0.14 eV less stable than **$5a_1$** even though it binds 0.12 eV more strongly to the surface than **$5a_1$**. While

this isomeric form of $(H_2O)_5$ is highly unstable in the gas phase, it is more relevant on the surface due to its donation of three hydrogen bonds to basal oxygen atoms. The various CLAYFF variants also locate the **5a$_1$** structure as well as a less stable binding motif (**5b$_2$**) involving a cyclic tetramer and a dangling water molecule, differing from **5b$_1$** by how it is bonded to the surface.

Table 4.8 Key distances (Å) and energies (eV) for the binding of a water pentamer on the pyrophyllite surface.

Method	Motif	N_{hb}^{ww}	N_{hb}^{ws}	H_w-O_b	E_{int}	E_{surf}	Binding Site(s)
PBE+D2	**5a$_1$**	5	3	2.11/2.19/2.48	-2.36	-0.47	2,3,3
	5b$_1$	5	3	2.13/2.30/2.36	-2.22	-0.59	1,2,3
CLAYFF	**5a$_1$**	5	3	1.86/1.98/1.99	-2.15	-0.38	2,3,3
	5b$_2$	5	2	1.84/1.96	-2.06	-0.44	2,3
CLAYFF-E	**5a$_1$**	5	3	1.85/1.87/1.99	-2.34	-0.41	2,3,3
	5b$_2$	5	2	1.84/1.92	-2.24	-0.46	2,3
CLAYFF-T	**5a$_1$**	5	3	1.86/2.01/2.05	-2.16	-0.44	2,3,3
	5b$_2$	5	2	1.90/1.91	-2.07	-0.48	2,3

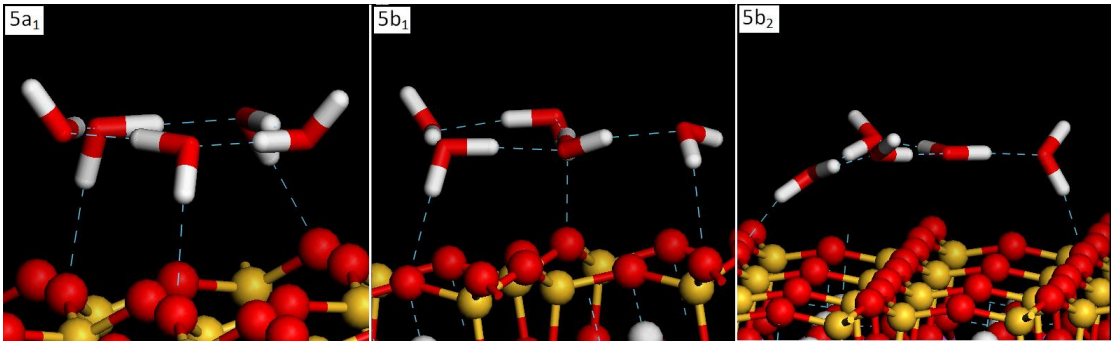

Figure 4.9: Representations of various binding motifs for the water pentamer on the surface described in Table 4.8. Structures are extracted from PBE+D2 ($5a_1$ and $5b_1$) and CLAYFF ($5b_2$) results, respectively.

Table 4.9 Key distances (Å) and energies (eV) of less stable binding motifs of the water pentamer on the pyrophyllite surface, predicted by PBE+D2 calculations.

Motif	H_w-O_b	E_{int}	E_{surf}	Binding sites
5a$_2$	2.30/2.35/2.53	-2.33	-0.45	3,3,3
5a$_3$	2.37/2.51/2.54	-2.28	-0.42	1,3,3
5a$_4$	2.04/2.47	-2.24	-0.44	2,2
5b$_3$	2.18/2.36/2.45	-2.16	-0.54	1,3,3

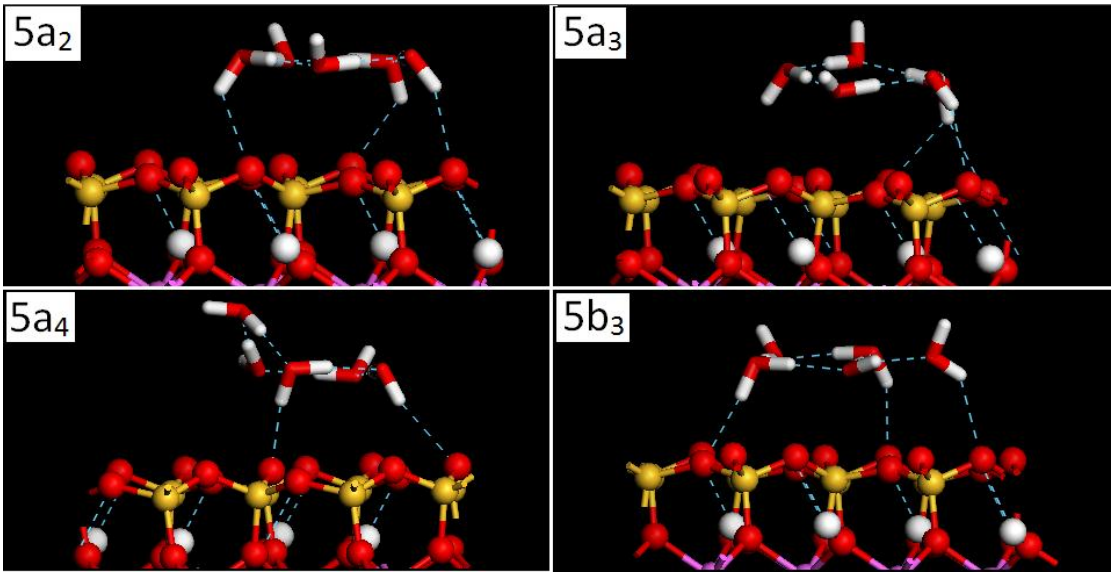

Figure 4.10: Structures of the water pentamer on the pyrophyllite surface described in Table 4.9.

4.3.6 Water hexamer

The low energy forms of $(H_2O)_6$ on the pyrophyllite surface are depicted in Fig 4.11, with the binding energies and geometrical parameters being summarized in Table 4.10. The gas-phase water hexamer possesses low energy ring, book, cage, prism and bag isomers.[201-206] At the complete basis set limit CCSD(T) level of theory, the cage and prism isomers are nearly isoenergetic, and 1-2 kcal/mol more stable than the book and ring isomers.[206] For the gas-phase hexamer, the PBE+D2 calculations are consistent with the CCSD(T) results in the order of these four isomers (Fig 4.13). However, on the pyrophyllite surface, the book isomer (**6a$_1$**) is predicted at the PBE+D2 level of theory to be most favorable, followed by the ring isomer (**6b$_1$**). These two nearly isoenergetic species are shown in Fig 4.8. In addition, the cage and prism isomers (Table 4.11 and Fig 4.12) are calculated to be 0.03-0.06 eV less stable than the book isomer on the pyrophyllite surface. Most interestingly, the PBE+D2 calculations also locate a structure (**6c$_1$**) consisting of a cyclic water pentamer with a dangling water molecule on the surface. This structure is found to be 0.13 eV less stable than the global minimum (**6a$_1$**).

The various CLAYFF variants predict a similar ordering of the different water hexamers on the surface as found in the PBE-D2 calculations. However, the binding sites on the surface found in the CLAYFF optimizations differ from those obtained in the DFT-D2 calculations. Most noticeably, the ring isomer found in the CLAYFF calculations (**6b$_2$**) does not retain the near-flat arrangement of oxygen atoms, but instead, distorts to form a chair-like structure. The CLAYFF calculations predict a second book structure (**6a$_2$**) to be only 0.08 eV more stable than **6b$_2$**, and a structure with cyclic pentamer plus dangling monomer (**6c$_2$**) about 0.05 eV less stable than **6b$_2$**.

Table 4.10 Key distances (Å) and energies (eV) for the binding of a water hexamer on the pyrophyllite surface.

Method	Motif	N_{hb}^{ww}	N_{hb}^{ws}	H_w-O_b	E_{int}	E_{surf}	Binding Site(s)
PBE+D2	**$6a_1$**	7	2	2.09/2.33	-2.86	-0.49	3,3
	$6b_1$	6	3	2.10/2.24/2.24	-2.84	-0.54	1,2,3
	$6c_1$	6	3	1.96/2.451/2.46	-2.73	-0.62	2,2,2
CLAYFF	**$6a_2$**	7	3	1.86/1.93/1.99	-2.67	-0.48	2,2,3
	$6b_2$	7	3	1.80/1.85/1.99	-2.59	-0.42	2,2,3
	$6c_2$	6	2	1.78/1.98	-2.54	-0.50	2,3
CLAYFF-E	**$6a_2$**	7	3	1.81/1.93/2.03	-2.89	-0.49	2,2,3
	$6b_2$	7	3	1.80/1.86/1.97	-2.80	-0.44	2,2,3
	$6c_2$	6	2	1.78/1.90	-2.75	-0.51	2,3
CLAYFF-T	**$6a_2$**	7	3	1.82/1.96/2.04	-2.67	-0.50	2,2,3
	$6b_2$	7	3	1.84/1.89/1.96	-2.54	-0.44	2,2,3
	$6c_2$	6	2	1.88/1.91	-2.49	-0.50	2,3

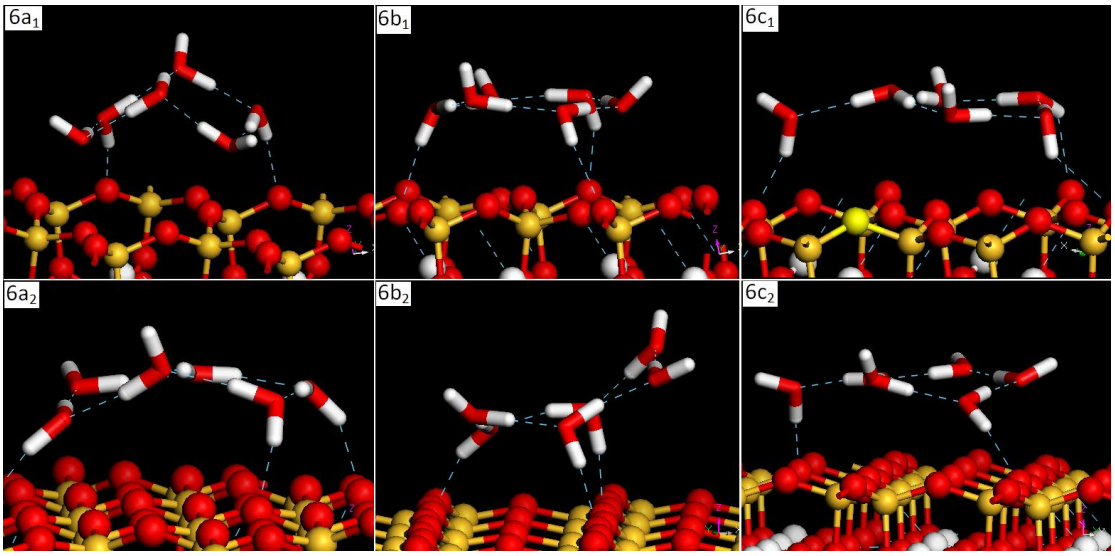

Figure 4.11: Representations of various binding motifs for the water hexamer on the surface described in Table 4.10. Structures are extracted from PBE+D2 ($6a_1$, $6b_1$ and $6c_1$) and CLAYFF ($6a_2$, $6b_2$ and $6c_2$) results, respectively.

Table 4.11 Key distances (Å) and energies (eV) of less stable binding motifs of the water hexamer on the pyrophyllite surface, predicted by PBE+D2 calculations.

Motif	H_w-O_b	E_{int}	E_{surf}	Binding sites
prism	2.20/2.44/2.46	-2.82	-0.45	3,3,3
cage	2.42/2.42	-2.78	-0.40	2,2
book(2)	2.10/2.22/2.30	-2.80	-0.54	2,2,3
book(3)	2.11/2.12	-2.78	-0.42	1,3
book(4)	2.06/2.23	-2.73	-0.38	3,3
ring(2)	2.23/2.40	-2.69	-0.50	1,2

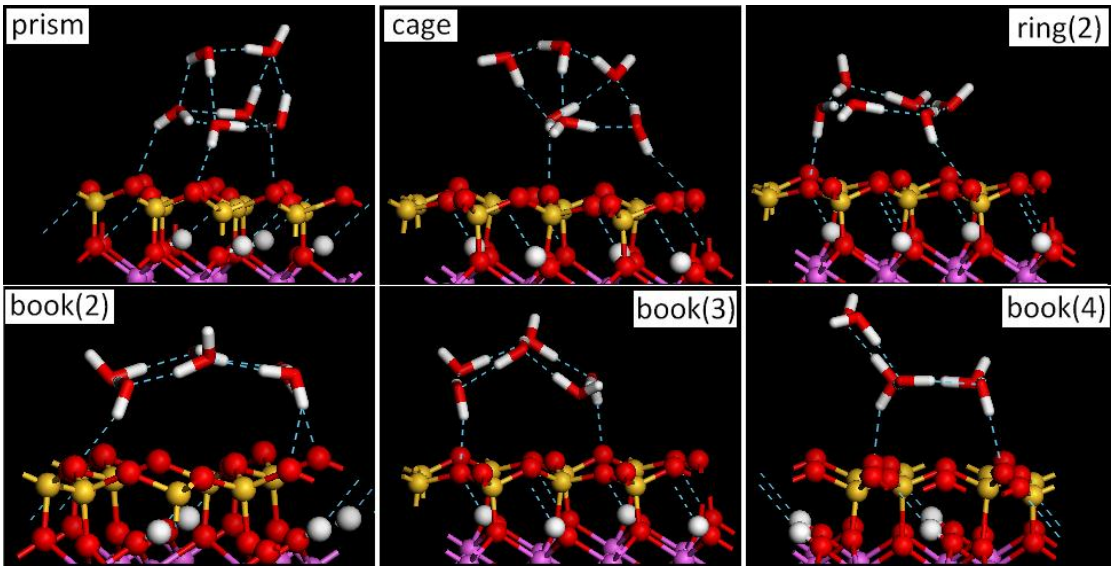

Figure 4.12: Structures of the water hexamer on the pyrophyllite surface described in Table 4.11.

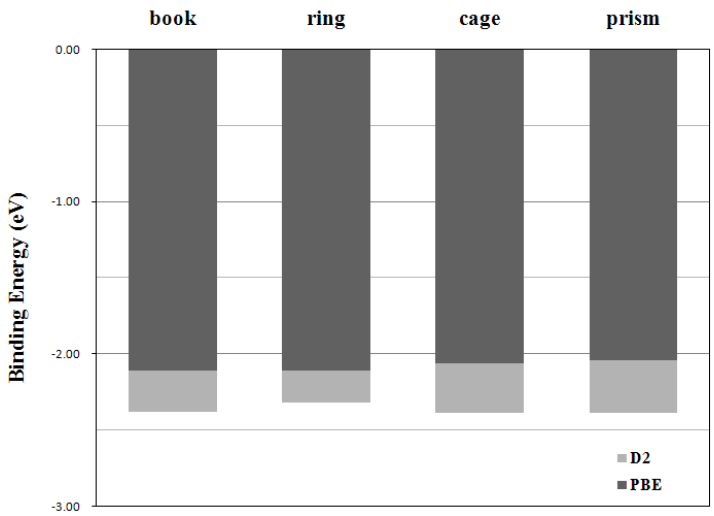

Figure 4.13: Binding energies of four gas phase water hexamer isomers. The geometries were optimized at the PBE+D2 level using PAW potential and plane wave basis sets. The dark and light grey regions represent, respectively, the non-dispersion and dispersion contributions to the PBE+D2 binding energies. The dispersion-corrected binding energies agree with complete basis set limit CCSD(T) results in terms of the ordering of the isomers.

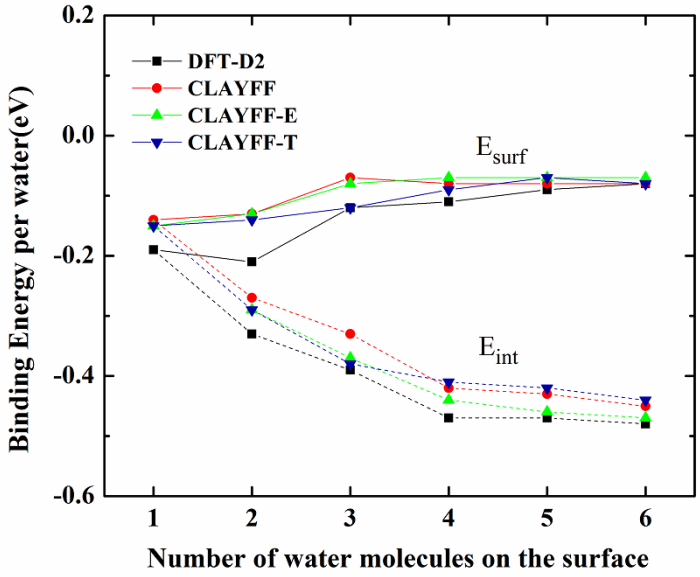

Figure 4.14: Trends of E_{int} (dash) and E_{surf} (solid) with the number of water molecules loading on the surface from PBE+D2 calculations and CLAYFF-based calculations, respectively.

The binding energies of the lowest energy structures of the $(H_2O)_n$ (n = 1-6) species on the pyrophyllite surface as determined by PBE+D2 calculations are reported in Fig 4.14. The strength of water-surface interaction per water molecule grows slightly in going from n = 1 to 2, and then decreases upon further increase in the number of water molecules. This primarily reflects the fact that, with the exception of the pentamer, the water clusters (n = 2-6) bind to the surface via two hydrogen bonds. (The pentamer binds via three hydrogen bonds.) On the other hand, the net stability of the cluster on the surface grows monotonically with the number of monomers. This is consistent with the growing stability of the isolated water clusters with increasing cluster size.

4.4 CONCLUSION

In summary, this study provides a detailed description of the energies and structures of small water clusters on the pyrophyllite surface. As expected, the inclusion of dispersion interactions plays an important role in the water-surface interactions. The interaction energy for a water monomer on the surface varies from -0.10 to -0.19 eV depending on the binding site and binding orientation. These binding energies are roughly comparable to the recently estimated energy (~ -0.15 eV)[179] for the binding of a water molecule to the graphene surface, which is known to be hydrophobic. Further loading the surface with more water molecules leads to formation of water clusters, hydrogen-bonded to basal oxygen atoms. The structures of the clusters correspond closely to these of the corresponding gas phase species. These results are consistent with the stronger water-water interactions than the water-surface interactions. In a qualitative sense, the

CLAYFF calculations reproduce the trend of binding energies of water molecules on the surface found in the PBE-D2 calculations, although CLAYFF gives much shorter hydrogen bond lengths and smaller values of the binding energies. However, the force field-based calculations predict several binding motifs (e.g., **1c**, **2c**, **3b$_2$**, **4b$_1$**) involving a hydrogen bond from a subsurface OH group to a water monomer which are not located in the PBE+D2 optimizations. Upon switching from the SPC to TIP4P water model, this local minimum is eliminated in the single water case, but persists for larger water clusters. The problem also persists when using a Morse potential to describe the O-H stretch of the hydroxyl groups. It is likely that the appearance of these structures is a consequence of the fact that the hydroxyl group is not restrained in the force field via bonded terms with metal atoms. It is hoped that the present results will motivate the development of refined force field for describing water-clay interactions.

4.5 ACKNOWLEDGEMENT

This chapter is adapted from a manuscript in press as Zhang, G.; Al-Saidi, W. A.; Myshakin, E. M.; Jordan, K. "*Dispersion-corrected Density Functional Theory and Classical Force Field Calculations of Water Loading on a Pyrophyllite (001) Surface*". This work was performed in support of the National Energy Technology Laboratory's ongoing research in Subtask 4000.4.641.251.002.255 under the RES contract RES0004000.

5.0 CONCLUSION AND OUTLOOK

In summary, we demonstrate our computational study on methane hydrate and water-clay systems, respectively.

In the study of methane hydrate, we found that popular non-polarizable models (SPC/E and TIP4P family) need improvements to provide better descriptions of structure and thermal properties of methane hydrate. First is the nuclear quantum effect. The non-linear effect of lattice constants with respect to the temperature is not well described by non-polarizable (and polarizable as well) water models. This is the indicative of other factor at play, which is believed to be nuclear quantum effect of water. The overestimation of thermal conductivity also suggests the deficiency of the lack of nuclear quantum effects. As eqn (3-3) shows, thermal conductivity is proportional to specific heat capacity. The calculated specific heat capacity using the SPC/E, TIP4P/2005 and TIP4P/Ice water models are around 30% larger than the experimental measured value, in line with the conclusion from a previous study. And the deviation is attributed to nuclear quantum effects.[114] Second is polarizability of water. The power spectra results show that non-polarizable water models are not as good as polarizable water models in the description of water lattice vibration. This may also cause the overestimation of thermal conductivity. Last, but not least, is the balance. It is not uncommon for an empirical water model to have good performance on some properties of water while poor performance on others. This is because that a specific water model is always parameterized in favor of limited properties while water

actually has too many peculiar characters.[58] It is hoped that a non-polarizable water model is optimized for gas hydrates to better describe their properties. We also found that proton disorder has a subtle yet unknown effect on thermal conductivity of methane hydrate. This is in line with the suggestion from a previous experiment study.[105] Recently, proton-disorder is found to also play a non-trivial role in determining the dielectric constants of water and ice.[207] Thus, it is meaningful to take the proton disorder of water lattice into account for full understanding of the transport properties (e.g. thermal conductivity and dielectric constant) of ice as well as gas hydrates. Since phonon scattering is responsible for thermal conductivity of hydrates and ice, and lattice dynamics can provide abundant phonon information,[123] we could invoke lattice dynamics simulations to evaluate the nuclear quantum effect and proton-disorder effect on phonon scattering.

In the study of water-clay systems, we investigate the loading of small water clusters on the surface using DFT-D2 calculation as well as molecular simulation. The hydrophobicity of the pyrophyllite surface is interpreted as the dominance of water-water interaction over water-surface interaction. This point of view, though in agreement with the conclusion from previous DFT study, is more comprehensive. Moreover, the results demonstrate the importance of dispersion correction for the DFT calculation of weakly bound interaction between water molecules and pyrophyllite surface. It is expected that dispersion interaction is also significant for the absorbance of water and other species such as ammonia and hydrocarbons on the MMTs surface. The comparison between DFT-D2 and CLAYFF results disclose the deficiency of the classical force field on the description of water-clay interface. It is thus necessary to refine the force field parameters to better model on the interfacial interaction, in order to utilize it for the study of the growth of methane hydrate in a confined environment formed by clay minerals.

BIBLIOGRAPHY

(1) Sloan, E. D.; Koh, C. A. *Clathrate hydrates of natural gases*; 3rd ed.; CRC Press: Boca Raton, FL, 2008.

(2) Sloan, E. D. *Nature* **2003**, *426*, 353.

(3) Lienhard, J. H. *A heat transfer textbook*; 3rd ed.; Phlogiston Press: Cambridge, Massachusetts, 2008.

(4) English, N. J.; Tse, J. S. *Energies* **2010**, *3*, 1934.

(5) Gatti, C.; Bertini, L.; Blake, N. P.; Iversen, B. B. *Chem. Eur. J.* **2003**, *9*, 4556.

(6) Seo, Y.-j.; Seol, J.; Yeon, S.-H.; Koh, D.-Y.; Cha, M.; Kang, S.-P.; Seo, Y.-T.; Bahk, J.-j.; Lee, J.; Lee, H. *J. Chem. Eng. Data* **2009**, *54*, 1284.

(7) Guggenheim, S.; van Groos, A. F. K. *Geology* **2003**, *31*, 653.

(8) Kawasaki, T.; Hailong, L.; Ripmeester, J.; Moudrakovski, I.; Zeng, H.; Lee, J.; Fujii, T.; Nakamizu, M. *AGU Fall Meeting Abstracts* **2006**, OS33B1696.

(9) van Groos, A. F. K.; Guggenheim, S. *Am. Mineral.* **2009**, *94*, 372.

(10) Douillard, J.-M. In *Encyclopedia of surface and colloid science*; Hubbard, A. T., Ed.; Marcel Dekker: New York, 2002; Vol. 1, p 5601.

(11) Giese, R.; Oss, C. *Colloid and surface properties of clays and related minerals*; Marcel Dekker, Inc., 2002.

(12) Murray, H. H. *Appl. Clay Sci.* **2000**, *17*, 207.

(13) Geatches, D. L.; Clark, S. J.; Greenwell, H. C. *J. Phys. Chem. A* **2010**, *114*, 3569.

(14) Greathouse, J. A.; Cygan, R. T. *Environ. Sci. Technol.* **2006**, *40*, 3865.

(15) Chilingarian, G. V.; Vorabutr, P. *Drilling and Drilling Fluids*, 1983.

(16) Tunega, D.; Gerzabek, M. H.; Haberhauer, G.; Lischka, H. *Eur J Soil Sci* **2007**, *58*, 680.

(17) Sposito, G.; Skipper, N. T.; Sutton, R.; Park, S. H.; Soper, A. K.; Greathouse, J. A. *Proc. Natl. Acad. Sci. U. S. A.* **1999**, *96*, 3358.

(18) Romanov, V. N.; Ackman, T. E.; Soong, Y.; Kleinman, R. L. *Environ. Sci. Technol.* **2009**, *43*, 561.

(19) Bernal, J. D.; Fowler, R. H. *J. Chem. Phys.* **1933**, *1*, 515.

(20) Rahman, A.; Stillinger, F. H. *J. Chem. Phys.* **1972**, *57*, 4009.

(21) Rick, S. W. *J. Chem. Phys.* **2005**, *122*, 094504.

(22) Rick, S. W.; Freeman, D. L. *J. Chem. Phys.* **2010**, *132*, 054509.

(23) Tipler, P. A.; Mosca, G.; Alumni and Friends Memorial Book Fund. *Physics for scientists and engineers*; 6th ed.; W.H. Freeman: New York, NY, 2008.

(24) Cverna, F.; ASM International. Materials Properties Database Committee. *ASM ready reference. Thermal properties of metals*; ASM International: Materials Park, Ohio, 2002.

(25) Allen, M. P.; Tildesley, D. J. *Computer simulation of liquids*; Oxford University Press: New York, 1989.

(26) Lewerenz, M. In *Quantum Simulations of Complex Many-Body Systems: From Theory to Algorithms*; Grotendorst, J., Marx, D., Muramatsu, A., Eds.; John von Neumann Institute for Computing: Jülich, Germany, 2002, p 1.

(27) Sutmann, G. In *Quantum Simulations of Complex Many-Body Systems: From Theory to Algorithms*; Grotendorst, J., Marx, D., Muramatsu, A., Eds.; John von Neumann Institute for Computing: Jülich, Germany, 2002, p 221.

(28) Tuckerman, M. E. In *Quantum Simulations of Complex Many-Body Systems: From Theory to Algorithms*; Grotendorst, J., Marx, D., Muramatsu, A., Eds.; John von Neumann Institute for Computing: Jülich, Germany, 2002, p 299.

(29) Marx, D.; Hutter, J. In *Modern Methods and Algorithms of Quantum Chemistry*; Grotendorst, J., Ed.; John von Neumann Institute for Computing: Jülich, Germany, 2000, p 301.

(30) Berendsen, H. J. C.; Vanderspoel, D.; Vandrunen, R. *Comput. Phys. Commun.* **1995**, *91*, 43.

(31) Smith, W.; Forester, T. R. *J. Mol. Graph.* **1996**, *14*, 136.

(32) Gibbon, P.; Sutmann, G. In *Quantum Simulations of Complex Many-Body Systems: From Theory to Algorithms*; Grotendorst, J., Marx, D., Muramatsu, A., Eds.; John von Neumann Institute for Computing: Jülich, Germany, 2002, p 467.

(33) Yeh, I. C.; Wallqvist, A. *J. Chem. Phys.* **2011**, *134*, 055109.

(34) Essmann, U.; Perera, L.; Berkowitz, M. L.; Darden, T.; Lee, H.; Pedersen, L. G. *J. Chem. Phys.* **1995**, *103*, 8577.

(35) Onsager, L. *J. Am. Chem. Soc.* **1936**, *58*, 1486.

(36) Barker, J. A.; Watts, R. O. *Mol. Phys.* **1973**, *26*, 789

(37) Smith, W.; Forester, T. R.; Todorov, I. T. *THE DL_POLY_2 USER MANUAL*; STFC Daresbury Laboratory: Cheshire, UK, 2008.

(38) Perera, L.; Berkowitz, M. L. *J. Chem. Phys.* **1991**, *95*, 1954.

(39) Illingworth, C. J.; Domene, C. *P R Soc A* **2009**, *465*, 1701.

(40) Warshel, A.; Kato, M.; Pisliakov, A. V. *J. Chem. Theory Comput.* **2007**, *3*, 2034.

(41) Yu, H. B.; van Gunsteren, W. F. *Comput. Phys. Commun.* **2005**, *172*, 69.

(42) Geerke, D. P.; van Gunsteren, W. F. *J. Phys. Chem. B* **2007**, *111*, 6425.

(43) Kumar, R.; Wang, F. F.; Jenness, G. R.; Jordan, K. D. *J. Chem. Phys.* **2010**, *132*, 014309.

(44) Kumar, R.; Wang, F. F.; Jenness, G. R.; Jordan, K. D. *J. Chem. Phys.* **2010**, *132*, 014309.

(45) Abascal, J. L. F.; Vega, C. *Phys. Rev. Lett.* **2007**, *98*, 237801.

(46) Potter, D. *Computational physics*; J. Wiley: London, New York,, 1973.

(47) Swope, W. C.; Andersen, H. C.; Berens, P. H.; Wilson, K. R. *J. Chem. Phys.* **1982**, *76*, 637.

(48) Evans, D. J.; Morriss, O. P. *Computer Physics Reports* **1984**, *1*, 297.

(49) Berendsen, H. J. C.; Postma, J. P. M.; van Gunsteren, W. F.; DiNola, A.; Haak, J. R. *J. Chem. Phys.* **1984**, *81*, 3684.

(50) Hoover, W. G. *Phys. Rev. A* **1985**, *31*, 1695.

(51) Andersen, H. C. *J. Chem. Phys.* **1980**, *72*, 2384.

(52) Guillot, B.; Guissani, Y. *J. Chem. Phys.* **1993**, *99*, 8075.

(53) Paschek, D. *J. Chem. Phys.* **2004**, *120*, 6674.

(54) Martin, M. G.; Siepmann, J. I. *J. Phys. Chem. B* **1998**, *102*, 2569.

(55) Jorgensen, W. L.; Madura, J. D.; Swenson, C. J. *J. Am. Chem. Soc.* **1984**, *106*, 6638.

(56) Kaminski, G.; Duffy, E. M.; Matsui, T.; Jorgensen, W. L. *J. Phys. Chem.* **1994**, *98*, 13077.

(57) Tse, J. S.; Klein, M. L.; McDonald, I. R. *J. Chem. Phys.* **1984**, *81*, 6146.

(58) Guillot, B. *J. Mol. Liq.* **2002**, *101*, 219.

(59) Jorgensen, W. L.; Chandrasekhar, J.; Madura, J. D.; Impey, R. W.; Klein, M. L. *J. Chem. Phys.* **1983**, *79*, 926.

(60) Berendsen, H. J. C.; Grigera, J. R.; Straatsma, T. P. *J. Phys. Chem.* **1987**, *91*, 6269.

(61) Abascal, J. L. F.; Vega, C. *J. Chem. Phys.* **2005**, *123*, 234505.

(62) Abascal, J. L. F.; Sanz, E.; Fernandez, R. G.; Vega, C. *J. Chem. Phys.* **2005**, *122*, 234511.

(63) Vega, C.; Abascal, J. L. F.; Conde, M. M.; Aragones, J. L. *Faraday Discuss.* **2009**, *141*, 251.

(64) Conde, M. M.; Vega, C. *J. Chem. Phys.* **2010**, *133*, 064507.

(65) Sun, R.; Duan, Z. H. *Geochim. Cosmochim. Acta* **2005**, *69*, 4411.

(66) Anderson, B. J.; Tester, J. W.; Borghi, G. P.; Trout, B. L. *J. Am. Chem. Soc.* **2005**, *127*, 17852.

(67) Jorgensen, W. L.; Maxwell, D. S.; Tirado-Rives, J. *J. Am. Chem. Soc.* **1996**, *118*, 11225.

(68) McMullan, R. K.; Jeffrey, G. A. *J. Chem. Phys.* **1965**, *42*, 2725.

(69) Myshakin, E. M.; Jiang, H.; Warzinski, R. P.; Jordan, K. D. *J. Phys. Chem. A* **2009**, *113*, 1913.

(70) Parrinello, M.; Rahman, A. *J. Appl. Phys.* **1981**, *52*, 7182.

(71) Nosé, S.; Klein, M. L. *Mol. Phys.* **1983**, *50*, 1055

(72) Jiang, H.; Jordan, K. D.; Taylor, C. E. *J. Phys. Chem. B* **2007**, *111*, 6486.

(73) English, N. J.; MacElroy, J. M. D. *J. Comput. Chem.* **2003**, *24*, 1569.

(74) Ren, P. Y.; Ponder, J. W. *J. Phys. Chem. B* **2003**, *107*, 5933.

(75) Yu, H. B.; van Gunsteren, W. F. *J. Chem. Phys.* **2004**, *121*, 9549.

(76) Gutt, C.; Asmussen, B.; Press, W.; Johnson, M. R.; Handa, Y. P.; Tse, J. S. *J. Chem. Phys.* **2000**, *113*, 4713.

(77) Davidson, D. W.; Handa, Y. P.; Ratcliffe, C. I.; Tse, J. S.; Powell, B. M. *Nature* **1984**, *311*, 142.

(78) Takeya, S.; Kida, M.; Minami, H.; Sakagami, H.; Hachikubo, A.; Takahashi, N.; Shoji, H.; Soloviev, V.; Wallmann, K.; Biebow, N.; Obzhirov, A.; Salomatin, A.; Poort, J. *Chem. Eng. Sci.* **2006**, *61*, 2670.

(79) Tse, J. S.; Mckinnon, W. R.; Marchi, M. *J. Phys. Chem.* **1987**, *91*, 4188.

(80) Shpakov, V. P.; Tse, J. S.; Tulk, C. A.; Kvamme, B.; Belosludov, V. R. *Chem. Phys. Lett.* **1998**, *282*, 107.

(81) Fernandez, R. G.; Abascal, J. L. F.; Vega, C. *J. Chem. Phys.* **2006**, *124*, 144506.

(82) Tanaka, H.; Tamai, Y.; Koga, K. *J. Phys. Chem. B* **1997**, *101*, 6560.

(83) Jiang, H.; Jordan, K. D. *J. Phys. Chem. C* **2010**, *114*, 5555.

(84) Greathouse, J. A.; Cygan, R. T.; Simmons, B. A. *J. Phys. Chem. B* **2006**, *110*, 6428.

(85) Tse, J. S.; Klein, M. L.; McDonald, I. R. *J. Phys. Chem.* **1983**, *87*, 4198.

(86) Baumert, J. PhD dissertation, Christian-Albrechts University, 2003.

(87) Tse, J. S.; Shpakov, V. P.; Murashov, V. V.; Belosludov, V. R. *J. Chem. Phys.* **1997**, *107*, 9271.

(88) Ross, R. G.; Andersson, P.; Backstrom, G. *Nature* **1981**, *290*, 322.

(89) Andersson, O.; Suga, H. *Phys. Rev. B* **1994**, *50*, 6583.

(90) Cook, J. G.; Leaist, D. G. *Geophys. Res. Lett.* **1983**, *10*, 397.

(91) Sloan, E. D. In *Clathrate hydrates of natural gases*; 2nd ed.; Marcel Dekker: New York, 1998, p 62.

(92) Krivchikov, A. I.; Gorodilov, B. Y.; Korolyuk, O. A.; Manzhelii, V. G.; Conrad, H.; Press, W. *J. Low Temp. Phys.* **2005**, *139*, 693.

(93) Krivchikov, A. I.; Gorodilov, B. Y.; Korolyuk, O. A.; Manzhelii, V. G.; Romantsova, O. O.; Conrad, H.; Press, W.; Tse, J. S.; Klug, D. D. *Phys. Rev. B* **2006**, *73*, 064203.

(94) Rosenbaum, E. J.; English, N. J.; Johnson, J. K.; Shaw, D. W.; Warzinski, R. P. *J. Phys. Chem. B* **2007**, *111*, 13194.

(95) Avila, M. A.; Suekuni, K.; Umeo, K.; Fukuoka, H.; Yamanaka, S.; Takabatake, T. *Phys. Rev. B* **2006**, *74*, 125109.

(96) Bridges, F.; Downward, L. *Phys. Rev. B* **2004**, *70*, 140201.

(97) Koza, M. M.; Johnson, M. R.; Viennois, R.; Mutka, H.; Girard, L.; Ravot, D. *Nature Materials* **2008**, *7*, 805.

(98) Kim, H.; Kaviany, M.; Thomas, J. C.; Van der Ven, A.; Uher, C.; Huang, B. *Phys. Rev. Lett.* **2010**, *105*, 265901.

(99) Dharmawardana, M. W. C. *J. Phys. Chem.* **1983**, *87*, 4185.

(100) Tse, J. S.; White, M. A. *J. Phys. Chem.* **1988**, *92*, 5006.

(101) Schober, H.; Itoh, H.; Klapproth, A.; Chihaia, V.; Kuhs, W. F. *Eur. Phys. J. E* **2003**, *12*, 41.

(102) Andersson, P.; Ross, R. G. *Journal of Physics C-Solid State Physics* **1983**, *16*, 1423.

(103) Cook, J. G. L., M. J. In *Proceedings of the 17th International Thermal Conductivity Conference*; Plenum Press: Gaithersbug, MD, 1983.

(104) English, N. J.; Tse, J. S.; Carey, D. J. *Phys. Rev. B* **2009**, *80*.

(105) Krivchikov, A. I.; Romantsova, O. O.; Korolyuk, O. A. *Low Temperature Physics* **2008**, *34*, 648.

(106) Ramos, M. A.; Buchenau, U. *Phys. Rev. B* **1997**, *55*, 5749.

(107) Chazallon, B.; Itoh, H.; Koza, M.; Kuhs, W. F.; Schober, H. *Phys. Chem. Chem. Phys.* **2002**, *4*, 4809.

(108) Inoue, R.; Tanaka, H.; Nakanishi, K. *J. Chem. Phys.* **1996**, *104*, 9569.

(109) Tse, J. S.; Shpakov, V. P.; Belosludov, V. R.; Trouw, F.; Handa, Y. P.; Press, W. *Europhys. Lett.* **2001**, *54*, 354.

(110) Baumert, J.; Gutt, C.; Shpakov, V. P.; Tse, J. S.; Krisch, M.; Muller, M.; Requardt, H.; Klug, D. D.; Janssen, S.; Press, W. *Phys. Rev. B* **2003**, *68*, 7.

(111) Lubchenko, V.; Wolynes, P. G. *Proceedings of the National Academy of Sciences* **2003**, *100*, 1515.

(112) Krivchikov, A. I.; Manzhelii, V. G.; Korolyuk, O. A.; Gorodilov, B. Y.; Romantsova, O. O. *Phys. Chem. Chem. Phys.* **2005**, *7*, 728.

(113) Ahmad, N.; Phillips, W. A. *Solid State Commun.* **1987**, *63*, 167.

(114) Jiang, H.; Myshakin, E. M.; Jordan, K. D.; Warzinski, R. P. *J. Phys. Chem. B* **2008**, *112*, 10207.

(115) MullerPlathe, F. *J. Chem. Phys.* **1997**, *106*, 6082.

(116) Oligschleger, C.; Schon, J. C. *Phys. Rev. B* **1999**, *59*, 4125.

(117) Jund, P.; Jullien, R. *Phys. Rev. B* **1999**, *59*, 13707.

(118) Che, J. W.; Cagin, T.; Deng, W. Q.; Goddard, W. A. *J. Chem. Phys.* **2000**, *113*, 6888.

(119) Schelling, P. K.; Phillpot, S. R.; Keblinski, P. *Phys. Rev. B* **2002**, *65*, 144306.

(120) Chantrenne, P.; Barrat, J. L. *J Heat Trans-T Asme* **2004**, *126*, 577.

(121) Berman, R. *Phys. Rev.* **1949**, *76*, 315.

(122) Sellan, D. P.; Landry, E. S.; Turney, J. E.; McGaughey, A. J. H.; Amon, C. H. *Phys. Rev. B* **2010**, *81*, 214305.

(123) Turney, J. E. PhD Dissertation, Carnegie Mellon University, 2009.

(124) Zhang, M. M.; Lussetti, E.; de Souza, L. E. S.; Muller-Plathe, F. *J. Phys. Chem. B* **2005**, *109*, 15060.

(125) Buch, V.; Sandler, P.; Sadlej, J. *J. Phys. Chem. B* **1998**, *102*, 8641.

(126) Howell, P. C. *J. Comput. Theor. Nanosci.* **2011**, *8*, 2144.

(127) Zhou, X. W.; Aubry, S.; Jones, R. E.; Greenstein, A.; Schelling, P. K. *Phys. Rev. B* **2009**, *79*, 115201.

(128) Lindberg, G. E.; Wang, F. *J. Phys. Chem. B* **2008**, *112*, 6436.

(129) Andersson, O.; Inaba, A. *Phys. Chem. Chem. Phys.* **2005**, *7*, 1441.

(130) English, N. J.; Tse, J. S. *Phys. Rev. Lett.* **2009**, *103*, 4.

(131) Anderson, B. J.; Tester, J. W.; Trout, B. L. *J. Phys. Chem. B* **2004**, *108*, 18705.

(132) de la Pena, L. H.; Kusalik, P. G. *J. Chem. Phys.* **2006**, *125*, 054512.

(133) de la Pena, L. H.; Razul, M. S. G.; Kusalik, P. G. *J. Chem. Phys.* **2005**, *123*, 144506.

(134) Hernández de la Peña, L.; Gulam Razul, M. S.; Kusalik, P. G. *J. Phys. Chem. A* **2005**, *109*, 7236.

(135) Conde, M. M.; Vega, C.; McBride, C.; Noya, E. G.; Ramirez, R.; Sese, L. M. *J. Chem. Phys.* **2010**, *132*, 114503.

(136) Noya, E. G.; Vega, C.; Sese, L. M.; Ramirez, R. *J. Chem. Phys.* **2009**, *131*, 124518.

(137) Vega, C.; Conde, M. M.; McBride, C.; Abascal, J. L. F.; Noya, E. G.; Ramirez, R.; Sese, L. M. *J. Chem. Phys.* **2010**, *132*, 046101.

(138) Hernández de la Peña, L.; Kusalik, P. G. *J. Am. Chem. Soc.* **2005**, *127*, 5246.

(139) Pamuk, B.; Soler, J. M.; Ramírez, R.; Herrero, C. P.; Stephens, P. W.; Allen, P. B.; Fernández-Serra, M. V. *Phys. Rev. Lett.* **2012**, *108*, 193003.

(140) Martin, R. T.; Bailey, S. W.; Eberl, D. D.; Fanning, D. S.; Guggenheim, S.; Kodama, H.; Pevear, D. R.; Srodon, J.; Wicks, F. J. *Clays Clay Miner.* **1991**, *39*, 333.

(141) Tambach, T. J.; Bolhuis, P. G.; Smit, B. *Angew. Chem. Int. Ed.* **2004**, *43*, 2650.

(142) Cygan, R. T.; Liang, J. J.; Kalinichev, A. G. *J. Phys. Chem. B* **2004**, *108*, 1255.

(143) Mignon, P.; Ugliengo, P.; Sodupe, M.; Hernandez, E. R. *Phys. Chem. Chem. Phys.* **2010**, *12*, 688.

(144) Suter, J. L.; Boek, E. S.; Sprik, M. *J. Phys. Chem. C* **2008**, *112*, 18832.

(145) Clausen, P.; Andreoni, W.; Curioni, A.; Hughes, E.; Plummer, C. J. G. *J. Phys. Chem. C* **2009**, *113*, 12293.

(146) Clausen, P.; Andreoni, W.; Curioni, A.; Hughes, E.; Plummer, C. J. G. *J. Phys. Chem. C* **2009**, *113*, 15218.

(147) Benco, L.; Tunega, D. *Phys. Chem. Miner.* **2009**, *36*, 281.

(148) Berghout, A.; Tunega, D.; Zaoui, A. *Clays Clay Miner.* **2010**, *58*, 174.

(149) Schmidt, S. R.; Katti, D. R.; Ghosh, P.; Katti, K. S. *Langmuir* **2005**, *21*, 8069.

(150) Bougeard, D.; Smirnov, K. S. *Phys. Chem. Chem. Phys.* **2007**, *9*, 226.

(151) Geysermans, P.; Noguera, C. *J. Mater. Chem.* **2009**, *19*, 7807.

(152) Tambach, T. J.; Hensen, E. J. M.; Smit, B. *J. Phys. Chem. B* **2004**, *108*, 7586.

(153) Tunega, D.; Goodman, B. A.; Haberhauer, G.; Reichenauer, T. G.; Gerzabek, M. H.; Lischka, H. *Clays Clay Miner.* **2007**, *55*, 220.

(154) Kohn, W.; Becke, A. D.; Parr, R. G. *J. Phys. Chem.* **1996**, *100*, 12974.

(155) Perdew, J. P.; Ruzsinszky, A.; Constantin, L. A.; Sun, J. W.; Csonka, G. I. *J. Chem. Theory Comput.* **2009**, *5*, 902.

(156) Friesner, R. A. *Proc. Natl. Acad. Sci. U. S. A.* **2005**, *102*, 6648.

(157) Jenness, G. R.; Karalti, O.; Jordan, K. D. *Phys. Chem. Chem. Phys.* **2010**, *12*, 6375.

(158) Becke, A. D. *Phys. Rev. A* **1988**, *38*, 3098.

(159) Lee, C. T.; Yang, W. T.; Parr, R. G. *Phys. Rev. B* **1988**, *37*, 785.

(160) Perdew, J. P.; Chevary, J. A.; Vosko, S. H.; Jackson, K. A.; Pederson, M. R.; Singh, D. J.; Fiolhais, C. *Phys. Rev. B* **1992**, *46*, 6671.

(161) Perdew, J. P.; Burke, K.; Ernzerhof, M. *Phys. Rev. Lett.* **1996**, *77*, 3865.

(162) Becke, A. D. *J. Chem. Phys.* **1993**, *98*, 5648.

(163) Grimme, S. *J. Comput. Chem.* **2004**, *25*, 1463.

(164) Grimme, S. *J. Comput. Chem.* **2006**, *27*, 1787.

(165) Grimme, S.; Antony, J.; Ehrlich, S.; Krieg, H. *J. Chem. Phys.* **2010**, *132*, 154104.

(166) Tkatchenko, A.; Scheffler, M. *Phys. Rev. Lett.* **2009**, *102*, 073005.

(167) von Lilienfeld, O. A.; Tavernelli, I.; Rothlisberger, U.; Sebastiani, D. *Phys. Rev. Lett.* **2004**, *93*, 153004.

(168) Tavernelli, I.; Lin, I. C.; Rothlisberger, U. *Phys. Rev. B* **2009**, *79*, 045106.

(169) Lee, K.; Murray, E. D.; Kong, L.; Lundqvist, B. I.; Langreth, D. C. *Phys. Rev. B* **2010**, *82*, 081101.

(170) Dion, M.; Rydberg, H.; Schröder, E.; Langreth, D. C.; Lundqvist, B. I. *Phys. Rev. Lett.* **2004**, *92*, 246401.

(171) Andersson, Y.; Langreth, D. C.; Lundqvist, B. I. *Phys. Rev. Lett.* **1996**, *76*, 102.

(172) Jaynes, W. F.; Boyd, S. A. *Clays Clay Miner.* **1991**, *39*, 428.

(173) Austen, K. F.; White, T. O. H.; Marmier, A.; Parker, S. C.; Artacho, E.; Dove, M. T. *J Phys-Condens Mat* **2008**, *20*.

(174) Bridgeman, C. H.; Buckingham, A. D.; Skipper, N. T.; Payne, M. C. *Mol. Phys.* **1996**, *89*, 879.

(175) Churakov, S. V. *J. Phys. Chem. B* **2006**, *110*, 4135.

(176) Silvestrelli, P. L.; Toigo, F.; Ancilotto, F. *J. Phys. Chem. C* **2009**, *113*, 17124.

(177) Silvestrelli, P. L.; Toigo, F.; Ancilotto, F. *J. Phys. Chem. B* **2006**, *110*, 12022.

(178) Labat, F.; Fuchs, A. H.; Adamo, C. *J. Phys. Chem. Lett.* **2010**, *1*, 763.

(179) Jenness, G. R.; Karalti, O.; Al-Saidi, W. A.; Jordan, K. D. *J. Phys. Chem. A* **2011**, *115*, 5955.

(180) Rimola, A.; Civalleri, B.; Ugliengo, P. *Phys. Chem. Chem. Phys.* **2010**, *12*, 6357.

(181) Voora, V. K.; Al-Saidi, W. A.; Jordan, K. D. *J. Phys. Chem. A* **2011**, *115*, 9695.

(182) Suter, J. L.; Anderson, R. L.; Greenwell, H. C.; Coveney, P. V. *J. Mater. Chem.* **2009**, *19*, 2482.

(183) Heinz, H.; Koerner, H.; Anderson, K. L.; Vaia, R. A.; Farmer, B. L. *Chem. Mater.* **2005**, *17*, 5658.

(184) Ugliengo, P.; Zicovich-Wilson, C. M.; Tosoni, S.; Civalleri, B. *J. Mater. Chem.* **2009**, *19*, 2564.

(185) Kresse, G.; Hafner, J. *Phys. Rev. B* **1993**, *47*, 558.

(186) Kresse, G.; Furthmuller, J. *Phys. Rev. B* **1996**, *54*, 11169.

(187) Blochl, P. E. *Phys. Rev. B* **1994**, *50*, 17953.

(188) Monkhorst, H. J.; Pack, J. D. *Phys. Rev. B* **1976**, *13*, 5188.

(189) Jiang, D. E.; Carter, E. A. *J. Phys. Chem. B* **2004**, *108*, 19140.

(190) Mignon, P.; Ugliengo, P.; Sodupe, M. *J. Phys. Chem. C* **2009**, *113*, 13741.

(191) Plimpton, S. *J. Comput. Phys.* **1995**, *117*, 1.

(192) Teleman, O.; Jonsson, B.; Engstrom, S. *Mol. Phys.* **1987**, *60*, 193.

(193) Hockney.; Eastwood. *Computer Simulation Using Particles* Adam Hilger, NY, 1989.

(194) Tambach, T. J.; Hensen, E. J. M.; Smit, B. *J. Phys. Chem. B* **2004**, *108*, 7586.

(195) Greathouse, J. A.; Durkin, J. S.; Larentzos, J. P.; Cygan, R. T. *J. Chem. Phys.* **2009**, *130*, 134713.

(196) Tuckerman, M.; Berne, B. J.; Martyna, G. J. *J. Chem. Phys.* **1992**, *97*, 1990.

(197) Santra, B.; Michaelides, A.; Scheffler, M. *J. Chem. Phys.* **2007**, *127*, 184104.

(198) Larentzos, J. P.; Greathouse, J. A.; Cygan, R. T. *J. Phys. Chem. C* **2007**, *111*, 12752.

(199) Wales, D. J.; Walsh, T. R. *J. Chem. Phys.* **1996**, *105*, 6957.

(200) Ramirez, F.; Hadad, C. Z.; Guerra, D.; David, J.; Restrepo, A. *Chem. Phys. Lett.* **2011**, *507*, 229.

(201) Santra, B.; Michaelides, A.; Fuchs, M.; Tkatchenko, A.; Filippi, C.; Scheffler, M. *J. Chem. Phys.* **2008**, *129*, 194111.

(202) Tsai, C. J.; Jordan, K. D. *Chem. Phys. Lett.* **1993**, *213*, 181.

(203) Kim, K.; Jordan, K. D.; Zwier, T. S. *J. Am. Chem. Soc.* **1994**, *116*, 11568.

(204) Olson, R. M.; Bentz, J. L.; Kendall, R. A.; Schmidt, M. W.; Gordon, M. S. *J. Chem. Theory Comput.* **2007**, *3*, 1312.

(205) Wang, F. F.; Jenness, G.; Al-Saidi, W. A.; Jordan, K. D. *J. Chem. Phys.* **2010**, *132*, 134303.

(206) Bates, D. M.; Tschumper, G. S. *J. Phys. Chem. A* **2009**, *113*, 3555.

(207) Aragones, J. L.; MacDowell, L. G.; Vega, C. *J. Phys. Chem. A* **2011**, *115*, 5745.